Conference Proceedings of the Society for Experimental Mechanics Series

Francois Barthelat · Chad Korach · Pablo Zavattieri
Barton C. Prorok · K. Jane Grande-Allen *Editors*

Mechanics of Biological Systems and Materials, Volume 7

Proceedings of the 2014 Annual Conference on Experimental and Applied Mechanics

SEM

Springer

Conference Proceedings of the Society for Experimental Mechanics Series

Series Editor
Tom Proulx
Society for Experimental Mechanics, Inc.
Bethel, CT, USA

For further volumes:
http://www.springer.com/series/8922

Francois Barthelat • Chad Korach • Pablo Zavattieri
Barton C. Prorok • K. Jane Grande-Allen
Editors

Mechanics of Biological Systems and Materials, Volume 7

Proceedings of the 2014 Annual Conference on Experimental and Applied Mechanics

Springer

Editors
Francois Barthelat
Department of Mechanical Engineering
McGill University
Montreal, QC, Canada

Pablo Zavattieri
Purdue University
West Lafayette, IN, USA

K. Jane Grande-Allen
Rice University
Houston, TX, USA

Chad Korach
Stony Brook University
Stony Brook, NY, USA

Barton C. Prorok
Auburn University
Auburn, AL, USA

ISSN 2191-5644 ISSN 2191-5652 (electronic)
ISBN 978-3-319-06973-9 ISBN 978-3-319-06974-6 (eBook)
DOI 10.1007/978-3-319-06974-6
Springer Cham Heidelberg New York Dordrecht London

Library of Congress Control Number: 2014944532

Printed on acid-free paper

Springer is part of Springer Science+Business Media (www.springer.com)

Preface

Mechanics of Biological Systems and Materials, Volume 7: Proceedings of the 2014 Annual Conference on Experimental and Applied Mechanics represents one of eight volumes of technical papers presented at the SEM 2014 SEM Annual Conference & Exposition on Experimental and Applied Mechanics organized by the Society for Experimental Mechanics and held in Lombard, IL June 3–5, 2013. The complete Proceedings also includes volumes on: *Dynamic Behavior of Materials; Challenges In Mechanics of Time-Dependent Materials; Advancement of Optical Methods in Experimental Mechanics: MEMS and Nanotechnology; Composite, Hybrid, and Multifunctional Materials; Fracture, Fatigue, Failure and Damage Evolution; and Experimental and Applied Mechanics.*

Each collection presents early findings from experimental and computational investigations on an important area within Experimental Mechanics, the Mechanics of Biological Systems and Materials being one of these areas.

This volume summarizes the exchange of ideas and information among scientists and engineers involved in the research and analysis of how mechanical loads interact with the structure, properties, and function of living organisms and their tissues. The scope includes experimental, imaging, numerical, and mathematical techniques and tools spanning various length- and timescales. Establishing this symposium at the Annual Meeting of the Society for Experimental Mechanics provides a venue where state-of-the-art experimental methods can be leveraged in the study of biomechanics. A major goal of the symposium was for participants to collaborate in the asking of fundamental questions and the development of new techniques to address bio-inspired problems in society, human health, and the natural world. The organizers would like to thank all the speakers and staff at SEM for enabling a successful program.

Montreal, QC, Canada — Francois Barthelat
Stony Brook, NY, USA — Chad Korach
West Lafayette, IN, USA — Pablo Zavattieri
Auburn, AL, USA — Barton C. Prorok
Houston, TX, USA — K. Jane Grande-Allen

Contents

Chapter 1
In Vitro Complex Shear Modulus of Bovine Muscle Tissue

Jennifer Hay and Sabina Cherneva

Abstract In living tissue, there exists a reciprocal relationship between mechanical properties and function. That is, properties affect function, and function can affect properties by means of adaptation. Thus, knowledge of mechanical properties leads directly to knowledge of function. Dynamic instrumented indentation provides a way to measure the mechanical properties of soft biological tissue that is relevant, localized, and accurate.

In this work, we measured the complex shear modulus of bovine muscle tissue, submerged in saline at bovine body temperature (38 °C). The muscle tissue was significantly stiffer in the direction of the grain ($G' = 24.4 \pm 13.9$ kPa) than perpendicular to it ($G' = 11.4 \pm 2.9$ kPa). This was expected, because the muscle tissue naturally acts in the direction of the grain to alternately exert and relax force. The loss factor was highly consistent and independent of testing direction: $\tan \delta = 0.34 \pm 0.035$. These results were consistent with what others have measured for muscle tissue using dynamic mechanical analysis (DMA).

Keywords Elasticity • Loss factor • Modulus • Muscle • Indentation

1.1 Introduction

Being able to measure the mechanical properties is crucial to understanding soft living tissue. First, there is a reciprocal relationship between mechanical properties and function. That is, properties affect function, but function can also affect properties by means of adaptation. Thus, knowledge of mechanical properties leads directly to knowledge of function. Further, gel is often used as a substitute for living tissue [1]. In order to tailor the gel to mimic the tissue, one must first know the mechanical properties of the tissue. Thus, the purpose of this work is to demonstrate the use of instrumented indentation to measure the complex shear modulus of soft tissue under physiologically relevant conditions—submerged in saline at body temperature.

Given the structure of skeletal muscle tissue, we should expect its mechanical properties to be highly anisotropic. The *fascicles* are the bundles of individual muscle cells or fibers which alternatively contract and relax in order to cause motion. Since this is the direction in which the muscle is used, we should expect the modulus to be higher in this direction than in the direction orthogonal to the fascicles. The common term for the fascicle is the "grain" of the tissue. In this work, we measure the properties of skeletal muscle tissue both in the direction of the fascicle action (with the grain) and orthogonally (against the grain).

A number of factors make instrumented indentation (also known as nano-indentation) a promising tool for mechanical evaluation of biological tissue. Measurements of force and displacement are highly resolved. Further, some systems allow the indenter to be oscillated, which offers the benefits of dynamic mechanical analysis on a microscopic scale [2, 3]. Testing is localized, which offers the possibility of evaluating spatial variations in properties in complex tissues. Testing in fluid is straightforward, because samples are naturally small and can be probed while submerged. Despite all these potential

J. Hay (✉)
Nano-Measurements Operation, Agilent Technologies, Inc., 105 Meco Ln., Suite 200, Oak Ridge, TN 37830, USA
e-mail: jenny.hay@agilent.com

S. Cherneva
Institute of Mechanics, Bulgarian Academy of Sciences, Acad. G. Bonchev Str., Bl.4, Sofia 1113, Bulgaria

F. Barthelat et al. (eds.), *Mechanics of Biological Systems and Materials, Volume 7: Proceedings of the 2014 Annual Conference on Experimental and Applied Mechanics*, Conference Proceedings of the Society for Experimental Mechanics Series,
DOI 10.1007/978-3-319-06974-6_1,

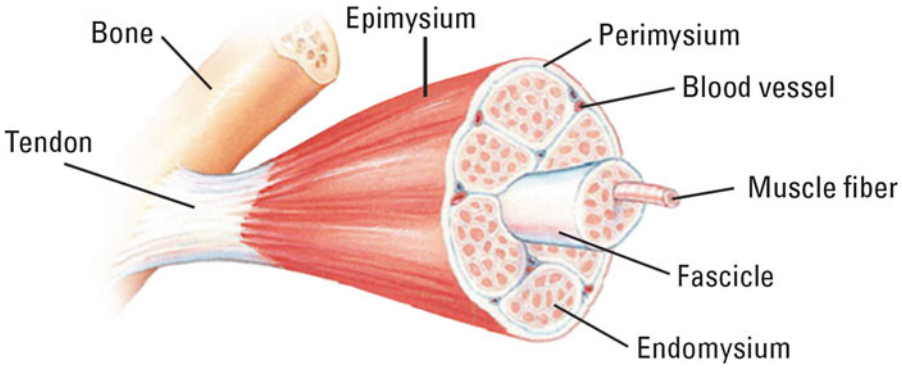

Fig. 1.1 Schematic of skeletal muscle tissue (National Cancer Institute, public domain)

advantages, however, accurate measurements of mechanical properties of soft biological tissue by instrumented indentation are rare in the literature. Three difficulties plague most measurements of this kind: (1) semi-static actuation, (2) complex sample geometry, and (3) measured stiffness comparable to the uncertainty in stiffness.

With semi-static actuation, the force is applied to the tissue monotonically and likewise removed in order to generate a "force-displacement curve" from which properties are derived. However, from such a test, it is nearly impossible to deconvolute the elastic, viscoelastic, and viscoplastic components of deformation. Not only do the measurements depend on the loading/unloading rates in a complex way, the procedure does not lend itself to the measurement of the loss factor which quantifies material damping. When testing biological tissue, it is far better to apply a small static force, then oscillate the probe and measure the amplitude ratio (to quantify stiffness) and the phase shift (to quantify damping). We must note that such a procedure does not allow for the quantification of viscoplasticity, i.e. creep. But at least the influence of creep on the measured viscoelastic properties can be minimized by waiting for a time after applying the small force, then testing with a small oscillation amplitude at a frequency of 1 Hz or greater.

In order to calculate shear modulus from stiffness (or loss modulus from damping), the test geometry must be simple enough to be modeled. Simpler geometry lends itself to simpler modeling. Studies which employ atomic-force microscopy (AFM) to mechanically test single cells often report stiffness, rather than modulus, due to the complex geometry of the cell. Although such measurements may be useful [4], they can only be used to compare cells of similar geometry. One may not, for example, compare the stiffness of one cell to that of another cell which is twice as large. The analytic model for instrumented indentation which is commonly used to calculate the complex shear modulus (from the more fundamental measurements of stiffness and damping) requires that the tested sample be large relative to the size of the contact, and that the contact area be well known [5, 6]. Let us momentarily defer the discussion of how large the sample must be. The second requirement of a well-known contact area is most easily met by using a flat-ended cylindrical punch, because the contact area is always that of the punch face, regardless of indentation depth.

The most insidious problem related to the mechanical testing of biological tissue is that without careful consideration, the measured contact stiffness can easily be on the order of the *uncertainty* in stiffness, which is dominated by the uncertainty in the stiffness of the actuator, be it AFM or nano-indenter. This problem exists whether the test is semi-static or oscillatory, but its exact manifestation depends on the nature of the test and the calculation path for determining stiffness. The solution to this problem involves (1) quantifying the uncertainty in stiffness, and (2) designing the test so that the contact stiffness will be much larger than the uncertainty.[1] For the equipment used in the present work, the uncertainty in stiffness at 10 Hz was previously evaluated to be 0.1 N/m. Thus, we must design our test so that the contact stiffness (S) is much larger than the uncertainty, say 5 N/m or more. This is tantamount to determining the diameter of the punch which is needed, because according to Sneddon's elastic contact theory [5] as later developed by Oliver et al. [6] and Herbert et al. [7], the contact stiffness scales with the contact diameter. Specifically, the real and imaginary components of the complex shear modulus ($G^* = G' + iG''$) are calculated as

$$G' = S(1-\nu)/(2D), \text{and} \tag{1.1}$$

$$G'' = C\omega(1-\nu)/(2D), \tag{1.2}$$

[1] The analogous problem for contact damping was also handled, but is not presented here for the sake of simplicity.

where ν is the Poisson's ratio of the material (assumed 0.5 for soft tissue) and D is the contact diameter (i.e. the diameter of the punch face). Often, the shear loss modulus (G'') is not reported as an absolute value, but in relation to the shear storage modulus. The loss factor, which characterizes the damping relative to stiffness, is calculated directly as

$$\tan\delta = G''/G' = C\omega/S. \tag{1.3}$$

Thus, we wish to know the value of D which is necessary for S to be of sufficient magnitude, relative to uncertainty. In order to calculate D in this way, we must make an educated guess at the value for G'. Kiss et al. have measured the complex shear modulus of human uterine muscle tissue by means of dynamic mechanical analysis (Bose EnduraTEC ELF 3220) [8]. At 10 Hz, they measured $G' = 19$ kPa parallel to the grain of the tissue and $G' = 14$ kPa perpendicular to the grain of the tissue. Further, they measured a loss factor of $\tan\delta = 0.33$ which was independent of direction. Thus, let us use a modulus value of 15 kPa to calculate the punch diameter which is needed to achieve a contact stiffness which is at least 5 N/m, or 50 times greater than our uncertainty.

$$D = S(1-\nu)/\left(2G'\right) = (5\,\mathrm{N/m})(1-0.5)/\left(2^{*}15\mathrm{e}+3\,\mathrm{N/m^2}\right) = 8.3\mathrm{e}-5\,\mathrm{m} = 83\,\mu\mathrm{m}. \tag{1.4}$$

Thus, we should use a flat punch with a diameter of 83 μm, or greater. We concede that this is very large in the realm of instrumented indentation, but such a contact size is necessary due to the extreme compliance of the tissue. The surprising outcome of this calculation is evidence of its necessity! Presently, we have enough information to return to the question of sample size. The sample radius and depth should be large relative to this contact size, and should take into account that we would like to make many indentation tests over the prepared surface.

1.2 Experimental Method

Two samples of bovine muscle tissue (steak) were tested in this work: one cut across the grain (Fig. 1.2a) and one cut with the grain (Fig. 1.2b). It should be noted that the testing direction is orthogonal to the plane of the cut. Thus, the sample which was cut across the grain (Fig. 1.2a) was actually tested in the direction of the grain—that is, in the direction of the muscle fibers illustrated in Fig. 1.1. The sample which was cut with the grain (Fig. 1.2b) was actually tested perpendicular to the grain. Results are reported according to the direction of the *test*, not the cut.

Samples were prepared as follows: The night before testing, the tissue was rough-cut and frozen. On the day of testing, a disk ($d = 8$ mm, $h = 8$ mm) was cut from the frozen material and quickly adhered to the base of the sample well[2] using 5-min epoxy. Once the epoxy had set, the well was filled with saline, and the sample holder was attached to the hot stage. Finally, a microscope slide was gently laid over the sample to keep it from drying while the sample equilibrated at the testing temperature (38 °C). The equilibration time was about 30 min. Figure 1.3 shows a sample ready for testing.

The Agilent G200 NanoIndenter was used for all testing. The system was configured with a DCM II actuator, the CSM option, and the hot-stage option. The CSM option allowed the superposition of an oscillating force, and the hot-stage option allowed the samples to be tested at body temperature. The DCM II actuator was fitted with a flat-ended cylindrical punch (D = 101.1 μm) in order to generate a known and constant contact.

The NanoSuite test method "G-Series DCM CSM Flat Punch Complex Modulus, Gel" was used for all testing. Each test with this method comprised the following steps:

1. Approach the surface, oscillating the indenter at its natural frequency (110 Hz), until contact is detected,
2. Switch to the prescribed testing frequency[3] (10 Hz),
3. Apply pre-test compression (7 μm),
4. Wait for creep to subside,
5. Sense tissue stiffness and damping, and
6. Withdraw the indenter and move to the next test site.

[2] In order to allow the samples to be submerged during testing, we used washers to build a "well" on the sample base plate for the hot-stage. Two washers, built up from the base plate with JB Weld SteelStick, provided sufficient depth (8 mm).

[3] The present testing was done at 10 Hz, but any frequency may be prescribed in the range of 1–200 Hz.

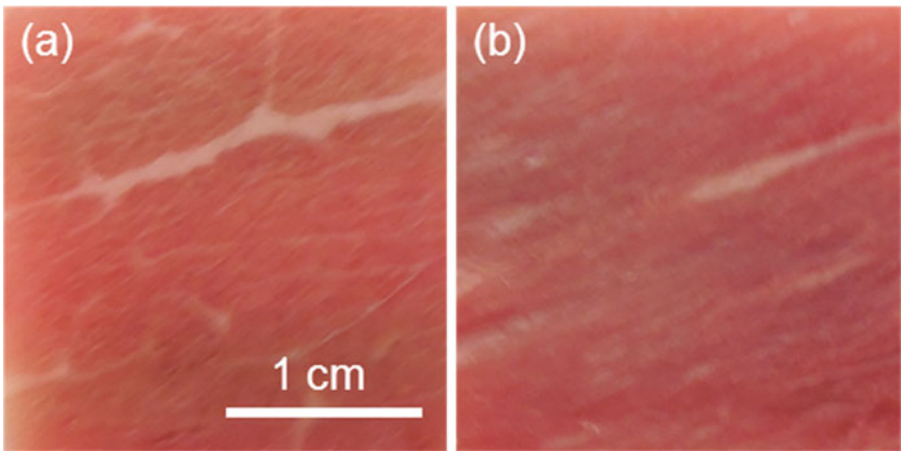

Fig. 1.2 Typical surfaces, as exposed for testing (**a**) cut across the grain, and (**b**) cut with the grain

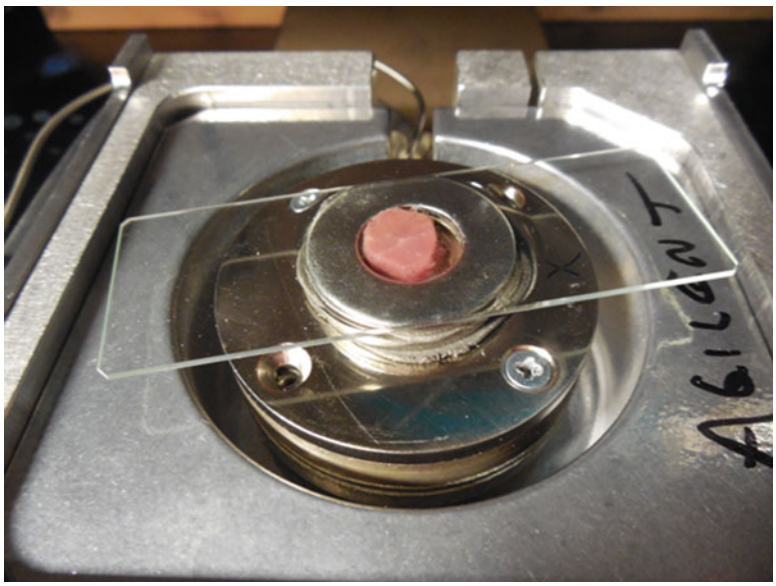

Fig. 1.3 Steak sample, submerged and ready for testing at body temperature. Microscope slide was used to seal the sample and keep it moist until just prior to testing

With this method, 25 different sites were tested on each sample; individual test sites were separated by at least 400 μm. Tests were performed in red tissue only. Each test took about 2 min. In order to keep the samples from drying out, testing was paused after every 10 min in order to add 1–2 drops of saline (Others have solved the problem of drying by the more elegant technique of integrating a slow drip [9]).

1.3 Results and Discussion

Testing a sample submerged in saline poses no problems. Although the system indeed senses contact with the saline, the signature is different from that of contact with tissue (Fig. 1.4). The attraction between the tip and the fluid causes a momentary decrease in the stiffness of the system. Thus, the interaction between the tip and the fluid manifests as a slight, but detectable, increase in the phase angle. Subsequent contact with the sample causes an increase in the stiffness of the system, thus manifesting as a sharp decrease in the phase angle. This extreme sensitivity in the phase angle is attained by oscillating the indenter at the natural frequency of the instrument (110 Hz) during the approach.

Figure 1.5 shows the results for shear modulus of bovine muscle tissue at 10 Hz. The muscle tissue is significantly stiffer in the direction of the grain ($G' = 24.4 \pm 13.9$ kPa) than perpendicular to it ($G' = 11.4 \pm 2.9$ kPa). This is not surprising

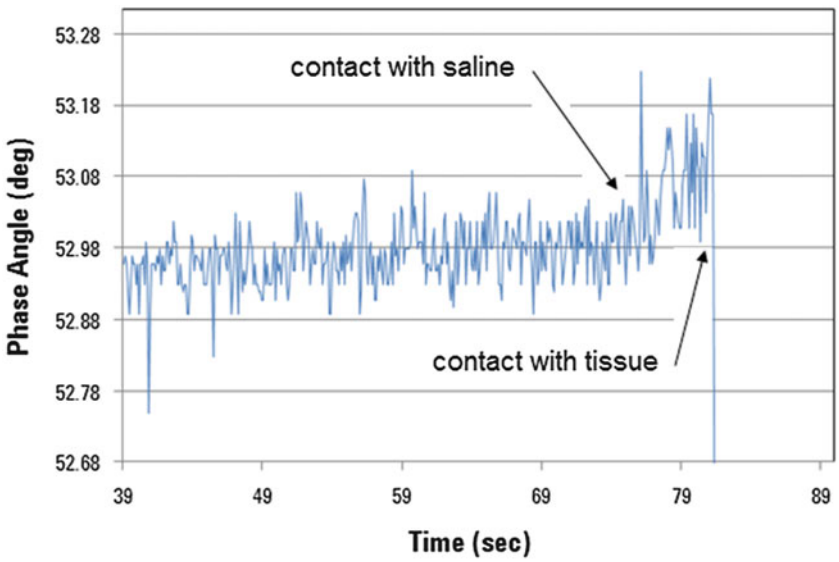

Fig. 1.4 Signatures in the phase angle of contact with saline, then tissue

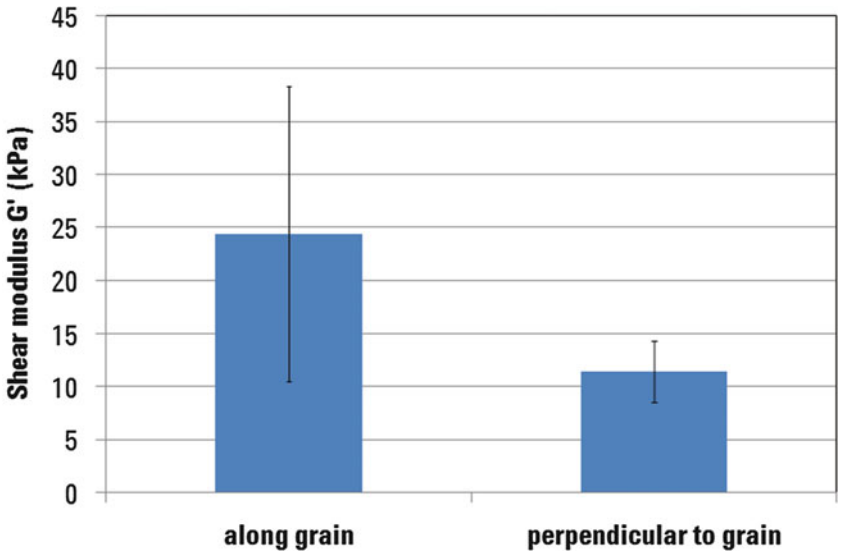

Fig. 1.5 Shear modulus of bovine muscle tissue at 38 °C, 10 Hz (N = 25)

since the muscle tissue naturally acts in the direction of the grain to alternately exert and relax force. The results measured in this work are remarkably similar to those measured by Kiss et al. on human uterine muscle tissue at the same frequency (parallel: $G' = 19 \pm 3$ kPa; perpendicular: $G' = 14 \pm 3$ kPa) [8].

The point-to-point variation in modulus is high, especially in the direction of the grain, but this is to be expected for biological materials. We know that the observed variation is due to true point-to-point variation in properties, not measurement uncertainty, because we designed the test such that the contact stiffness would be more than 50 times greater than the uncertainty in stiffness. Indeed, when we apply the same equipment and test method to uniform gels of comparable moduli, the point-to-point variation is quite low [10]. In the direction of the grain, this high degree of variation is likely due to the complex structure exposed by the cut across the grain (as illustrated by the cross-section of Fig. 1.1). Perpendicular to the grain, the variation is much smaller. Again, this is not surprising, because the volume of tested material likely includes many fascicles lying perpendicular to the motion of the indenter, and so the measured response for each test is influenced by many fascicles.

The uniformity and consistency of the loss factor (Fig. 1.6) are quite surprising. The ability of the tissue to damp energy, as quantified by the loss factor, is rather independent of the direction or location: $\tan\delta = 0.34 \pm 0.035$. On human uterine muscle tissue, Kiss et al. also found the loss factor at 10 Hz to be independent of direction and of virtually identical magnitude ($\tan\delta = 0.33 \pm 0.05$ [8]). This value of the loss factor means that at 10 Hz, the capacity of the tissue to damp out energy is one third of its capacity to store energy elastically. This is physiologically realistic and only measurable in vitro by keeping the sample submerged during testing.

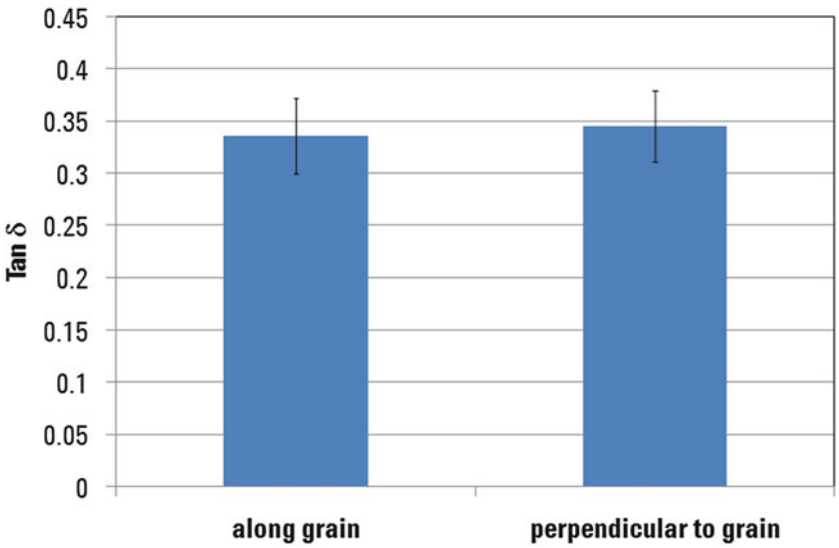

Fig. 1.6 Loss factor of bovine muscle tissue at 38 °C, 10 Hz (N = 25)

1.4 Conclusions

In this work, we measured the complex shear modulus of bovine muscle tissue at 10 Hz to be $G' = 24.4 \pm 13.9$ kPa (parallel to the grain), $G' = 11.4 \pm 2.9$ kPa (perpendicular to the grain), and $\tan\delta = 0.34 + 0.035$ (direction independent). These values are comparable to what others have measured for muscle tissue by means of dynamic mechanical analysis (DMA). Achieving results which are comparable to DMA requires (1) oscillatory indentation, (2) a test geometry which lends itself to modeling, and (3) a contact stiffness which is large relative to the uncertainty in stiffness. For the present equipment and test method, these requirements demand testing at a scale which is relatively large in the realm of instrumented indentation. We hope that these techniques will help others to illuminate fundamental relationships between structure, history, and mechanical properties in biological tissues.

Acknowledgements This work was funded in part by the Bulgarian Ministry of Education, Youth and Science, Human Resources Development Operational Program, Project BG051PO001/3.3-05-0001 "Science and Business".

References

1. Jain SK, Bhattacharayya CN, Badonia B, Singh RP (2003) Study of unusual phenomenon of contact firing on Gelatine block using 38 special revolver - forensic importance. Forensic Sci Int 133(3):183–189
2. Hay JL, Agee P, Herbert EG (2010) Continuous stiffness measurement during instrumented indentation testing. Exp Tech 34(3):86–94
3. Hay J, Herbert E (2011) Measuring the complex modulus of polymers by instrumented indentation testing. Exp Tech 37(3):55–61
4. Lee YJ, Lee GJ, Kang SW, Cheong Y, Park HK (2013) Label-free and quantitative evaluation of cytotoxicity based on surface nanostructure and biophysical property of cells utilizing AFM. Micron 49:54–59
5. Sneddon IN (1965) The relation between load and penetration in the axisymmetric boussinesq problem for a punch of arbitrary profile. Int J Eng Sci 3(1):47–57
6. Pharr GM, Oliver WC, Brotzen FR (1992) On the generality of the relationship among contact stiffness, contact area, and elastic-modulus during indentation. J Mater Res 7(3):613–617
7. Herbert EG, Oliver WC, Pharr GM (2008) Nanoindentation and the dynamic characterization of viscoelastic solids. J Phys D Appl Phys 41(7), 074021
8. Kiss MZ, Hobson MA, Varghese T, Harter J, Kliewer MA, Hartenbach EM, Zagzebski JA (2006) Frequency-dependent complex modulus of the uterus: preliminary results. Phys Med Biol 51(15):3683–3695
9. Huja SS, Hay JL, Rummel AM, Beck FM (2010) Quasi-static and harmonic indentation of osteonal bone. J Dent Biomech 2010:1–7
10. Hay J (2012) Complex shear modulus of commercial gelatin by instrumented indentation. Agilent Technologies, Inc., Document No: 5990-0000EN. Available from: http://cp.literature.agilent.com/litweb/pdf/5990-9745EN.pdf. Accessed 6 June 2013

Chapter 2
A Camera-Based Experimental Method for Mechanical Test on Patellar Tendons

Lorenzo Scalise, Barbara Lonzi, and Natascia Bernacchia

Abstract Tendons have an important structural function in biological systems, their mechanical proprieties are therefore of great interest in biomechanics engineering and reconstructive medicine. Their physiological characteristics require the study of specific experimental methods able to determine the mechanical properties.

In this work the authors propose a non-contact experimental method aimed to the characterization of the mechanical proprieties of rabbit patellar tendons based on the use of a single camera and a customized gripping system. The tensile test setup makes use of a fixed lens camera and a customized algorithm, providing the measurement of the local sample strain on different part along the tendon and of the cross-sectional area. The tensile stress is estimated by the value of the applied load and of the cross-section value of the sample; tensile stress values are calculated at a frequency of 8 Hz. Moreover a special design of the clamps and the use of the camera allow to protect the experimental tests from the well-known problem of peak force concentrations on the sample and slipping at its extremities, which indeed are typical problems in tensile testing of tendons.

Keywords Rabbit patellar tendons • Tensile test • Image analysis • Cross-sectional area • Gripping system

2.1 Introduction

Patellar tendon failure is a relatively rare lesion caused by forced flexion of the knee against an eccentric contraction of the quadriceps. This pathology could occur also in patients with systemic diseases that attack the soft tissue, such as rheumatoid arthritis [1]. Today the failure of patellar tendon is a very interesting and studied theme, because the tendon represents an important resource for autologous reconstruction of the cruciate ligament. This aspect becomes important especially in the sport medicine, where the incidence of the cruciate ligament injuries is particularly high [2].

Mechanical testing is frequently used to characterize tendons, and to analyze the effects of therapies and surgical interventions on their mechanical properties. Tendon physiological characteristics have been therefore already studied in the past years; such studies highlight the necessity to use specifically developed experimental methods to determine the mechanical properties.

The most reliable mechanical data were obtained by applying a tensile load on samples provided by both the insertions. A typical stress–strain curve for collagen-rich tissue, as the tendon, is non-linear and has an initial phase, when the crimps stretch out, called toe region [3], characterized by a large increase in the length with increasing force. When load increases, stiffness of the tissue also increases and progressively the curve is characterized by a sudden rise in the slope. The slope of this linear region is calculated as the value of Young's (or elastic) modulus of the tendon [3]. In literature different values for ultimate stress can be found, it varies from 28 to 44 N/mm^2 for young humans (with a strain to failure of 14–18 %). For tendons belonging to adult subjects, however, the ultimate stress varies between 42.5 and 113 N/mm^2 (with an elongation of 10–12.5 %) [4]. Elastic modulus in adult vertebrate varies from 0.8 to 2 GPa [5].

L. Scalise (✉) • B. Lonzi • N. Bernacchia
Dipartimento di Ingegneria Industriale e Scienze Matematiche (DIISM), Università Politecnica delle Marche,
Via Brecce Bianche 1, 60131 Ancona, Italy
e-mail: l.scalise@univpm.it

F. Barthelat et al. (eds.), *Mechanics of Biological Systems and Materials, Volume 7: Proceedings of the 2014 Annual Conference on Experimental and Applied Mechanics*, Conference Proceedings of the Society for Experimental Mechanics Series,
DOI 10.1007/978-3-319-06974-6_2,

Due to their morphology and composition, in most of the cases, the gripping action of tendon samples for tensile can lead to a possible alteration of their mechanical characteristics, especially at their extremities where a cross-section reduction occurs. Clamping the tendon into a test machine is a known major problem, which derives from the independence of the fibrous units, that has to be separately held, therefore a technique such as gluing, which holds only the outside of the tendon, is not fully appropriate [5]. Gripping directly the specimen between two metal plates determines a serious distortion of the fibers, with consequent non-uniform concentrations of load and deformation, resulting in premature failure. Another problem could be possible slippage respect to the grips, due to the low friction coefficient. In literature it is possible to find several solution aiming to solve the problem of clamping tendons [5], unfortunately none of them completely solves all the problems. Riemersa and Schamhardt [6] have described the "cryo-jaw", a cooled clamp with liquid carbon dioxide (CO_2), with plates provided by channels for tissue freezing. Since then, cooled terminals were considered the gold standard for the mechanical tests with high applied loads on the soft tissues. It should be emphasized that the cryogenic techniques [7, 8] create a zone of thermal transition, which may alter the mechanical properties of the tendon tissue. The possibility to incorporate tendon extremities in resin was evaluated, in order to avoid the problem of stress concentration at the ends of the sample [9].

A second relevant aspect is related to the need to carefully estimate the geometric characteristics of the tendon [10] in order to determinate the mechanical properties of tendons. Legerlotz et al. found that specimen length and cross-sectional area (CSA) appear to influence failure stress, strain and modulus in fascicles from two functionally different tendons [11]. Measurement of the previous mentioned geometrical parameters is really important to correctly assess tendon mechanical behavior. Goodship et al. [12] summarized the main methods historically used to measure CSA. The first technique is based on cutting sections of the tendon, although it allows morphological measurements, it is destructive and mechanical tests cannot be performed subsequently. Other research group thought to acquire tendon dimensions using a microscope. To allow measurement of CSA in structures with a non-uniform shape, a device known as an area micrometer was developed; in order to adopt this technique, it is necessary to compress the tendon into a rectangular slot of known width until the tendon completely fills the slot. However, this technique is affected by the applied pressure and permanent damage could occur to the soft tissue. In 1996 Race and Amis adopted a technique to measure tendon CSA by making a silicone rubber cast and a mold of the structure. The drawbacks of this technique are that it is time consuming, dehydration and shrinkage of the sample.

Due to the tendon nature of soft tissue, contact could alter shape and real cross-section. The need of no contact technique and systems able to provide the measurement of strain and sample CSA, is clear. Some authors [13,15] developed a method based on measuring the width of the tendon using incremental degrees and then calculating the CSA by integration. Recently an optical approach has been proposed [13], consisting on laser light projection perpendicular to the sample axis, digital camera acquisition of the scene and image processing. Despite the high resolution and precision achievable, the testing time is still limiting its use in dynamic and fatigue testing, due to the need to stop and restart the test to allow the previous described task. An assessment of tendon biomechanics and its relation with age was conducted [14] on rabbit patellar tendons. In this work cross-section was measured in three equidistant locations with a camera and the averaged value was calculated. Revel et al. [15] conducted a study on vibrational properties of rabbit Achilles tendons where their length was measured using a video dimensions analyzer (VDA), which has also the role to monitor any slippage. Limitations can be found in the complexity of these techniques and in the possibility to measure cross-sections at fixed intervals only stopping and restarting the test.

In this work, a novel non-contact measurement method is proposed for the characterization of the mechanical proprieties of rabbit patellar tendons based on the use of a single camera and a customized gripping system. The tensile test setup makes use of a fixed lens camera, measuring the local sample strain simultaneously along the tendon length and cross-sectional area frame by frame. The experimental setup will be validated and the choice of the rabbit as an experimental animal model was suggested by the similarity of its extensor mechanism with the human one.

2.2 Experimental Set Up and Measurement Procedure

The aim here is to propose the design of a new measurement bench for mechanical characterization of biological materials, in details rabbit patellar tendons, to allow tensile tests, using some traditional instrumentation but also new strategies to solve main problems connected with biological tissues, like sample clamping and assessing the real elongation and cross-section of the sample.

The apparatus is composed by a clamping system, a servo-pneumatic uniaxial test machine and a data acquisition unit, a PC, a non-contact strain measurement system and an illumination source (Fig. 2.1).

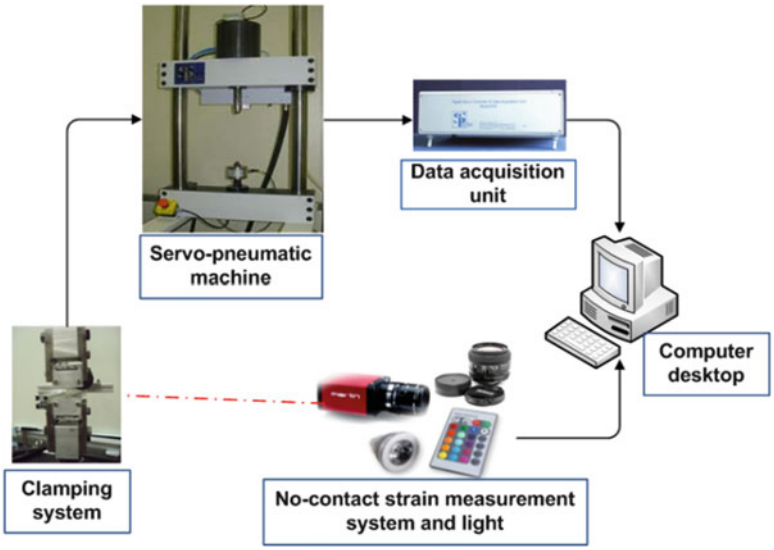

Fig. 2.1 Experimental setup scheme for tensile tests

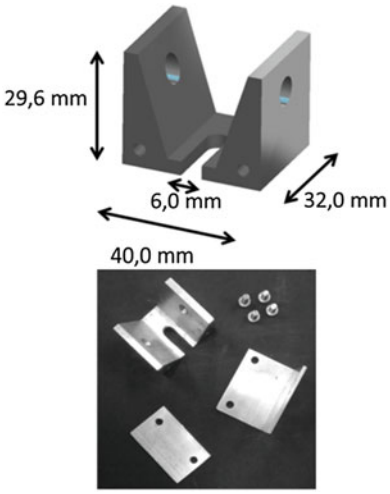

Fig. 2.2 Clamping system design and realization

The experimental setup has been firstly tested on reference material with known mechanical behavior. In particular Nylon 6 wires (with diameter of 0.7 mm) were chosen. To this aim the international standard UNI EN ISO 527-1/1997 [16] was taken in consideration for test procedure and to compare stress–strain curves obtained with the experimental setup. In the following all the components will be discussed, highlighting the proposed solutions.

An appropriate clamping system has been studied in order to optimize sample gripping without modifying its mechanical properties and avoiding its slippage. Technical requirements were defined analyzing dimensions of the sample, with a well-documented study in literature [17]. A length of 17.2 $\pm$ 1.5 mm and a CSA of 13.3 $\pm$ 1.0 mm^2 were found. For what concerns the gripping technique both cryogenic method and mechanical serration were discarded due to the possibility to create a damage at tendon ends and alter its mechanical behavior, especially because rabbit patellar tendon are small structures. The choice was done considering the inclusion of tendon ends in cement inside custom designed clamps. In Fig. 2.2 the innovative clamping system could be seen in all its components; it has been realized in aluminium and appropriately studied to withstand and distribute tension, avoiding failure also using plates fixed with screws. An holding system allows to connect the grips with the testing machine, and an angular bar serves to maintain the correct alignment of the sample during each phase of the preparation procedure.

Tensile tests were carried out using a Servo-pneumatic test machine 966-804-23 made (Si-Plan Electronics Research Ltd©) provided by an actuator rod, with embedded displacement transducers (maximum stroke equal to 50 mm), and a load cell (maximum calibrated force: 2 kN). The equipment includes also a data acquisition unit and a manufacturer software, which works with the operating system Windows XP®, characterized by an extremely simple interface that allows the user to enter test settings and, at the same time, to observe in real time quantities of interest. In this work the tests were performed in

Fig. 2.3 AVT Marlin F-131 camera and optical zoom

Table 2.1 Camera settings

Brightness (relative)	50
Gain	7
Shutter (relative)	4,095
Lens opening	2.8
Focus	0.3

displacement control mode. Moreover it is possible to choose sample frequency, ramp rate, maximum and minimum values, waveform, cycles number, etc.

As reported in the introduction, we aimed to be design and experimental system able to observe eventual gliding during the application of the tensile load. To this aim, the measurement of the sample strain was determined processing images captured during the test by a digital camera with fixed lens. A Marlin F-131 camera (Allied Vision Technologies, Fig. 2.3) was used, with a IEEE 1394 firewire connection (field of view: 1,280 × 1,204 pixels). Camera settings, as sample frequency, brightness, gain and shutter, can be selected through Measurement and Automation software (National Instruments). Considering the small size of the rabbit patellar tendons, in order to improve image resolution, that is to reduce the pixel size, an AF NIKKOR 24 mm 1: 2.8 D optical zoom was added. Technical settings of the camera (Table 2.1) affect the value of the sampling frequency. For all our tests, a sampling frequency of 8 Hz (or fps, frame per second) was used, while a sampling frequency of 80 Hz was used for displacement and force signals generated by the test machine.

The camera was placed perpendicularly to the clamping system at a distance of 20 cm from the sample. In order to enhance the image contrast, a white led light source and a black background screen were used. From camera calibration with 3 gauge blocks [18] ($\dim_{mm}1 = 3.415$ mm, $\dim_{mm}2 = 2.935$ mm and $\dim_{mm}3 = 4.005$ mm), pixel size was determined using the following equation:

$$pixel\ size_{(mm)} = \frac{\dim_{mm}}{\dim_{pixel}} \tag{2.1}$$

Camera calibration was done recording the support placed in specimen test plane. Images were analyzed with a custom algorithm realized in Matlab® (Mathworks) environment, to measure $\dim_{pixel}$, i.e. block dimension in pixels.

2.3 Materials and Methods

Ten patellar tendons were extracted from five healthy rabbits, 3–4 months old (3.5 ± 0.5 kg), and maintained in low saline solution at −20 °C until the test day [15, 19]. The protocol was the same for all the samples, consisting in dissection of the tendon from muscle tissue, keeping the patella in the upper side and the tibial bone insertion in the lower side. Before tensile tests, specimens were thawed for 4 h at room temperature (20 °C) covered with a sterile gauze soaked with physiological saline solution, in order to avoid dehydration. The tendon was gripped with the innovative clamping system described previously. First a silicone spray was applied in order to easily clean the clamps after the experiment. After that both the ends of the sample, patella and tibial insertion, have been embedded in a synthetic resin inside the clamps (Fig. 2.4), taking care in preventing sample drying using physiological saline solution. On the central area of tendon two markers were created, at a distance of 4 mm from the clamps, using black ink. In this work all the tests were performed in displacement control mode, in order to check actuator movement through parameters like maximum and minimum values, ramp rate, expressed respectively in mm and mm/s. Load and displacement data were saved in CSV format (Comma Separated Value). The image sequences were acquired during the tests using a custom interface implemented in LabView® (National Instruments)

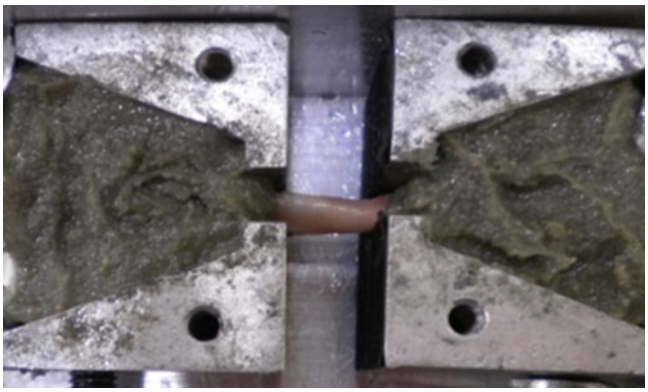

Fig. 2.4 Tendon assembly

environment, allowing to start and stop the acquisition, finally to save images in bmp format (bitmap). A trigger has been used to synchronize data acquisition from camera and tensile test start.

After sample preparation and assembly on test machine, a caliper (resolution of 0.05 mm) was used to measure l_0 (initial length) as the distance between the clamps. Rabbit patellar tendons were preloaded applying a constant elongation equal to 1 % l_0 for 10 min [20]. After that sample was subjected to a preconditioning procedure performing 10 loading-unloading cycles with a deformation varying between 0 and 2 % l_0. It is possible to notice that this range corresponds to the initial toe region, that typically characterize tendon stress–strain curve [3], in which all the fibers are crimped, so this step is essential for their straightening before the tensile test. For tendon an elongation rate of 0.3 mm/s [21] was chosen due to its viscoelastic nature. Last step was constituted by the tensile test performed at the same rate of the previous phase.

A custom algorithm was developed in Matlab® environment to analyse acquired data. The processing was divided into two parts due to the nature of information: machine data and image sequences, stored respectively in comma separated value format (.csv) and bitmap (.bmp). Preliminary the off-set compensation is operated on the initial values from the load cell and the testing machine displacement transducer. Load signal was low-pass filtered with a II order Butterworth filter with a normalized cut-off frequency of 0.03 Hz. Considering displacement signal as Δl, longitudinal tensile strain ε_l was determined at any time instant as the elongation Δl divided by the initial length l_0 [16]:

$$\varepsilon_l = \frac{\Delta l}{l_o} \tag{2.2}$$

Unitary tensile stress σ was calculated as the ratio between load to which the sample is subjected and its initial cross-sectional area (CSA) [16].

$$\sigma = \frac{F}{CSA} \tag{2.3}$$

Tendon CSA was calculated from the first frame with segmentation technique, multiplying the number of white pixels counted on a chosen line in the central area of the specimen, by the pixel size. Cross-sectional area was found as $(d/2)^2\,\pi$, assuming a circular model for the tendon section area [22]. From the stress–strain curves the following parameters were determined: ultimate tensile strength and ultimate strain (σ_u, ε_u), Young modulus (E). The last is usually evaluated using linear regression analysis as it is reported in [16] for reference specimens, but for tendons it was necessary to calculate Young modulus as the slope in the linear region of the stress–strain curve that is the portion which presents a deformation between 2 and 4 %, as it is also reported in [3]. The equation used for the calculation of E is:

$$E = \frac{\sigma_2 - \sigma_1}{\varepsilon_2 - \varepsilon_1} \tag{2.4}$$

What we can obtained from these curves are nominal values of analyzed mechanical properties. In order to compare tensile test curves with image-derived deformation it is necessary to resample load cell signal. As regards image sequences, a region of interest was chosen on the last frame of the test, when the complete actuator stroke is reached. The ROI is constituted by specimen location and both the clamping system and the markers should be clearly visible, so it was selected also taking the lower reference line. Subsequent processing was done only on this region that was selected for all the test frames. Image processing began with a contrast enhancement. After that, images were converted from grayscale to binary

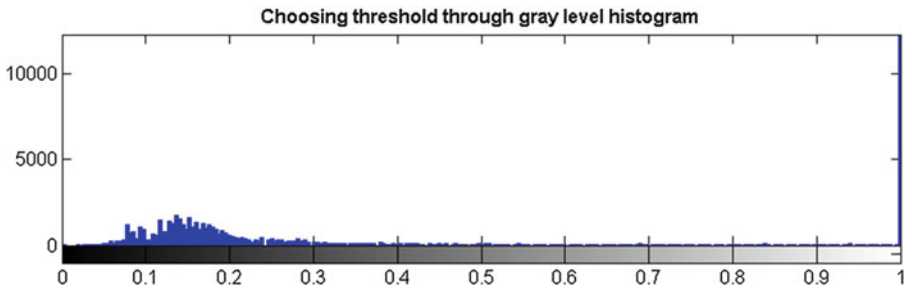

Fig. 2.5 Gray level histogram

Fig. 2.6 Image segmentation

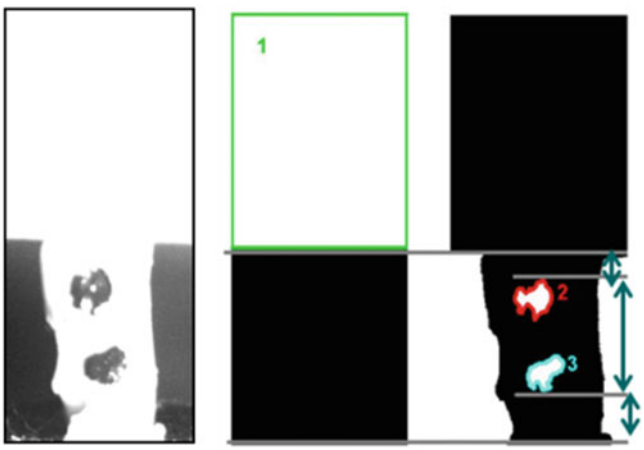

coding in order to obtain black and white ones, using a threshold that could be chosen by the user, looking at gray level histogram (Fig. 2.5). The threshold was not fixed for all the samples, due to the variability of natural illumination during the test days, despite the fact that the test room is pretty isolated by the external ambient. The tendon makes segmentation process difficult cause of its gray level is similar to that of the clamp. However targets are dark, in contrast to those applied on the wire. In particular images were treated with opening, a morphological operation that allows sample removal in order to see the upper clamp, using a line as sliding structure. Complementary images were computed from those ones just converted in binary format, in which it is possible to correctly identify white objects with an edge-based segmentation algorithm. The reference line on the lower clamp was fixed, instead of the upper one and the markers that move during the test and in some cases could not be well recognized. To address this problem they were automatically localized for each frame implementing a procedure that assesses the distance of each target respect to the position in the previous frame and searching the minimum value. In this way, locations of the markers and upper clamp were determined considering maximum or minimum height as it can be seen in Fig. 2.6.

Distances between the two markers were computed and converted in mm in order to obtain the length l; the longitudinal strain ε_l was measured using:

$$\varepsilon_l(t) = \frac{l(t) - l_0}{l_0} \tag{2.5}$$

where l_0 is the sample initial length measured from the first frame. Moreover through image analysis it was possible to measure the sample diameter for each frame, allowing to have a continuous CSA measurement during the test. In this way stress values can be calculated as:

$$\sigma(t) = \frac{F(t)}{CSA(t)} \tag{2.6}$$

All mechanical parameters were found, as it was previous discussed for nominal curves, but using strain and cross-section measurements provided by image analysis.

2.4 Experimental Results

Data measured with the camera-based measurement method was validated considering, as reference method, data measured with the displacement and force sensors of the tensile test transducer; validation tests were performed on nylon samples. From scatter-plot of the measured data, a Pearson squared correlation coefficient $R^2 = 0.99$ was obtained and the extended uncertainty of the strain measurement, calculated according [23], was:

$$U_\varepsilon = \sqrt{\left(\frac{\partial f}{\partial x_1} \cdot u_{x_1}\right)^2 + \left(\frac{\partial f}{\partial_{x_2}} \cdot u_{x_2}\right)^2} \tag{2.7}$$

where $x_1 = \Delta l$, $x_2 = l_0$, and $\varepsilon = f(\Delta l, l_0)$.

A value of 0.03 was obtained as extended uncertainty on strain measurement, considering a confidence interval with a coverage factor $k = 1$.

Rabbit patellar tendons were preconditioned applying an elongation in the range of 2–4 %, in order to allow fibers stretching and uncrimping. Loading/unloading cycles ($N = 10$) were analyzed and it was possible to notice that the stress/strain curve is shifted to the right along the X axis in each load cycle, revealing the presence of a non-elastic and hysteretic behavior as it was found in literature [24]. In Fig. 2.7 stress/strain curve of quasi-static tensile tests are visible. The upper curve was obtained using data provided by the sensors of the tensile test machine and considering single CSA (calculated from the first video frame); the lower curve instead reports the stress/strain curve simultaneously measured with the proposed measurement method where CSA and strain measurements were obtained with the proposed image-based method. Both the curves show a curve trend comparable with that showed in literature [3], but the slipping of one of the sample extremity is detectable in the later (Fig. 2.8).

Transverse strain was also evaluated from the frames and it is reported in Fig. 2.9, showing the necking of the sample during the tensile test. In the following figures (Figs. 2.10, 2.11 and 2.12) box-plots of Young modulus, ultimate strain and ultimate strength are finally presented.

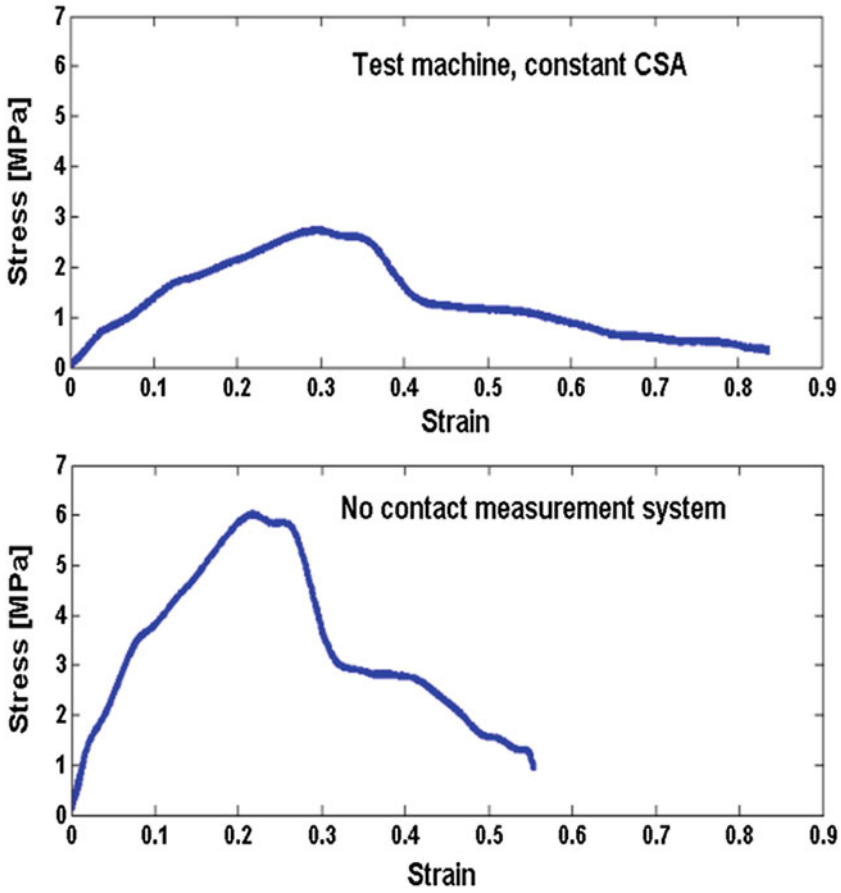

Fig. 2.7 Example of a stress/strain curve of rabbit patellar tendon

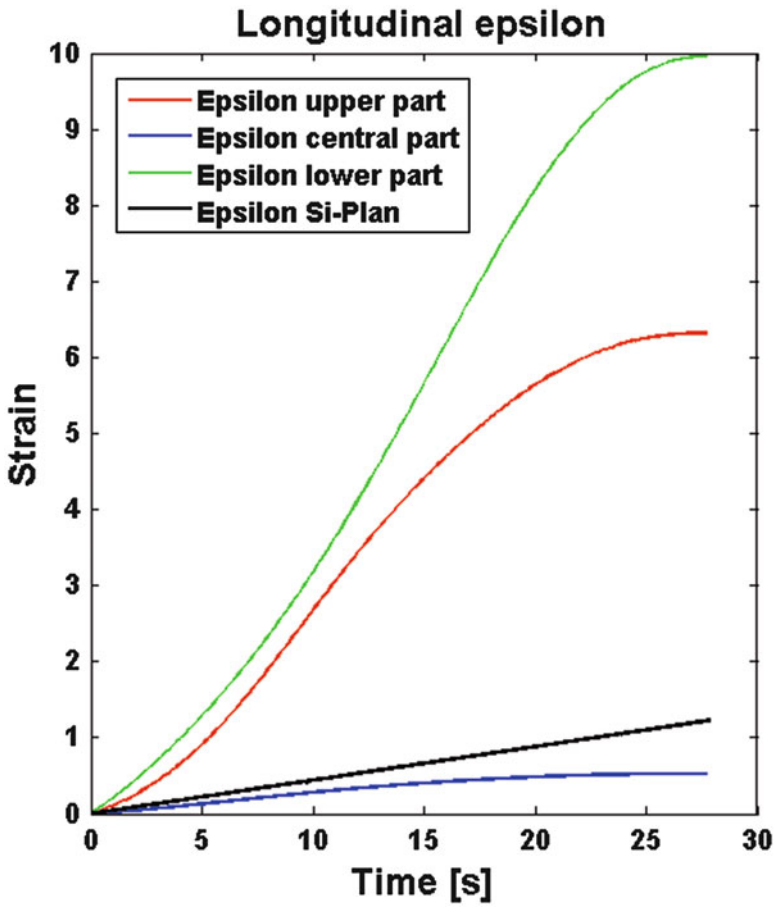

Fig. 2.8 Strain measured by machine and camera (in the three segments)

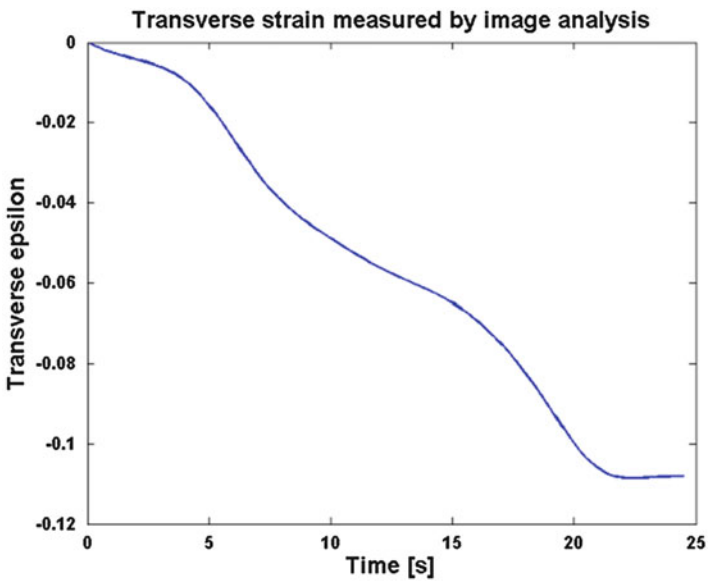

Fig. 2.9 Transverse strain

In Fig. 2.10, the Young's modulus is calculated using the data obtained by the tensile machine (Machine), the data from the new proposed method for the evaluation of strain but a constant cross-section area (Camera) and final the strain and the cross-section area evaluated with the image-system (Variable CSA).

In Figs. 2.11 and 2.12, the ultimate strain and stress are calculated using the data obtained with the tensile machine (Test Machine) and the data from the new proposed method (strain and CSA measurement frame-by-frame) (Camera).

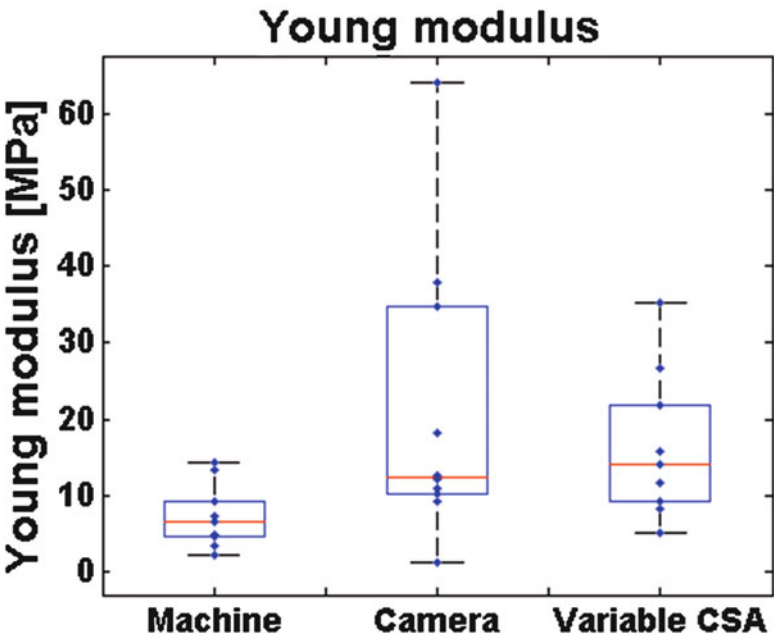

Fig. 2.10 Boxplot of Young modulus

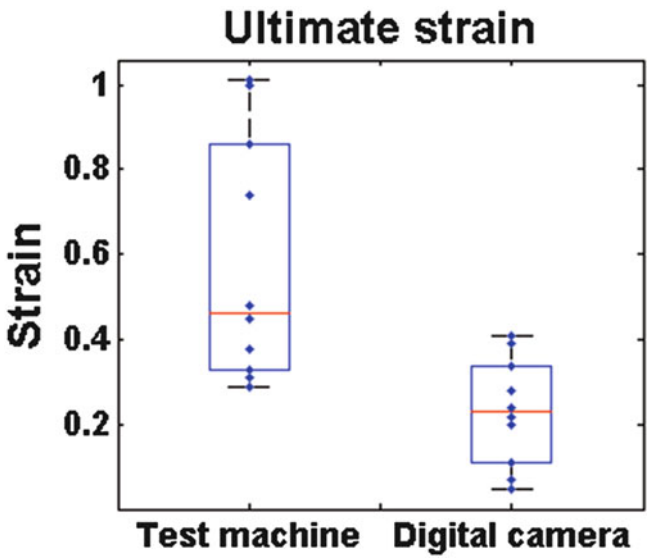

Fig. 2.11 Boxplot of ultimate strain

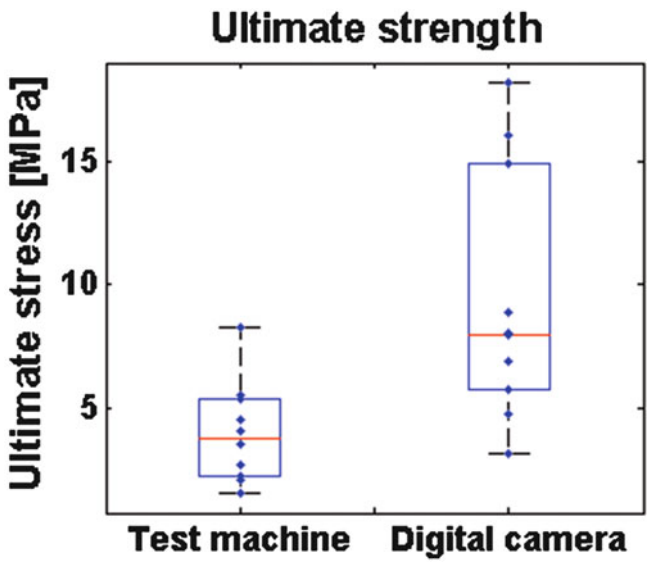

Fig. 2.12 Boxplot of ultimate strength

2.5 Conclusions

The new measurement method is based on the digital image processing, using techniques as filtering, segmentation, edge detection. These tools are powerful in order to measure longitudinal strain and CSA completely contactless, obtaining results that fit well to the values found literature. The proposed method was validated using samples of known mechanical characteristics (nylon) showing a good correlation ($R^2 = 0.99$) and an extended uncertainty on strain measurement rather limited (0.03).

One of the innovative aspects of the proposed method lies in the fact that the image analysis should provide a local measure of the strain which allows the control and correction of slipping phenomena. Also important it is the frame-by-frame measurement of the sample cross-sectional area. It should be noted that the majority of methods reported in the literature is based either on destructive methods (such as casts or insertion into preformed frames) or on optical methods (such as laser, or use in conjunction with a video dimension analyser) but they still do not guarantee a continuous measurement and often require to stop and restart the test, to be able to capture the sample.

Moreover tendons are considered to have a viscoelastic behavior, so it is essential to measure both the two quantities in order to correctly characterize and study mechanical parameters of this biological material. The experimental protocol developed in this work allowed to realize a suitable preconditioning of the tendon fibers, as can be observed by the decrease of the area inside the hysteresis loop, and at the same time it ensured a good performance in the tensile tests, correctly determining the sample rupture in its middle section.

Future steps in this work will be to study tendons in pathological conditions, in order to test the efficacy of grafts or therapies, and to design a new and custom clamping system also for samples of larger size. Another topic would be to validate the clinical evidence that the use of collagen I membranes in tendons could enhance and facilitate its repair. In particular a study on the behavior of tendons from the mechanical point of view could be realized to assess the changes resulting from the presence of the membrane.

From the experimental point-of-view the next improvement will aim to introduce a second camera, perpendicular to the optical axis of the first one, allowing to model the sample cross-section area with a ellipse [21].

Acknowledgments The authors would like to thank Prof. Enrico Primo Tomasini for supporting the research activity, dott. Alessandro Scalise and his medical team for sample dissection.

References

1. Pritchard CH, Berney S (1989) Patellar tendon rupture in systemic lupus erythematosus. J Rheumatol 16(6):786–788
2. Alentorn-Geli E, Myer GD, Silvers HJ, Samitier G, Romero D, Lázaro-Haro C, Cugat R (2009) Prevention of non-contact anterior cruciate ligament injuries in soccer players. Part 1: mechanisms of injury and underlying risk factors. Knee Surg Sports Traumatol Arthrosc 17(7):705–729
3. Wang JH-C (2006) Mechanobiology of tendon. J Biomech 39:1563–1582
4. Ippolito E, Natali PG, Postacchini F, Accinni L, De Martino C (1980) Morphological, immunochemical and biochemical study of rabbit Achilles tendon at various ages. J Bone Joint Surg 62(4):583–592
5. Ker RF (2007) Mechanics of tendon, from an engineering perspective. Int J Fatigue 29(6):1001–1009
6. Riemersa DJ, Schamhardt HC (1982) The cryo-jaw, a clamp designed for in vitro rheology studies of horse digital flexor tendons. J Biomech 15(8):619–620
7. Sharkey NA, Smith TS, Lundmark DC (1995) Freeze clamping musculo-tendinous junctions for in vitro simulation of joint mechanics. J Biomech 28(5):631–635
8. Rincon L, Schatzmann L, Brunner P, Stäubli HU, Ferguson SJ, Oxland TR, Nolte LP (2001) Design and evaluation of a cryogenic soft tissue fixation device - load tolerances and thermal aspects. J Biomech 34(3):393–397
9. Shapiro PS, Rohde RS, Froimson MI, Lash RH, Postak P, Greenwald AS (2007) The effect of local corticosteroid or ketorolac exposure on histologic and biomechanical properties of rabbit tendon and cartilage. Am Assoc Hand Surg 2(4):165–172
10. Woo SL, Gomez MA, Sites TJ, Newton PO, Orlando CA, Akeson WH (1987) The biomechanical and morphological changes in the medial collateral ligaments of the rabbit after immobilization and remobilization. J Bone Joint Surg 69(8):1200–1211
11. Legerlotz K, Riley GP, Screen HR (2010) Specimen dimensions influence the measurement of material properties in tendon fascicles. J Biomech 43(12):2274–2280
12. Goodship AE, Birch HL (2005) Cross sectional area measurement of tendon and ligament in vitro: a simple, rapid non-destructive technique. J Biomech 38(3):605–608
13. Salisbury STS, Buckley CP, Zavatsky AB (2008) Image-based non-contact method to measure cross-sectional areas and shapes of tendons and ligaments. Meas Sci Technol 19(4):045705
14. Dressler MR, Butler DL, Wenstrup R, Awad HA, Smith F, Boivin GP (2002) A potential mechanism for age-related declines in patellar tendon biomechanics. J Orthop Res 20(6):1315–1322

15. Revel GM, Scalise A, Scalise L (2003) Measurement of stress–strain and vibrational properties of tendons. Meas Sci Technol 14(8):1427–1436
16. UNI EN ISO 527-1/1997 (1997) Plastics – determination of tensile properties
17. Maeda E, Tohyama H, Noguchi H, Yasuda K, Hayashi K (2010) Effects of maturation on the mechanical properties of regenerated and residual tissues in the rabbit patellar tendon after resection of its central one-third. Clin Biomech 25(9):953–958
18. UNI EN ISO 3650: 2002 (2002) Geometrical product specifications (GPS) - length standards - Gauge blocks
19. Woo SL, Orlando CA, Camp JF, Akeson WH (1986) Effects of postmortem storage by freezing on ligament tensile behavior. J Biomech 19(5):399–404
20. Fujie H, Yamamoto N, Murakami T, Hayashi K (2000) Effects of growth on the response of the rabbit patellar tendon to stress shielding: a biomechanical study. Clin Biomech 15(5):370–378
21. Ohno K, Yasuda K, Yamamoto N, Kaneda K, Hayashi K (1996) Biomechanical and histological changes in the patellar tendon after in situ freezing. Clin Biomech 11(4):207–213
22. Parent G, Cyr M, Desbiens-Blais F, Langelier E (2010) Bias and precision of algorithms in estimating the cross-sectional area of rat tail tendons. Meas Sci Technol 21(12):1–8
23. International Organization for Standardization (1993) Guide to the expression of uncertainty in measurement, 1st edn. International Organization for Standardization, Switzerland (corrected and reprinted 1995)
24. Woo SL, Debski RE, Zeminski J, Abramowitch SD, Saw SSC, Fenwick JA (2000) Injury and repair of ligaments and tendons. Annu Rev Biomed Eng 2:83–118

Chapter 3
Thin-Shell Behavior of Mammalian Tympanic Membrane Studied by Digital Holography

Morteza Khaleghi, Cosme Furlong, Jeffrey Tao Cheng, and John J. Rosowski

Abstract The acousto-mechanical-transformer behavior of the Tympanic Membrane (TM) is defined by its shape, 3D displacements, and mechanical properties. In this paper, we report the quantification of these characteristics by full-field-of-view optoelectronic techniques. Due to geometrical constraints imposed by the ear canal, however, 3D displacement measurements with multiple sensitivity vectors in holographic interferometry or 3D Laser Doppler Vibrometry (LDV) have limited applications for testing in vivo. Therefore, we seek alternative methods to perform 3D measurements. In our work, we hypothesize that the TM behaves as a thin-shell, so that the principal components of vibration are parallel to the TM's shape normal vectors, which allows the estimation of the 3D components of displacement with only 1D component of displacements and shape information. Full-field-of-view measurements of the TM are obtained with our digital holographic system, with shape measured in two-wavelength mode and 1D displacements measured in single-wavelength mode. The theoretically-estimated 3D components of displacement are then compared with those measured by methods of multiple sensitivity vectors. Preliminary data suggest that the thin-shell hypothesis is applicable for estimation of the 3D acoustically-induced vibrations of the TM excited at low and mid frequency ranges.

Keywords 3D displacement measurements • Digital holography • Sound-induced vibrations • Thin-shell theory • Tympanic membrane

3.1 Introduction

Air in the ear canal has low mechanical impedance, whereas the mechanical impedance at the center of the eardrum, the umbo, is high. The TM must act as a transformer between these two impedances; otherwise, most of the energy will be reflected rather than transmitted [1, 2]. The acousto-mechanical transformer behavior of the TM is determined by its shape, internal fibrous structure, and mechanical properties [3, 4]. Therefore, full-field-of-view measurements of shape and 3D motion of the TM is necessary. In addition, measurements of 3D motion of the TM can help to properly diagnose the degree and type of hearing loss, i.e., conductive, sensorineural, or mixed.

M. Khaleghi (✉)
Mechanical Engineering Department, Worcester Polytechnic Institute, Center for Holographic Studies and Laser micro-mechaTronics (CHSLT), Worcester, MA 01609, USA
e-mail: mkm@wpi.edu

C. Furlong
Mechanical Engineering Department, Worcester Polytechnic Institute, Center for Holographic Studies and Laser micro-mechaTronics (CHSLT), Worcester, MA 01609, USA

Eaton-Peabody Laboratory, Massachusetts Eye and Ear Infirmary, Boston, MA 02114, USA

Department of Otology and Laryngology, Harvard Medical School, Boston, MA 02114, USA

J.T. Cheng • J.J. Rosowski
Eaton-Peabody Laboratory, Massachusetts Eye and Ear Infirmary, Boston, MA 02114, USA

Department of Otology and Laryngology, Harvard Medical School, Boston, MA 02114, USA

F. Barthelat et al. (eds.), *Mechanics of Biological Systems and Materials, Volume 7: Proceedings of the 2014 Annual Conference on Experimental and Applied Mechanics*, Conference Proceedings of the Society for Experimental Mechanics Series,
DOI 10.1007/978-3-319-06974-6_3,

Due to geometrical constraints imposed by the ear canal, common 3D displacement measurements techniques such as multiple sensitivity vectors in holographic interferometry [5] or 3D Laser Doppler Vibrometry [6, 7] are not applicable for in vivo investigations that require an intact ear. However, we can, even in such a confined geometry, measure both the 1D component of sound-induced displacement and the shape of the membrane. Based on thin-shell hypothesis of the TM, sound-induced displacement vectors are hypothesized to be parallel to the corresponding normal vectors of the shape of the TM [3, 8] and therefore, enabling the estimation of 3D information. In this paper, we present 3D displacement measurements obtained with both, thin-shell theory and with multiple sensitivity directions and draw some conclusion about applicability of the thin-shell approach.

3.2 Thin-Shell Modeling of the TM

The shape, planar dimensions, and thickness of the TM vary among various vertebrate species. Thickness values between 50 and 150 μm in several TMs of humans of different ages are reported [9]. Figure 3.1 shows thin-shell like characteristics of the human TM.

Based on a classical mechanics criterion, a membrane can be considered as a thin-shell if the maximum ratio of its thickness to radius of curvature is less than 0.05, which is usually the case for mammalian TMs, so that they can be considered thin-shells.

As reported in our earlier publications [3, 8], combining the measured component of displacement along the system's optical axis ($\boldsymbol{d}_z$), with the x, y, and z components of the normal vector obtained by the shape of the TM, displacement maps along the x- and y-axes, $\boldsymbol{d}_x$ and $\boldsymbol{d}_y$, can be computed with

$$\boldsymbol{d}_x = \boldsymbol{n}_x \frac{\left|\vec{d}_z\right|}{\left|\vec{n}_z\right|}, \text{and} \tag{3.1}$$

$$\boldsymbol{d}_y = \boldsymbol{n}_y \frac{\left|\vec{d}_z\right|}{\left|\vec{n}_z\right|}. \tag{3.2}$$

Figure 3.2 shows estimation of the 3D components of displacements with thin-shell hypothesis using measured shape and 1D sound-induced component of displacements for a chinchilla TM.

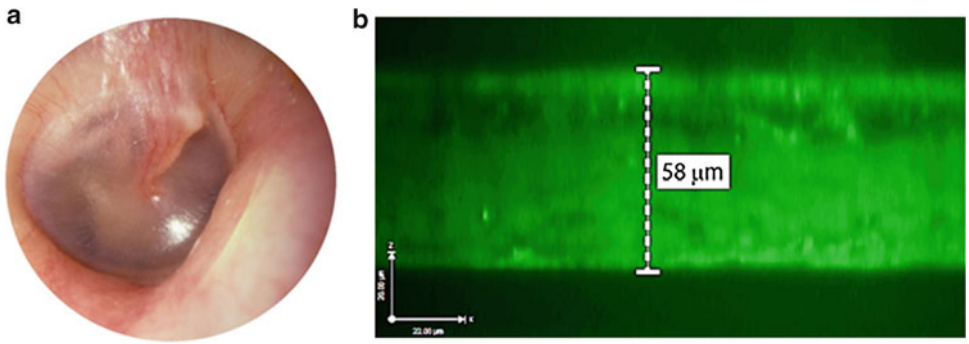

Fig. 3.1 Some characteristics of the human TM: (**a**) semi-transparent nature; and (**b**) confocal image showing a thickness that is smaller than its radius of curvature [10]

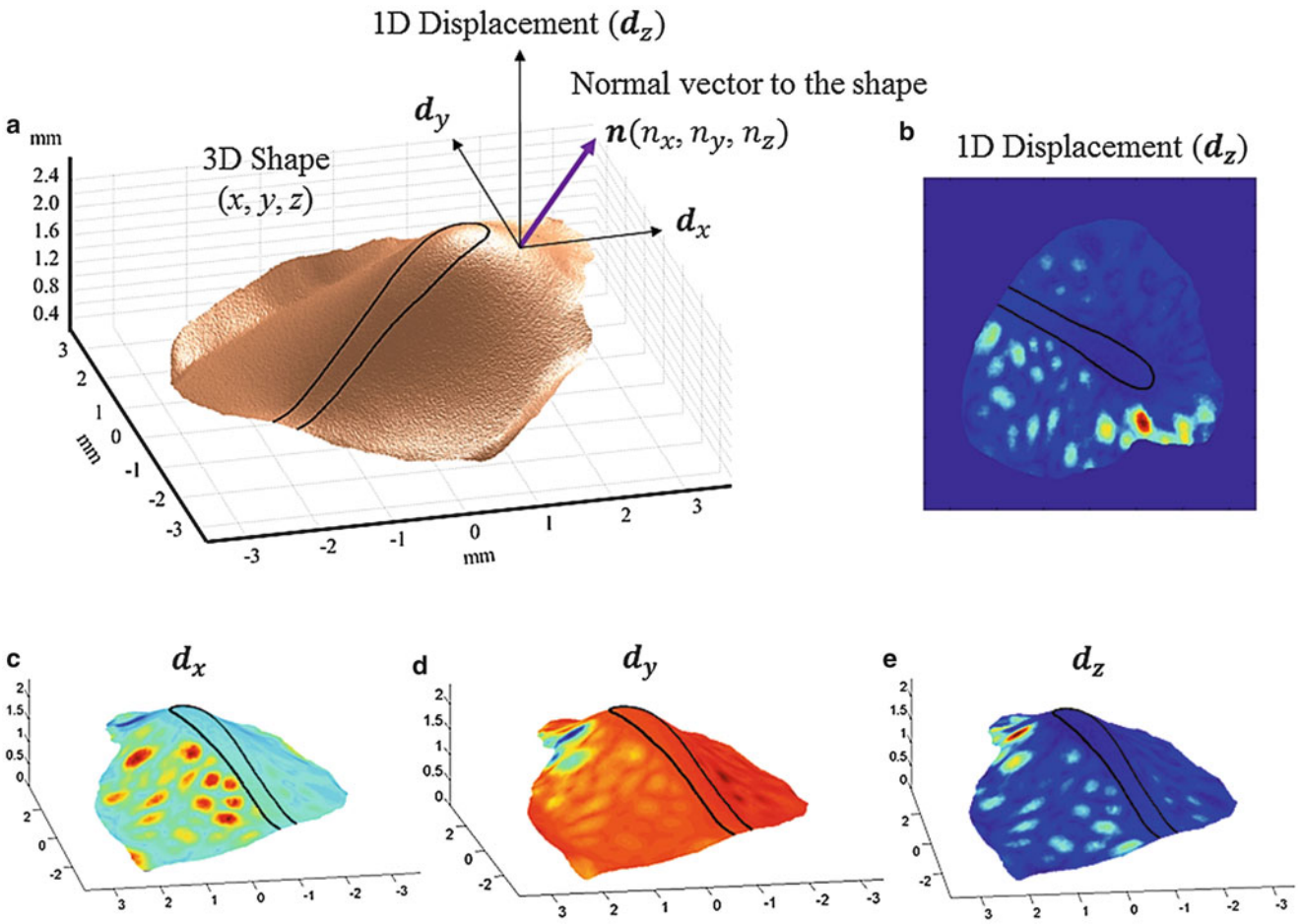

Fig. 3.2 Application of thin-shell theory to recover 3D components of displacement from shape and only 1D displacement measurements: (**a**) shape of the TM to determine surface normal vectors; (**b**) 1D displacement measurements of the TM through lateral axis (z-axis); (**c, d**), and (**e**) are recovered *x*- and *y*-axes, and measured z-axis of displacement, superimposed on the shape of the TM, respectively. The TM was subjected to sound stimuli of 5,730 Hz at the sound pressure level of 101 dB SPL

3.3 Methods to Test the Thin-Shell Theory

Shape and 3D sound-induced motion of the TM are measured with Digital Holographic Interferometric (DHI) techniques. The Fresnel-Kirchhoff integral is used for the numerical reconstruction of the holograms at the image plane from the backscattered light that is recorded at the CCD plane [8, 11]. The optical phase is recovered by the method of four phase-stepping with steps of 90° [12].

3.3.1 Shape Measurements

Two-wavelength holographic contouring technique [13] is applied to generate depth contours related to the geometry of the TM. In two-wavelength contouring, the height at each point on the surface of the object, Z(x, y), is calculated with

$$\mathrm{Z(x,y)} = \frac{\Omega(\mathrm{x,y}) \cdot \Lambda}{4\pi}, \tag{3.3}$$

where Ω(x, y) is the fringe-locus function and Λ is the synthetic wavelength defined by

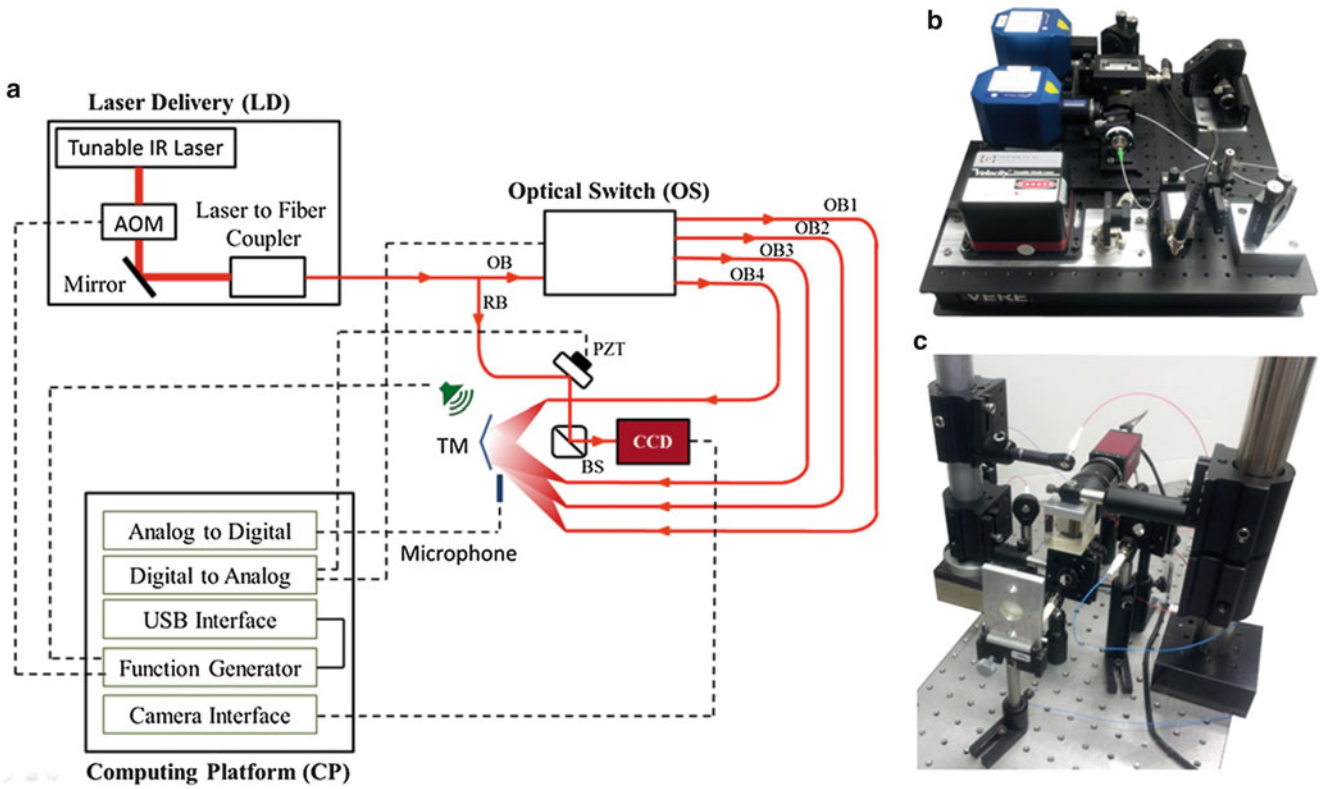

Fig. 3.3 Realization of a holographic system that can measure both, shape and 3D components of displacements using multiple sensitivity vectors: (**a**) schematic of the system using a single external cavity tunable laser; (**b**) an alternative laser delivery system consisting of three external cavity tunable lasers; and (**c**) optical head with multiple single-mode optical fibers for sample illumination

$$\Lambda = \frac{\lambda_1 \lambda_2}{|\lambda_1 - \lambda_2|}, \tag{3.4}$$

where λ_1 and λ_2 are the two wavelengths utilized during recordings, respectively.

3.3.2 3D Displacement Measurements

Full-field-of-view 3D displacement maps are obtained by the method of multiple sensitivity vectors. At least three sensitivity vectors are required to measure all three components of the displacement vector. However, to minimize the errors, phase maps obtained by stroboscopic measurements from four sensitivity vectors are imported into a system of equations and the displacement vector at each point is calculated by the least-squares method [11] with

$$\boldsymbol{d} = \left\{ [K]^T [K] \right\}^{-1} [K]^T \{\Omega\}, \tag{3.5}$$

where $\boldsymbol{d}$ is the displacement vector, $[K]$ is the sensitivity matrix, and $\{\Omega\}$ is the fringe-locus function vector. Figure 3.3 shows the realization of a 3D holographic system that can measure shape and 3D sound-induced displacements of the TM.

3.4 Results Through Test and Validation of the Thin-Shell Theory

To test the thin-shell theory, full-field-of-view, 3D sound-induced components of displacement are measured and compared with the ones obtained by the thin-shell theory. Also, resultant displacements obtained from both approaches, thin-shell theory and experimental tests, are compared with each other.

3.4.1 Comparisons of the 3D Motion of the TM

In vitro TM samples were prepared following standard procedures [3] and 3D sound-induced displacement components were measured at different tonal frequencies and amplitudes. As an example, Fig. 3.4 shows representative comparisons between 3D measurements obtained with multiple sensitivity vectors and with the ones obtained by the use of the thin-shell approach. The correlation coefficients are 0.81 and 0.88 for displacements along x, and y axes, respectively.

3.4.2 Resultant Sound-Induced Displacements

Resultant displacements obtained with multiple sensitivity vectors and with the thin-shell theory approach are compared. Figure 3.5 shows representative results of comparisons for two TM species. Based on our measurements, we observe that the correlation coefficients between the two approaches decrease as the excitation frequencies increase, even though, in most of the cases, the comparisons show correlation coefficients ($\mathbb{R}$) greater than 90 %.

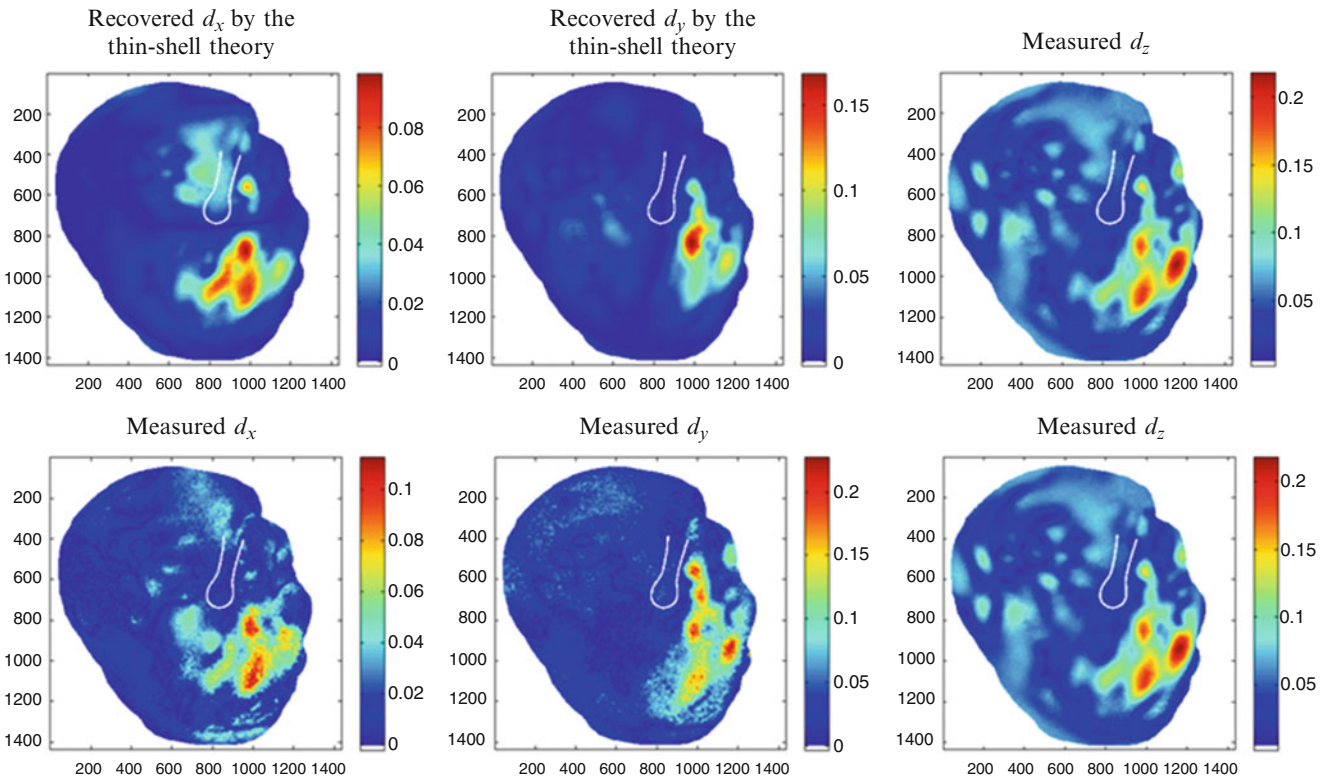

Fig. 3.4 Characterization of 3D acoustically-induced displacements of a human sample in vitro by multiple sensitivity vectors and by our proposed thin-shell approach. Comparisons indicate correlation coefficients of 0.81 and 0.88 for displacements along the x, and y axes, respectively

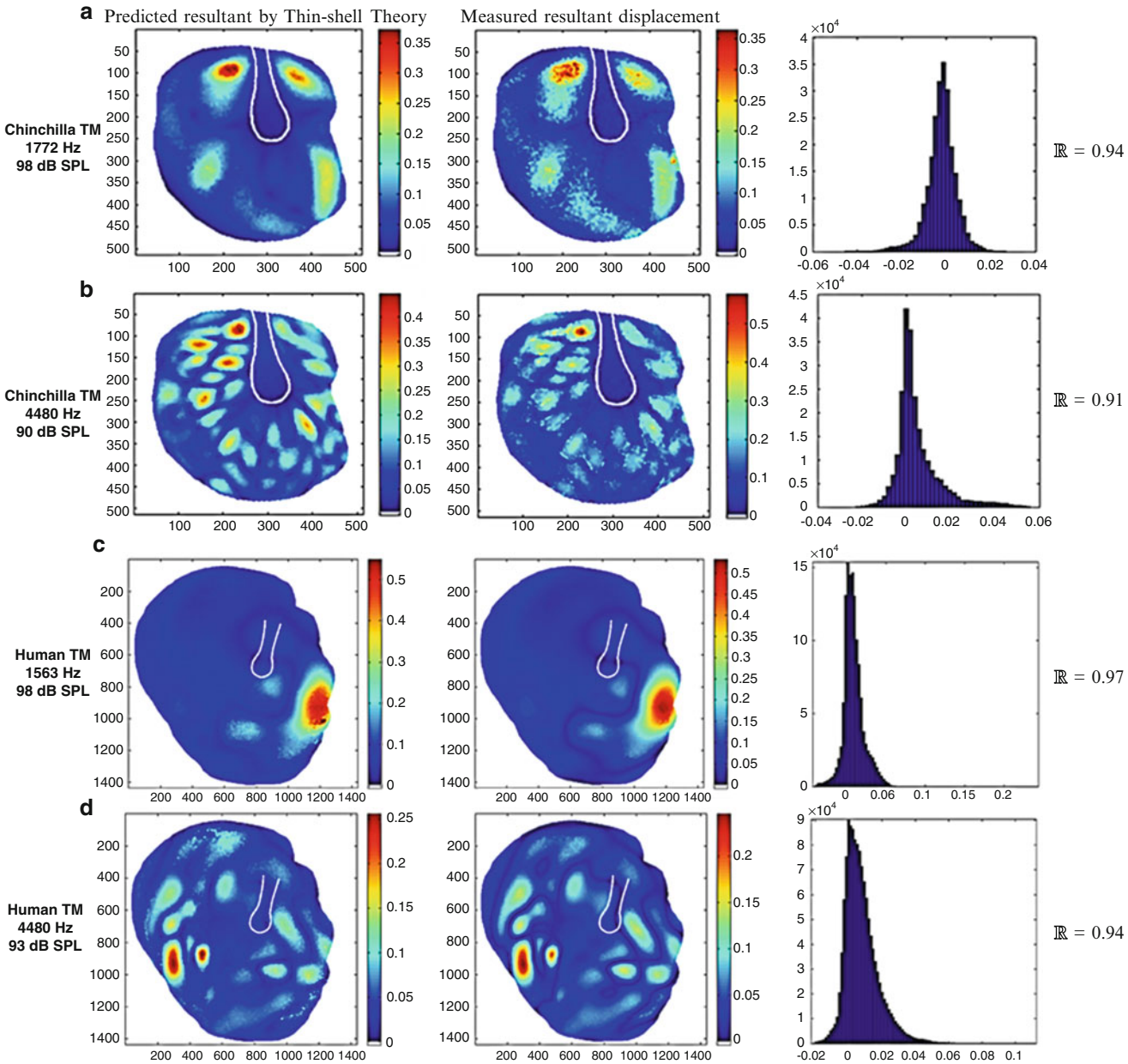

Fig. 3.5 Comparisons between resultant 3D acoustically-induced displacements obtained with multiple sensitivity vectors and thin-shell approach for two species: (**a**) and (**b**) chinchilla TM excited at 1772 Hz, at 98 dB SPL, and 4480 Hz, at 90 dB SPL, respectively; (**c**) and (**d**) human TM excited at 1563 Hz, at 98 dB SPL, and 4480 Hz, at 93 dB SPL, respectively. The corresponding histograms of the differences between both approaches are shown on the right. Correlation coefficients in all cases are greater than 90 %

3.5 Conclusions

Due to the confined geometry of the ear canal, we established a hypothesis to model the TM as a thin-shell in order to facilitate 3D displacement measurements. Based on the hypothesis, the displacement vectors at every point on the surface of the TM are parallel to the normal vectors corresponding to the shape of the TM. Therefore, it is possible to estimate 3D displacements by measuring 1D component of displacements and the shape of the TM. To test the thin-shell hypothesis, we developed 3D digital holographic systems for near simultaneous measurements of shape and 3D acoustically-induced displacements of TM. Our holographic systems have a measuring range spanning nearly five orders of magnitude, from millimeter (in shape measurement) to sub-micrometer (in 3D displacement measurement). The holographic systems are used

to measure 3D displacements, which are compared with a thin-shell approach. Measurements are performed on two different species and preliminary results indicate that the thin-shell approach is applicable at low and mid-range excitation frequencies, which indicate that the displacement vectors on the surface of the membrane are mainly out-of-plane (parallel to the normal vector of the TM), and displacement components tangent to the surface of the TM are negligible.

Acknowledgements This work has been funded by the National Institute on Deafness and Other Communication Disorders (NIDCD), the National Institute of Health (NIH), the Massachusetts Eye and Ear Infirmary (MEEI), and the Mittal Fund.

References

1. Puria S, Steele C (2010) Tympanic-membrane and malleus–incus-complex co-adaptations for high-frequency hearing in mammals. Hear Res 263(1):183–190
2. Khaleghi M, Dobrev I, Harrington E, Furlong C, Rosowski JJ (2014) Study of the transient response of tympanic membranes under acoustic excitation. In: Proceedings of SEM 2013, mechanics of biological systems and materials, vol 4. Springer, New York, pp 1–9
3. Rosowski JJ, Dobrev I, Khaleghi M, Lu W, Cheng JT, Harrington E, Furlong C (2012) Measurements of three-dimensional shape and sound-induced motion of the chinchilla tympanic membrane. Hear Res 301:44–52
4. Rochefoucauld O, Olson ES (2010) A sum of simple and complex motions on the eardrum and manubrium in gerbil. Hear Res 263(1):9–15
5. Khaleghi M, Furlong C, Cheng JT, Rosowski JJ (2014) 3-dimensional quantification of surface shape and acoustically-induced vibrations of TM by digital holography. In: Proceedings of Fringe 2013. Springer, Berlin, pp 599–602
6. Schmidt T, Gerhardt U, Kupper C, Manske E, Witte H (2013) A miniaturized laser-Doppler-system in the ear canal. Proc SPIE 9, 85651N
7. Decraemer WF, Khanna SM, Funnel WRJ (1994) A method for determining three-dimensional vibration in the ear. Hear Res 77:19–37
8. Khaleghi M, Lu W, Dobrev I, Cheng JT, Furlong C, Rosowski JJ (2013) Digital holographic measurements of shape and three-dimensional sound-induced displacements of Tympanic Membrane. Opt Eng 52(10), 101916
9. Decraemer WF, Funnell WRJ (2008) Anatomical and mechanical properties of the tympanic membrane. In: Ars B (ed) Chronic otitis media. Pathogenesis-oriented therapeutic management. Kugler, The Netherlands, pp 51–84
10. Aernouts J, Aerts JRM, Dirckx JJJ (2012) Mechanical properties of human tympanic membrane in the quasi-static regime from in situ point indentation measurements. Hear Res 290(1):45–54
11. Kreis T (2005) Handbook of holographic interferometry: optical and digital methods. Wiley, Weinheim, pp 243–255
12. Yamaguchi I, Zhang T (1997) Phase-shifting digital holography. Opt Lett 22(16):1268–1270
13. Furlong C, Pryputniewicz RJ (2000) Absolute shape measurements using high-resolution optoelectronic holography methods. Opt Eng 39(1):216–223

Chapter 4
Controlling Abalone Shell Architecture with Temperature

MariAnne Sullivan and Barton C. Prorok

Abstract Biomimetics is a growing field, and abalone shells have become a recently studied topic because of their amazing strength properties. Their shell is composed of calcium carbonate, and it is formed by the mollusk in a unique structure of interlocking tablets called nacre, also known as mother of pearl. There has been much interest in the interactions between tablets, but there are also structural growth lines that occur between layers of nacre that have been unnoticed by other researchers. With these additional non-nacre layers, the material's strength is increased. We show how abalones can be cultured with changes in temperature to adjust shell and nacre growth. Then, they are tested using nanoindentation for qualitative mechanical data. In all, we aim to utilize the abalone nacre architecture based on these composite layers for improved strength applications such as protective armor.

Keywords Biomimetics • Nanoindentation • Multilayer composites • Biomineralization • Nacre

4.1 Introduction

Abalones are a type of mollusk found in saltwater that have very intricate shells. Their shiny underside is known as mother-of-pearl, and is used for aesthetic applications such as jewelry or guitar frets. Besides its outer beauty, the abalone shell also has inner strength. Its components are a mix of organic and inorganic substances, and its structure is called nacre. The inorganic is calcium carbonate, or solely chalk, but because the abalone grows in such an ornate manner, the nacre has 3,000 times the strength of its individual components [1]. The nacre is composed of layers upon layers of tablets that are about eight microns in diameter [2], and there have been many thoughts as to why this nacre is so strong. Mechanical tests have been completed, from miniature tensile tests to atomic force microscopy to nanoindentation [3–6]. In this research, scanning electron microscopy (SEM) is the primary tool for qualitative measurements of the abalones shell structure. Following observed trends, nanoindentation is used for quantitative clarification.

Biomimetics is such an interesting topic because nature has been using the best practices to create strong and the most effective materials. The abalone shell is amazing because its nacre is formed automatically by the animal. In our research group, abalones are being raised in the lab so as to study their growth patterns. While other researchers have been focused on the intricacies of the nacre itself and this individual tablets and their interactions, there is more to the abalone shell than solely the nacre. It is seen that wild abalones have a completely different overall structure than ones that are farm raised in large aquariums. The farmers have constant conditions such as food and temperature that are chosen for the fastest growing abalone. In the wild, however, conditions are limited and temperature fluctuations are constant. The wild abalones have extra growth lines that are a different structure than the nacre. Farm raised abalones, however, have a constant pattern. The differences are seen in Fig. 4.1. Not only are there visual, qualitative differences, but there is nanoindentation data that shows the wild is stronger than the farm raised abalone. In Fig. 4.2, elastic modulus is plotted vs. displacement for both types of abalone. The wild is about 20 GPa stronger than the farm raised. Nature is amazing and it is interesting that there is such a large difference. Because the growth lines are apparent within the SEM images, it is believed that these structure differences attribute to the increased strength of the wild abalones.

M. Sullivan • B.C. Prorok (✉)
Department of Mechanical Engineering, Auburn University, 275 Wilmore Laboratories, Auburn, AL 36849, USA
e-mail: prorok@auburn.edu

F. Barthelat et al. (eds.), *Mechanics of Biological Systems and Materials, Volume 7: Proceedings of the 2014 Annual Conference on Experimental and Applied Mechanics*, Conference Proceedings of the Society for Experimental Mechanics Series,
DOI 10.1007/978-3-319-06974-6_4,

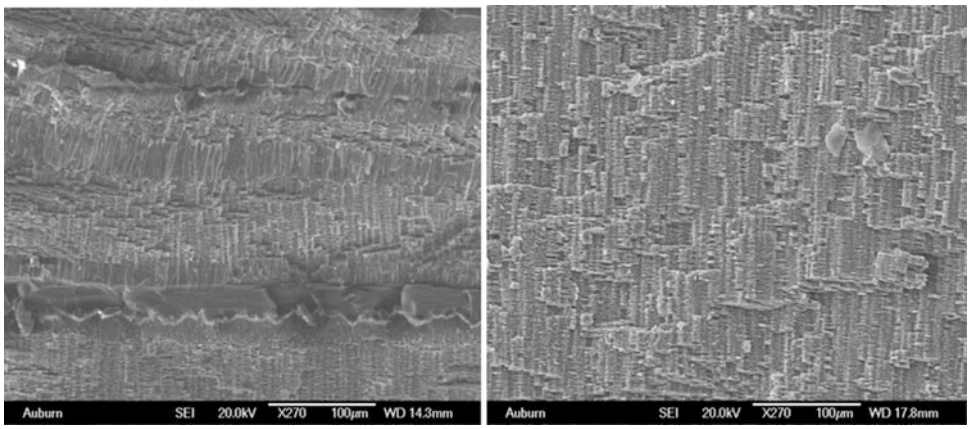

Fig. 4.1 Wild abalone structure with *growth lines* (*left*) compared to farm raised abalone continuous nacre (*right*)

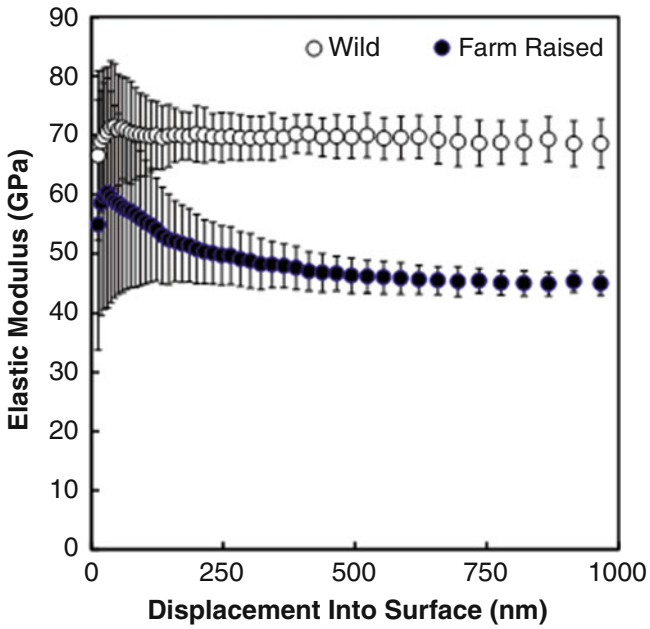

Fig. 4.2 Nanoindentation data of elastic modulus vs. displacement into surface for wild and farm raised abalone

If the abalone shell structure could be replicated with other materials, it could provide an improved material for protective applications. The abalones are able to protect themselves from predators such as octopi and otters. With improved material selection but mimicking the architecture of the abalone shell, with both the nacre structure and the growth layers, there could be a new type of material for these kinds of applications.

4.2 Experimental Procedure

Abalones were obtained from California and shipped on ice to Alabama. There was a revival process, where only a few of the abalones survived. After acclimating the animals for a month, their growth patterns were studied. A method pioneered by researchers at UC Santa Barbara was utilized, called the flat pearl technique [7]. Figure 4.3 shows the placement of 10 mm glass coverslips that were glued with underwater glue. First, the methods were studied to see growth patterns of constant temperature, 62 °F. SEM was used to visualize the growth patterns. After the initial tests were completed at constant

Fig. 4.3 Flat pearl technique implemented on abalones in the lab

temperature, next a cold region was implemented in between the normal temperatures. The tanks were decreased by 5–57 °F. Then, abalones were studied in the SEM again and differences in the structures were noted, discussed below. Nanoindentation was completed using an MTS Nanoindenter XP with continuous stiffness measurements and a Berkovich three-sided pyramid indenter tip.

4.3 Results and Discussion

First, the flat pearl technique was shown to be successful at studying the effects on temperature in a short amount of time. Another benefit is that the abalone are not harmed, and the same animal can be used for repeated tests. This helps when repeating tests. During the constant temperature range, the constant nacre structure was seen after a prismatic layer was first deposited on the foreign object placed in the abalone, seen in Fig. 4.4. Because the abalone is getting acquainted to the new implants, it seems to take a few weeks before the nacre formation starts. Also, the mantle needs to be covering the abalone before growth can occur. In Fig. 4.3, the mantle is pulled back to see the inserted cover slips, and sometimes the animal takes a few days to become comfortable and cover the slides to begin growing again.

After 7 weeks at a constant temperature, similar trends are seen. The abalone still places a prismatic non-nacre layer on the cover slip before nacre can form. When the temperature is kept constant, the nacre grows continuously. Because all other parameters are kept constant, such as sustenance, the nacre growth is also constant. When there is a change in temperature, however, the abalone growth patterns also change. Figure 4.6 demonstrates there is a non-nacre layer forming when there are now three temperature regimes. The temperature pattern is shown in Fig. 4.5.

Although there is only a slight change in the temperature, the structure greatly changes. Compared to the nacre structures seen in the previous image, growth lines are now apparent that match the wild abalone structure. There is only one growth line in the middle of the sample, so it is believed that during this colder temperature, the abalone grows differently. Even though this may be thought to be a problem for the abalone, either being without food or in a less desired condition, the animal is still growing. This altered growth line that is different from the nacre actually adds to the strength, as shown in the previous nanoindentation data.

The structure seen in Fig. 4.6 has first, the prismatic layer on the bottom. This is followed by nacre, then a growth line, and nacre again. There is some trigger that makes the abalone grow differently at a colder temperature. Because this structure is stronger than sole nacre, if the architecture could be used with other materials, then it would provide a strong protective material. Nanoindentation needs to be completed on these portions of the abalone and compared. There is some difficulty in these tests because when the implants are embedded for a couple months, the abalone seems to completely absolve the glass slide, and it is impossible to remove. This shows how adaptable and strong the abalone can be, but it is not helpful for our testing. New substrates may be used in the future that will allow for a smaller prismatic layer and longer growth times to be studied.

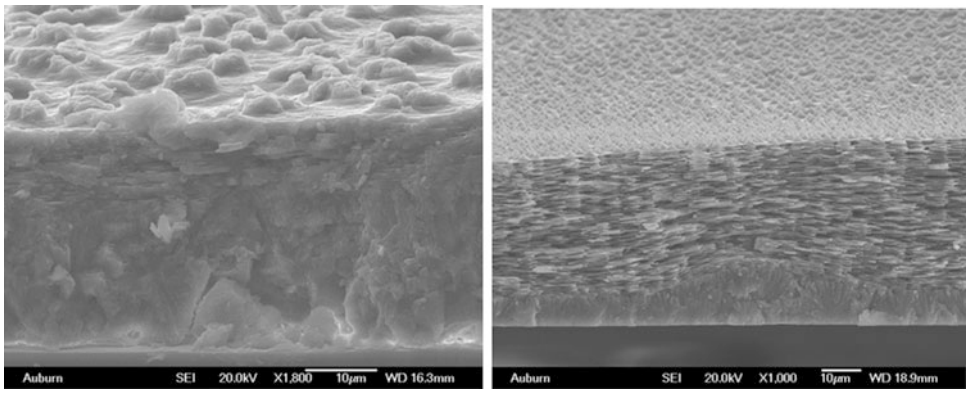

Fig. 4.4 Four weeks' growth at constant temperature (*left*) and seven weeks' growth at constant temperature (*right*)

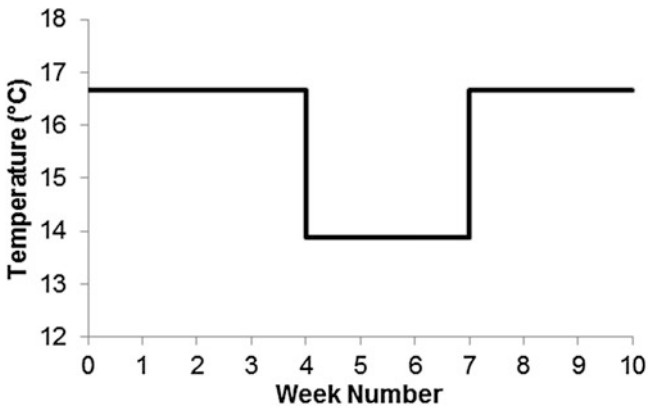

Fig. 4.5 Temperature regimes where non-nacre regions form in the colder temperature

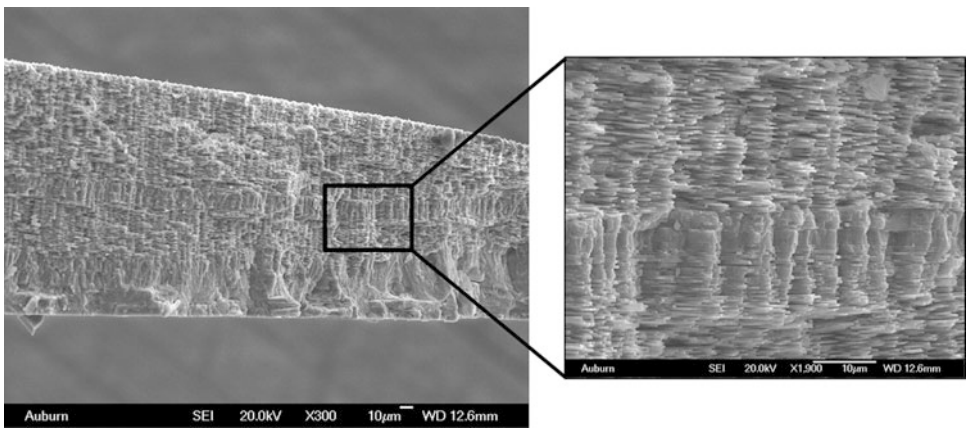

Fig. 4.6 *Left*, edge of growth from abalone from changing temperatures; *right*, closer image of the non-nacre regions of growth expected during the cold regime

4.4 Conclusions

Overall, it is concluded that abalone growth can be monitored in the lab setting. Changing temperature affects the abalone growth. The extra growth lines are present only when there are temperature changes, and solely a 5 °F change is able to affect the growth. To imagine the abalones in their natural habitats, there are fluctuations based on seasons and tidal changes, so it makes sense that these patterns would attribute to their growth. What is novel in these findings is that despite it being a

natural process with temperature changes, the growth lines add to the strength of the abalone. Acting like multilayer composites, the growth lines provide a place for crack deflections to further strengthen the shell. Not only is nacre an amazing structure, but the growth of the abalone shell with temperature changes increases the strength properties even more. The next step is to study these patterns and the differences in strength using nanoindentation techniques. The next question is if the abalones are utilizing this multilayer composite to its greatest potential, or if it is possible to induce the abalone to create even stronger architectural patterns. In the long term, it may be possible to use this architecture with other materials to provide better structures for protective applications, such as armor.

References

1. Currey JD (1977) Mechanical properties of mother of pearl in tension. Proc R Soc Lond Ser B Biol Sci 196:443–463
2. Barthelat F, Li C-M, Comi C, Espinosa HD (2006) Mechanical properties of nacre constituents and their impact on mechanical performance. J Mater Res 21:1977–1986
3. Lin AY-M, Meyers MA (2009) Interfacial shear strength in abalone nacre. J Mech Behav Biomed Mater 2:607–612
4. Li X, Chang W-C, Chao YJ, Wang R, Chang M (2004) Nanoscale structural and mechanical characterization of a natural nanocomposite material: the shell of red abalone. Nano Lett 4:613–617
5. Meyers MA, Lim CT, Li A, Hairul Nizam BR, Tan EPS, Seki Y, McKittrick J (2009) The role of organic intertile layer in abalone nacre. Mater Sci Eng C 29:2398–2410
6. Espinosa HD, Juster AL, Latourte FJ, Loh OY, Greegoire D, Zavattieri PD (2011) Tablet-level origin of toughening in abalone shells and translation to synthetic composite materials. Nat Commun 2, 173
7. Fritz M, Belcher AM, Radmacher M, Walters DA, Hansma PK, Stucky GD, Morse DE, Mann S (1994) Flat pearls from biofabrication of organized composites on inorganic substrates. Nature 371:49–51

Chapter 5
The Modeling of Time Dependent Mechanical Properties of Cervine Enamel

Y.-J. Syu, R.-L. Lin, and N.-S. Liou

Abstract This work investigated the time dependent mechanical properties of cervine enamel. Three point bending tests were used to investigate mechanical properties of cervine enamel. The specimens of enamel were prepared from cervine incisors and the ramp-hold three point bending tests were performed to acquire the force-time and displacement-time relation of enamel specimens under three point bending load. The finite element analysis of specimen under three point bending load was performed by applying the three point bending ramp-hold displacement-time boundary condition to the plane strain finite element model of specimen and the reaction force of the loading tip was recorded. In this study, cervine enamel was considered as linear viscoelatic material. The long-term elastic modulus of enamel was evaluated from the stress and strain relations at the end of ramp-hold tests and the relaxation behaviour of enamel was estimated from the force-time and displacement time curves of three point bending ramp-hold tests. An inverse iterative finite element analysis procedure was developed to obtain the long-term elastic modulus, relaxation coefficients and characteristic times of linear viscoelastic model of cervine enamel. The results show that a linear viscoelastic model with two relaxation time constants can well describe the time dependent behaviour of cervine enamel.

Keywords Biomechanics • Enamel • Cervine • Bending Test • Viscoelastic

5.1 Introduction

Enamel, forming the hardest part of mammal tooth, is a biological hierarchical composite and has attracted significant interest from material and mechanical scientists due to its excellent mechanical properties. The understanding of mechanical properties of enamel can benefit the development of bio-inspired composite materials. The time dependent mechanical properties of hard tissue such as bone which has attracted significant attention; however, enamel has long been considered as an elastic biological material due to its high inorganic content. Recent investigations have shown the inelastic properties of enamel [1, 2]. In this study, the time dependent mechanical properties of cervine enamel under bending load were investigated by using three point bending tests. Ramp-hold three point bending tests were used to examine the time dependent mechanical behavior of beam type enamel specimens. The specimens were prepared from cervine incisors. The linear viscoelastic model was used to describe the time dependent behavior of enamel under three point bending load. The inverse iterative finite element analysis procedure was used to obtain the relaxation coefficients and characteristic times of enamel.

Y.-J. Syu • R.-L. Lin • N.-S. Liou (✉)
Department of Mechanical Engineering, Southern Taiwan University of Science and Technology, No. 1, Nan-Tai Street, Yongkang District, Tainan City 710, Taiwan ROC
e-mail: nliou@mail.stust.edu.tw

F. Barthelat et al. (eds.), *Mechanics of Biological Systems and Materials, Volume 7: Proceedings of the 2014 Annual Conference on Experimental and Applied Mechanics*, Conference Proceedings of the Society for Experimental Mechanics Series,
DOI 10.1007/978-3-319-06974-6_5,

5.2 Material and Methods

The enamel material for test was obtained from cervine incisors (Fig. 5.1a). The cervine incisors were extracted and encapsulated in cold mounting epoxy (Fig. 5.1b), and the encapsulated incisors were sectioned to 1 mm thick slices (Fig. 5.1c). The thickness of enamel layer of cervine incisor is about 1 mm. The cervine enamel specimens for three point bending tests were prepared by using low speed saw from the slices of incisor and the height of beam type specimens is about 0.5 ~ 1 mm and the length of specimens varies from 7 to 10 mm (Fig. 5.2).

In order to obtain the parameters of linear viscoelastic constitutive model, ramp-hold three point bending tests (Fig. 5.3a) were carried out by using Instron tensile test machine (Fig. 5.3b). The distance between two lower supports is 6 mm and the diameter of supports and loading tip is 0.5 mm. The displacement rate and total displacement of loading tip is 0.001 mm/s and 0.01 mm respectively. The procedure of the ramp-hold bending test consists of two steps. In the first step, the displacement of loading tip increases linearly until the center deflection of specimen reaches 0.01 mm. The deflection is held for a total time of 200 s in the second step. At the end of first step, the reaction force reaches the maximum value and the reaction force decreases due to the time dependent mechanical properties of dentine during the second step. The force-time curve was used to investigate the viscoelastic properties of cervine enamel.

The linear viscoelastic model was used to describe the relaxation behavior of cervine enamel due to its simplicity and can be easily implemented to finite element models. In this study, linear viscoelastic model with two time constants was used and the Prony series of this model can be expressed as follows:

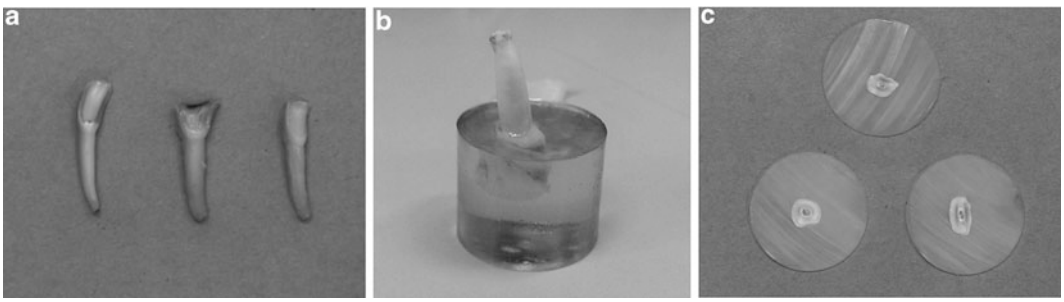

Fig. 5.1 (**a**) Cervine incisors, (**b**) incisor embedded in cold molding epoxy and (**c**) slices of cervine incisor and epoxy

Fig. 5.2 (**a**) Slice of cervine enamel was cut by (**b**) low speed saw to make (**c**) enamel specimens for bending tests

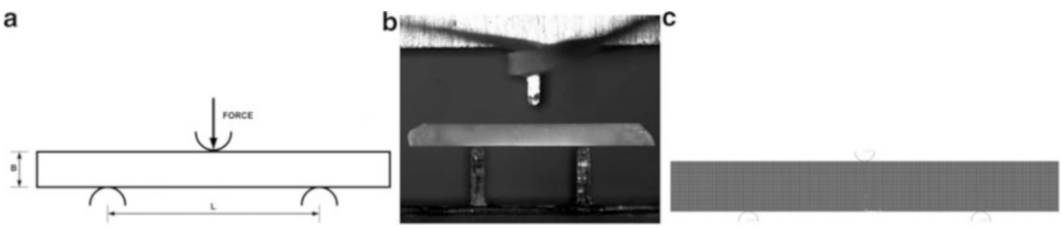

Fig. 5.3 (**a**) Schematic and (**b**) experimental setup of three points bending ramp-hold test and (**c**) corresponding FEA model

$$E_R(t) = E_0 \cdot \left(1 - \sum_{i=1}^{2} g_i \cdot \left(1 - e^{-t/\tau_i}\right)\right). \tag{5.1}$$

In Eq. (5.1), E_R, E_0, g_i and τ_i are relaxation modulus, instantaneous modulus, Prony constant and time constant respectively. The generalized pattern search method and finite element analyses were used for the optimization process to obtain the parameters of linear viscoelastic model [3, 4]. In this study, plane strain FE model was used (Fig. 5.3c). The model consists of two rigid supports, one rigid loading tip which applied center deflection to the specimen. The pattern search optimization process was used to find out the best fit parameters of viscoelastic mechanical model of cervine enamel under bending load.

5.3 Results and Discussion

The force-time curves of cervine enamel specimens under ramp-hold three point bending tests are shown in Fig. 5.4a and the average long-term elastic modulus computed from the force–deflection relation at the end of ramp-hold experiments (200 s) is about 19 GPa (n = 3). This value is lower than the elastic modulus of cervine enamel reported by using nanoindenter. The possible reason is due to the micro cracks in the specimen which reduce the bulk stiffness of specimen. The displacement of loading tip is under open loop control since, for the test machine used in this study, close loop control for such a small displacement (0.01 mm) will cause the oscillation of holding displacement. The displacement of loading tip monitored by extensometer is shown in Fig. 5.4b. Due to the compliance and backlash of test machine, the actual holding displacement of loading tip is about 60 ~ 80 % of target displacement (0.01 mm). This discrepancy should be taken into consider is the calculation of stress and elastic modulus.

In order to obtain the relaxation behavior of enamel under three point bending condition, the force-time curves were normalized and the average was computed (Fig. 5.5). It can be seen that the mechanical behavior of cervine enamel is time dependent. The averaged normalized force-time curve was used to evaluate the relaxation constants of cervine enamel by using iterative inverse finite element method and, for linear viscoelatstic model with two time constants, the best fit time constants and relaxation factors are $g_1 = 0.07$, $g_2 = 0.05$, $\tau_1 = 10$ and $\tau_2 = 137$ respectively.

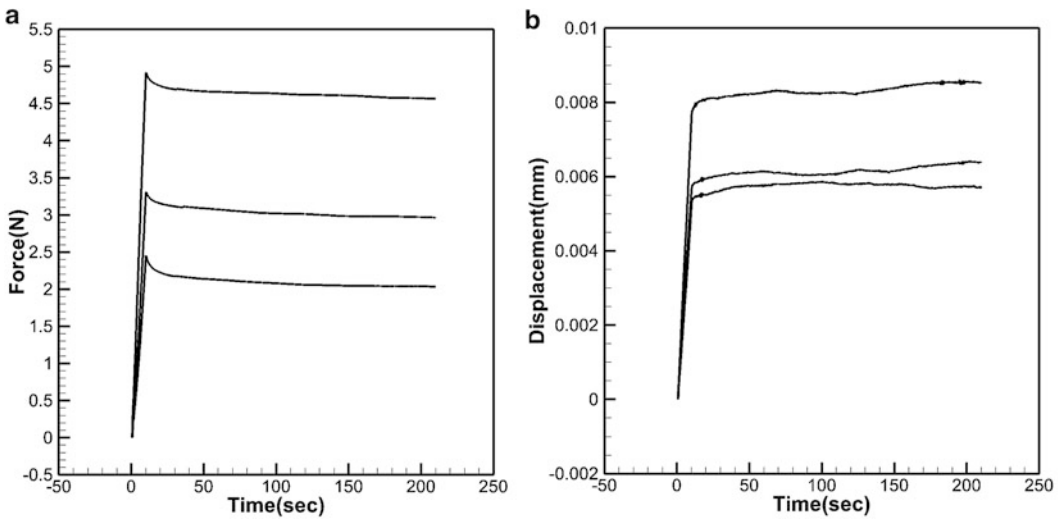

Fig. 5.4 (**a**) The force-time curves (**b**) and displacement of loading tip monitored by extensometer

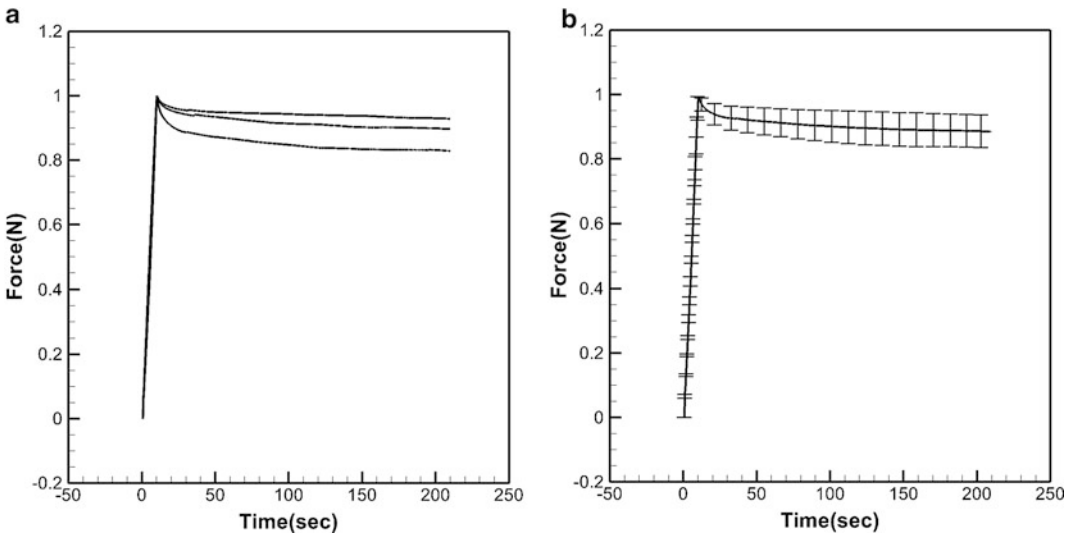

Fig. 5.5 (**a**) The normalized force-time curves and (**b**) the averaged and standard deviation of normalized force-time curves

5.4 Conclusion

This study showed that the cervine enamel is a time-dependent material. Although the elastic modulus of cervine enamel obtained from this study is lower than the elastic modulus of enamel reported elsewhere. However, the findings of the relaxation trend under mechanical load still provide important information for developing more faithful constitutive models of enamel.

Acknowledgement This research was supported by NSC 101-2221-E-218 -026 -MY3 from the R.O.C government.

References

1. He LH, Swain MV (2009) Nanoindentation creep behavior of human enamel. J Biomed Mater Res Part A 91A:352–359
2. Schneider GA, He LH, Swain MV (2008) Viscous flow model of creep in enamel. J Appl Phys 103:014701
3. Namani R, Simha N (2009) Inverse finite element analysis of indentation tests to determine hyperelastic parameters of soft-tissue layers. J Strain Anal Eng Des 44:347–362
4. Lei FL, Szeri AZ (2007) Inverse analysis of constitutive models: biological soft tissues. J Biomech 40:936–940

Chapter 6
Development of Tissue Surrogates for Photoelastic Strain Analysis of Needle Insertion

Rachel A. Tomlinson, Wei Kang Aui Yong, Guy Morton, and Zeike A. Taylor

Abstract This paper focuses on the development of full-field experimental methods for validating computational models of needle insertion, and specifically the development of suitable tissue surrogate materials. Gelatine also known as "ballistic gel" is commonly used as a tissue surrogate since the modulus of elasticity matches that of tissue. Its birefringent properties also allow the visualisation of strains in polarised light. However, other characteristics of tissue are not well emulated by gelatine, for example the fibrous network of cells of tissue is not well represented by the granular microstructure of gelatine, which tears easily. A range of birefringent flexible materials were developed and calibrated for photoelastic analysis. The most suitable were then used to explore quantitatively the different strain distributions in tissue when subjected to a range of needles with different tip profiles.

Keywords Tissue surrogate • Birefringent • Gelatine • Needle insertion

6.1 Introduction

Needle insertion is a common surgical procedure used in everything from drug administration to biopsy extraction. Many such applications would benefit from robust and flexible numerical models of the needle insertion process. For example during a biopsy procedure, the hollow needle, usually with a notch at the tip, will be guided with the aid of ultrasound to cut small tissue samples and remove them from the body. Guidance problems may arise when the targeted area is deep in the body, requiring a relatively large distance to be travelled by the needle tip. Also the tip of the needle is not symmetrical and so forces acting on the tip will be uneven, consequently resulting in bending of the needle in the body during insertion [1–3]. The bending can cause inaccuracy in the needle placement and consequently the needle tip may miss cancerous tissue and result in mis-diagnosis [4]. Normally doctors will perform 3–6 insertions each session in order to avoid such mis-diagnosis thus making the procedure time quite lengthy for the patient. Additionally if one considers small breast lesions for example, during biopsy the target could move as the needle indents and punctures the skin layer [5]. The target could penetrate deeper into the breast soft tissue, making it more difficult for the needle to reach the lesion. Lesion movements were tracked with ultrasound images and it was found that insertion force and target displacement increase by 90.2 and 275.9 % respectively, when the skin thickness is increased from 0 to 2.5 mm. Modelling the needle insertion could improve the reliability of needle placement within a body by predicting tissue and needle deflections.

Although computational modelling of complex human tissue systems is now a real possibility due to advancements in mathematical and numerical techniques, such models need validating. Ethical issues clearly limit validation experiments on human tissue, therefore there is a need to develop tissue surrogates. Photoelastic materials have been used for many years in

R.A. Tomlinson (✉) • W.K. Aui Yong • G. Morton
Department of Mechanical Engineering, The University of Sheffield, Sheffield S1 3JD, UK
e-mail: r.a.tomlinson@sheffield.ac.uk

Z.A. Taylor
Centre for Computational Imaging and Simulation Technologies in Biomedicine, CISTIB, The University of the Sheffield, Mappin St., Sheffield S1 3JD, UK

F. Barthelat et al. (eds.), *Mechanics of Biological Systems and Materials, Volume 7: Proceedings of the 2014 Annual Conference on Experimental and Applied Mechanics*, Conference Proceedings of the Society for Experimental Mechanics Series,
DOI 10.1007/978-3-319-06974-6_6,

dental and medical applications, offering not only mechanical similarity to tissue, but also visualisation of strains. Photoelastic materials exhibit temporary birefringence, such that when loaded and viewed in polarised light, the double-refraction effect results in the observation of interference fringes which relate directly to the shear strains in the material. Birefringent materials such as epoxy resins have been used to represent stiffer materials such as bone and dentine, and gelatine, also known as "ballistic gel", is often used as a surrogate to evaluate penetrating impacts or blast loading effects on soft tissues [6–9]. The use of photoelasticity for tissue analysis has been mainly limited to qualitative analysis since there are many issues which require consideration when developing flexible birefringent surrogate tissue materials for quantitative validation purposes. These include: transparency and birefringent sensitivity; matching the modulus of elasticity to tissue types of different stiffness; physically modelling and quantifying three dimensional systems; modelling viscoelasticity and creep present in tissue materials; representing the fibrous network of tissues' extracellular matrix, particularly when punctured with medical instruments; and the stability of mechanical properties of surrogate materials over time and at different temperatures.

This work focuses on the initial attempts to develop full-field experimental methods for validating computational models of needle insertion, and specifically the development of suitable tissue surrogate materials.

6.2 Mechanical Properties of Tissue

The first step of the development of a surrogate was to investigate mechanical properties of human tissue. The biopsy procedure and tools used are normally similar on all patients, but the mechanical properties of tissue vary according to gender and age group. Also, as the tissue-needle interaction is being investigated, the characteristics of each layer of tissue may have to be considered. For example in a breast cancer biopsy, upon puncturing the skin, the needle may pierce layers of fat, glandular tissue and muscles.

Since with any needle insertion, the tip must first puncture the skin, the mechanical properties of skin were considered first. A study done by Agache et al. shows that the Young's modulus, E, of human skin increases with age [10]. In the study, mechanical properties of the skin were measured on 138 persons, aged from 3 to 89 years old. It was found that elasticity and stretchability of skin deteriorates with age with an average E of 0.42 MPa below 30 years and 0.85 MPa above 30 years old. However, in research by Edwards and Marks [11], the Young's modulus ranged from 15 to 150 MPa. Looking at the mean value, it peaks at about 70 MPa at 11 years old and slowly declines to about 60 MPa at 95 years old. The vast difference in numerical results from these two studies is probably due to the difference in experimental techniques. Agache performed in vivo testing by applying a fixed torque on test subjects and measuring the resulting angle of twist then calculating the modulus of elasticity using a set of equations. Edwards and Marks quoted the work of Vogel where in vitro testing was performed on different human skin samples. Tensile tests to failure were performed on specimens, and the corresponding stress–strain curves plotted. To compare both experiments, the in vitro test by Vogel would be considered more accurate as a test to failure interprets more data compared to a small section done by Agache et al. While this information is useful, the compressive and shearing behaviour of skin was not discussed. Compression, or more precisely, of the puncturing of skin would be more relevant to our study.

Considering the soft tissue layers, Saraf et al. [12] performed experiments on four types of soft tissue: stomach, liver, heart and lung. The tissues were put under hydrostatic compression and simple shear test to get the dynamic response. Their study concluded that the tangent shearing moduli of the four tissues range from 0.008 to 0.34 MPa. In terms of shearing, the liver tissue was found to be stiffest while the lung tissue was the softest. However, the dynamic bulk moduli vary from 150 to 500 MPa, the stomach being the stiffest and the lung again was the softest. In addition, it is stated that these tissues do not possess linear elastic behaviour and the results are just an approximation. Nevertheless, the study fulfilled its primary goal to determine the average mechanical properties of the four tissues.

In a study by Davis et al. [13], the force required to insert a micro-needle into living skin was measured and it was found that the insertion force depends heavily on the sharpness and size of the needle but as the needle punctures the tissue, the fracture toughness could affect the overall strength of the tissue. Taylor et al. [14] found that the value of fracture toughness of skin was highly variable, and depends strongly on the crack growth. They found that specimen size was important since stress and failure energy were seen to be constant for larger specimens with no dependence on crack size. Furthermore, it is of interest that soft tissues were found to be highly tolerant to defects as they could withstand cracks up to several millimetres without losing much strength.

6.3 Development of a Surrogate Tissue Material

The review of mechanical properties of tissue showed that the modulus is highly variable depending on its location and depth, is not linear-elastic and shows some resistance to tearing. A range of materials were tested as potential surrogates, considering: (1) transparency and birefringence; (2) resistance to tearing when punctured; and (3) performance under load. The materials considered were gelatine, gelatine with additives, konjac, agar, and a range of silicone rubbers.

Gelatine-based materials are commonly used to represent soft tissues and several studies have been performed to characterise the mechanical properties of such materials [6–9]. The work by Kwon and Subhash [7] shows that 11 % concentrated gelatine results in a Young's modulus of 10.9 kPa. Their experiment focuses on the strain rate sensitivity of the gelatine and different responses were obtained under different loading conditions. Gelatine concentrations of 5, 7 and 14 % yielded average Young's moduli of 40, 63 and 110 kPa respectively [8]. The difference in stiffnesses between these two studies might be due to the types of raw gelatine powder used. Kwon and Subhash [7] used engineering gelatine powder with a known Bloom strength of 250, while [8] uses gelatine powder for food preparation. Gelatine powder used for food preparation has lower Bloom strength and expected to have a value of around 60–80. The Bloom level is a measurement of toughness, therefore, higher Bloom value gelatine are more resistive to tearing. Glycerol and sorbitol have been added to gelatine mixtures, where glycerol acts as a plasticizer which increases the molecular weight [9]. Different ratios of glycerol and sorbitol were mixed together with gelatine and it was found that an increase in the proportion of glycerol caused an increase in flexibility but the material suffers an overall loss in strength.

In our initial experiments, a mixture only consisting of gelatine powder and water was used. 20 g of gelatine powder was mixed with 200 ml water for 1:10 ratio and refrigerated (5 °C) overnight. Leaving the mixture overnight allows proper blooming of the gelatine and also means the gelatine crystals have enough time to absorb liquid. The blooming process is very important as it ensures smooth texture of the finished product. After leaving it overnight, the gelatine mixture crystalized and the grains can be seen to have enlarged. The cluster of gelatine grains were then heated to about 60–70 °C, taking care not to let the mixture boil as this introduces bubbles. Once the mixture was fully liquefied, it was poured into the cylindrical mould and cooled to room temperature. The cooled mixture is then refrigerated overnight again before testing.

A similar procedure was used with different ratios of gelatine to water, and with additives of glycerin and/or sorbitol as indicated in Table 6.1. An attempt was made using a systematic process to fabricate usable specimens at the highest concentration possible, but which would still solidify. Only one composition of gelatine powder, glycerin and sorbitol (4:10:10) was successful because the nature of the substances made it difficult for the gelatine powder to absorb. Hence, the blooming period was extended to 3 days for the mixtures with additives, to allow the gelatine to crystalize fully.

The konjac gel is derived from the konjac plant and is commonly known in Asia as "Konnyaku". It was considered that fibrous microstructure of the konjac may provide superior toughness over gelatine. To fabricate, 10 g of konjac powder was progressively mixed with 800 ml of cold water while stirring gently to ensure even mixing. The mixture was then heated to 70 °C, stirring the mixture until all the granules dissolved. Precautions were taken not to overheat the mixture. The mixture was poured into the mould and cooled to room temperature before setting in the refrigerator overnight. Higher concentrations of the mixture were attempted but it was found that the mixture tended to become too thick and solidified too quickly causing residual stresses.

Agar is derived from algae and is used as a culinary thickening agent, a growth medium for bacteria in science labs and a dental impression material. It was supplied in a solid gel form, so was heated gently until liquid then was poured into the mould and cooled to room temperature before leaving to re-set in the refrigerator overnight.

Table 6.1 Composition, photoelastic fringe constant and Young's modulus of the gelatine specimens

Specimens	Composition	Fringe constant, f (N/m. fringe)	Young's modulus, E (kPa)
Gelatine:Water	1:10	36	27.3
	2:10	33	56.9
	3:10	28	84.1
Gelatine:Water:Glycerin	2:10:10	82	47.5
	3:10:10	85	75.5
	3:5:10	115	112.5
Gelatine:Glycerin:Sorbitol	4:10:10	152	120.6

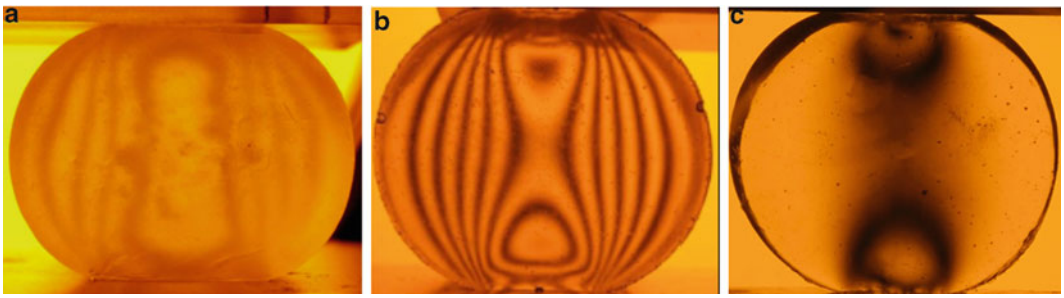

Fig. 6.1 Birefringence of (**a**) konjac gel, (**b**) gelatine and (**c**) agar

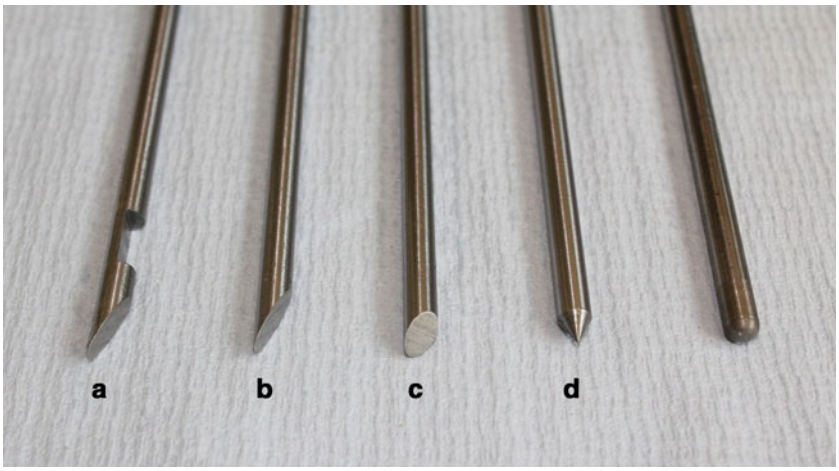

Fig. 6.2 Scale models of the types of needle tip: (**a**) Westcott, (**b**) Chiba (25° bevel), (**c**) Turner (45° bevel) and (**d**) 60° Cone

6.3.1 Transparency and Birefringence

Disc specimens of all the materials were loaded in compression in a circular polariscope. Silicon rubbers were discounted immediately as they exhibited poor photoelastic response. Figure 6.1 shows the birefringent response of the gelatine, konjac and agar. All materials were birefringent but the gelatine displayed the greatest sensitivity. The konjac possessed poor optical properties as the fibrous material tended to refract the light. The gelatine possessed the best optical and birefringent properties and therefore a standard disc in diametral compression calibration test [15] was performed to determine the photoelastic fringe constant, f, for the different mixtures of gelatine. The results are presented in Table 6.1 and show that the highest fringe constant was achieved by the mixture containing both glycerin and sorbitol.

6.3.2 Resistance to Tearing When Punctured

Syringes or needles come in many sizes and shapes. The size, or thickness, is marked with "gauge number". The smaller the gauge value, the thicker the needle. For example for breast lesion localization, a needle of gauge 20 (nominal outer diameter of 0.9 mm) is normally used, which is considered as a fine-needle biopsy while a core-needle biopsy means using a thicker and longer hollow needle to extract tissue samples. The "needles" used in our experiments were scaled up models made from 5 mm diameter steel rod. The different tip shapes of the needles are displayed in Fig. 6.2: Westcott et al. [3, 16]; and as a comparison, a symmetrically tipped cone "needle" was also manufactured.

Figure 6.3 shows the 45° bevel needle inserted into each material and shows that the fibrous nature of the konjac does give it greater resistance to tearing than the gelatine or the agar. The konjac clings to the needle as it is inserted (Fig. 6.3a), but the surface of the gelatine and agar splits, forming a tear (Fig. 6.3b, c). Since the agar performed no better than the gelatine under the tearing test, it was discounted, since the gelatine was a more established surrogate material.

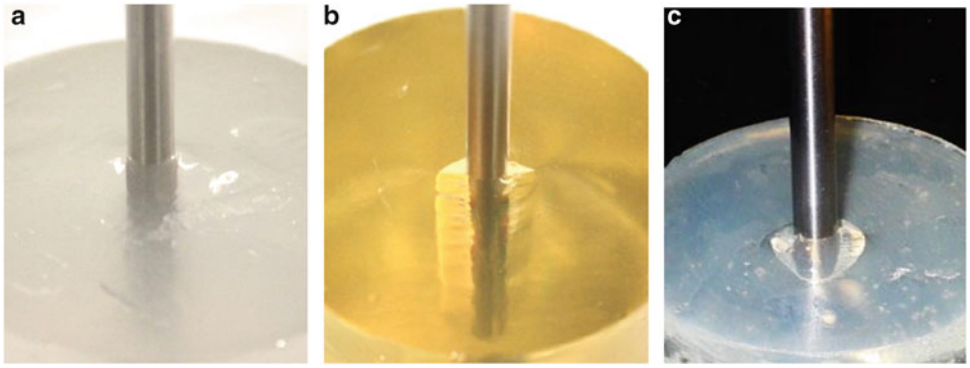

Fig. 6.3 Demonstrating that (**a**) konjac gel has a greater resistance to tearing than (**b**) gelatine or (**c**) agar

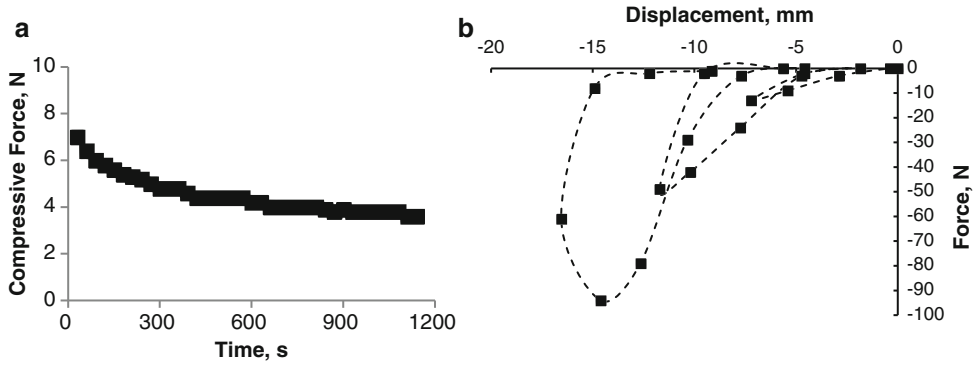

Fig. 6.4 (**a**) Load response of Konjac specimen with 10 mm displacement over 20 min. (**b**) Force-displacement of konjac when loaded and unloaded three times

6.3.3 Performance Under Load

A cylinder sample of each gelatine material was loaded in compression in a Tinius Olsen 5 kN single column H5kS benchtop test machine with a step increment of 1 mm, starting from 0 to 10 mm and its corresponding reaction force recorded. The tests were repeated three times for each specimen and the values averaged out before plotting the stress strain curves and determining the Young's modulus (Table 6.1) from the slope of the graph. Due to the barrelling effect, the stress was calculated from the load using an average area, with consideration of constant volume [17]. The effect of barrelling is difficult to overcome and the only solution was to perform multiple tests to obtain the average value.

A similar procedure was attempted with the konjac specimen, but the material proved to be very non-linear and showed signs of creep (Fig. 6.4a) and viscoelasticity (Fig. 6.4b).

6.3.4 Discussion of Surrogate Material Experiments

At this stage in the research the gelatine was considered to be the most suitable selection for photoelasticity tests on the different shaped needles, because, of the materials tested, it had the best transparency and birefringent sensitivity, and the modulus can be varied with the use of additives in order to represent the varying stiffness of the human body. The photoelastic calibration shows that the concentration of gelatine and additives directly affect the fringe constant. While the specimen with added sorbitol produced the highest fringe constant, this was not a significant increase compared to mixture with glycerine only. As a result, the range of gelatine with glycerin as an additive was selected for this research. The lower stiffness specimen (2:10:10) could represent soft tissues such as the stomach or lung, and the stiffer gelatine (3:5:10) could simulate the heart or liver [12]. However, the 3:10:10 gelatine would be most appropriate to replicate aged human

skin. Additionally, the 3:10:10 gelatine exhibits repeatability in mechanical and photoelastic properties with an acceptable toughness.

The konjac showed excellent resistance to tearing when compared to the gelatine and agar (Fig. 6.3), but the transparency was poorer. The fact that the material shows a non-linear viscoelastic response is not being seen as a drawback since tissue also displays such properties and thus the properties are being explored further.

6.4 Puncture Experiments

During needle insertion, the reaction force on the needle is the sum of contributions from tissue rupture ahead of the tip, tissue deformation in the vicinity, and friction between the tissue and needle. Furthermore, any change in geometry along the needle will also cause changes in needle-tissue response. For example, the work required to puncture the skin will be much higher than the work required to cut the tissue due to the high stress concentration on the crack tip. Therefore, the insertion of the needle cannot be considered as a single motion. The needle insertion process could be separated into three phases, which is the deflection on skin before puncture, insertion of the needle tip and insertion of the tip and shaft as shown in Fig. 6.5 [18].

6.4.1 Phase I: Boundary Displacement

The first phase begins as soon as the needle comes into contact with the tissue and ends when the first crack is initiated. During this phase, the insertion force comprises the force to overcome tissue elasticity and friction, and the force to initiate the first crack (puncturing of the tissue boundary) [4]. Due to the tissue's elasticity, the needle does not puncture the tissue upon contact but the boundary moves with the needle. The small area where the needle pushes the boundary is called the interfacial area. The small interfacial area creates high stress levels with minimal force, and as the stress exceeds the tissue puncture toughness, a crack will be initiated.

6.4.2 Phase II: Tip Insertion

The second phase begins from the first crack initiated to the position where the whole needle tip is in the tissue and the tissue boundary touches the shaft. A rupture often occurs in a split second because the large among of strain energy stored during the boundary displacement phase is released at once to extend the crack. As a result, a large drop in force is noticed and

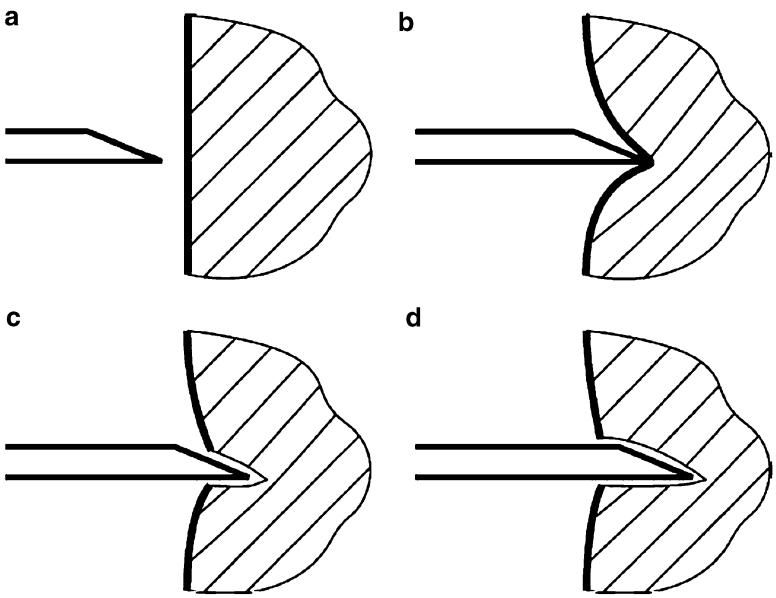

Fig. 6.5 Phases of needle insertion: (**a**) before contact; (**b**) boundary displacement; (**c**) tip insertion; (**d**) tip and shaft insertion [18]

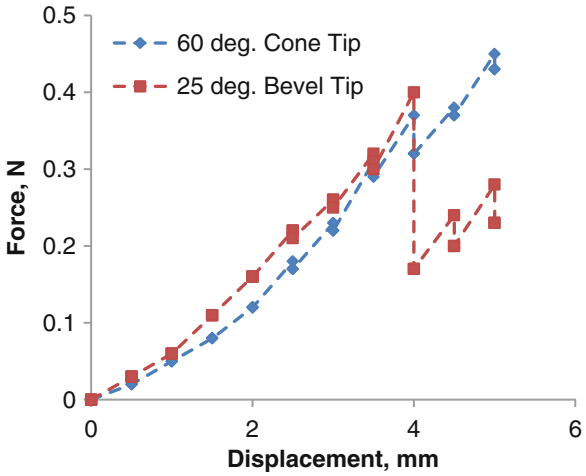

Fig. 6.6 Force-displacement response of two needle tips in the 3:10:10 gelatine specimen

the cutting forces can be seen to be relatively lower than the initial puncture force due to the presence of the crack. However, additional puncture events may occur as the needle pierces further into the tissue, due to tissue inhomogeneity. Additionally, the insertion force also includes the effort to push the crack apart caused by the gradual increase of area of the bevel needle tip. Hence, the increase in force is nonlinear at this stage.

6.4.3 Phase III: Tip and Shaft Insertion

Finally, the third phase starts as the tip and shaft travel through the tissue and stops when the tip reaches its target. In this phase the needle tip is still subjected to cutting and/or puncture force but the behaviour is much more consistent as the interfacial area of tip and tissue remain constant [18]. The increasing contact area between the shaft and the tissue causes varying friction force throughout the insertion process. Although most of the stock needles manufactured are lubricated, a certain degree of friction still persists.

6.4.4 Puncture Test Procedure

A new set of gelatine-glycerine-water mixture 3:10:10 cylindrical specimens were prepared for the puncture experiment. The 25° bevel tip needle was attached to the Tinius Olsen machine, placed just touching the gelatine specimen and the load cell and displacement readings were both set to zero. The needle was then displaced and every 0.5 mm its corresponding force recorded. This procedure was repeated with the 60° cone tip scaled needle. The results are shown in Fig. 6.6. The procedure was then repeated within a light field circular polariscope and the images recorded at every 1 mm displacement are shown in Fig. 6.7. Since photoelasticity gives an integral effect, a two dimensional system was created so there were insignificant out of plane effects. To hold the gelatine in space, glass sheets were glued together forming a container which could hold the gelatine at a uniform thickness of 15 mm.

6.4.5 Discussion of Puncture Test

The 25° bevel tip insertion in Fig. 6.6 shows a steady force increase which drops abruptly at 4 mm. The peak force at 4 mm displacement in this case could be described as the puncture event. At this point, the first crack is initiated and the strain energy accumulated was relaxed resulting in a sharp drop in force. So the puncture event signifies the end of phase one and the start of phase two. In phase two, the variation in force is due to the continuous cutting action of the tip as well as to overcome friction and internal stiffness. The 60° cone tip produces a more moderate puncture event.

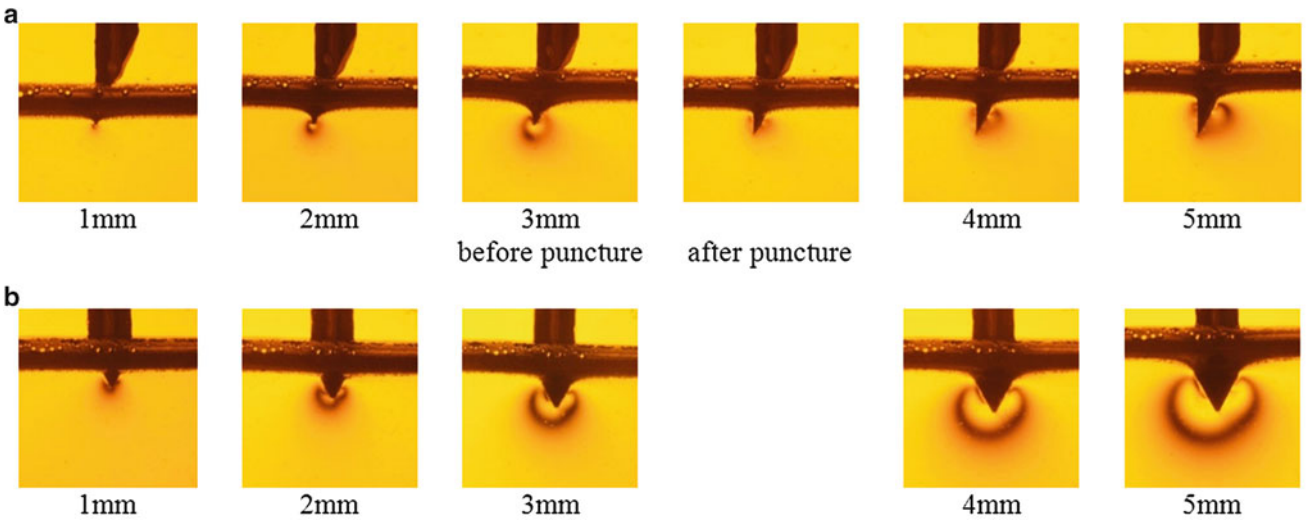

Fig. 6.7 Photoelastic fringes, representing the shear stress in the 3:10:10 gelatine; showing the (**a**) 25° bevel tip and (**b**) 60° cone tip with increasing insertion into the material

In Fig. 6.7 the half order photoelastic fringes represent the shear response around the needle tips. It can be seen that the fringe concentration, and hence stress, increase with insertion depth. However for the 25° bevel tip needle, the puncture event is seen in the reduction in fringes after 3 mm displacement. Other than the relaxation in stress, the fringe pattern also changed after the puncture event. Before the puncture, the fringe could be seen to surround the tip uniformly, but after the material had failed, the accumulated stresses at the tip were relieved. The figure highlights the difference between symmetrically shaped tips and the bevelled tip needles. Besides showing an increase in shearing force as the needle is inserted, it confirms the hypothesis of an asymmetric force distribution on bevel tipped needles.

6.5 Closing Remarks

This work is still in preliminary stages and further research is needed to develop a robust full-field experimental method for validating computational models of needle insertion. Although the gelatine mixed with glyerin was used for the photoelastic tests, and showed good optical properties and controllable stiffness, its tearing characteristics are quite different from those of biological tissues. However, the konjac demonstrates potential as a tissue surrogate which doesn't tear, and experiments are underway to quantify its non-linear viscoelastic behaviour for comparison with the non-linear properties of tissue. It is also acknowledged that the development of an isotropic surrogate material is unrealistic in the human body, but is a starting point to a much wider research programme.

The current study only considered phase one of needle insertion and the second and third phases are to be considered in the future. Another factor not discussed in this work is how the magnitude of insertion force or its rate influences the magnitude of needle deflection. Besides the cutting force, the shearing caused by friction between the needle shaft and the tissue is also damaging to the material. Since photoelasticity provides a map of shear strain, the technique appears ideal for investigation of friction and results to be presented at the conference show some interesting behaviour.

References

1. Misra S, Reed KB, Schafer BW, Ramesh KT, Okamura AM (2010) Mechanics of flexible needles robotically steered through soft tissue. Int J Robot Res 29:1640–1660
2. Jahya A, van der Heijden F, Misra S (2012) Observations of three-dimensional needle deflection during insertion into soft tissue. In: International conference on biomedical robotics and biomechatronics, Italy, June 2012, pp 1205–1210
3. Abolhassani N, Patel R, Moallem M (2007) Needle insertion into soft tissue: a survey. Med Eng Phys 29:413–431
4. Misra S, Reed KB, Douglas AS, Ramesh KT, Okamura, AM (2008) Needle-tissue interaction forces for bevel-tip steerable needles. National Institutes of Health, NIH Public Access, Scottsdale, pp 224–231

5. Abayazid M, op den Buijs J, de Kortey CL, Misra S (2012) Effect of skin thickness on target motion during needle insertion into soft-tissue phantoms. In: The fourth IEEE RAS/EMBS international conference on biomedical robotics and biomechatronics, pp 755–760
6. Cronin DS, Falzon C (2010) Characterization of 10 % ballistic gelatin to evaluate temperature, aging and strain rate effects. Exp Mech 51:1197–1206
7. Kwon J, Subhash G (2010) Compressive strain rate sensitivity of ballistic gelatin. J Biomech 43(3):420–425
8. Markidou A, Shih WY, Shih W (2005) Soft-materials elastic and shear moduli measurement using piezoelectric cantilevers. Am Inst Phys Rev Sci Instrum 76(3):064302
9. Thomazine M, Carvalho RA, Sobral PJA (2005) Physical properties of gelatine films plasticized by blends of glycerol and sorbitol. J Food Sci 70(3):E172–E176
10. Agache PG, Monneur C, Leveque JL, De Rigal J (1980) Mechanical properties and Young's modulus of human skin in vivo. Arch Dermatol Res 269:221–232
11. Edwards C, Marks R (1995) Evaluation of biomechanical properties of human skin. Clin Dermatol 13(4):375–380
12. Saraf H, Ramesh KT, Lennon AM, Merkle AC, Roberts JC (2007) Mechanical properties of soft human tissues under dynamic loading. J Biomech 40(9):1960–1967
13. Davis SP, Landis BJ, Adams ZH, Allen MG, Prausnitz MR (2004) Insertion of microneedles into skin. J Biomech 37:1155–1163
14. Taylor D, O'Mara N, Ryan E, Takaza M, Simms C (2011) The fracture toughness of soft tissues. J Mech Behav Biomed Mater 6:139–147
15. Cloud G (1995) Optical methods of engineering analysis. Cambridge University Press, Cambridge
16. Lacasse Y, Wong E, Guyatt GH, Cook DJ (1999) Transthoracic needle aspiration biopsy for the diagnosis of localised pulmonary lesions: a meta-analysis. Thorax 54:884–893
17. Benham PP, Crawford RJ, Armstrong CG (1996) Mechanics of engineering materials. Pearson, Essex, p 497
18. van Gerwen DJ, Dankelman J, van den Dobbelsteen JJ (2012) Needle–tissue interaction forces – a survey of experimental data. Med Eng Phys 34:665–680

Chapter 7
Polymer Gels for Defense Applications

Randy A. Mrozek, Yelena R. Sliozberg, Jan W. Andzelm, and Joseph L. Lenhart

Abstract A polymer gel is a physically or chemically cross-linked polymer that is highly swollen by solvent. The gel properties can be tuned by varying the polymer chemistry, solvent type, polymer-solvent architecture and molecular weight, and solvent loading. In addition, small molecule additives and fillers can be incorporated into the gel formulation to enhance the properties further. This tunability offers the potential for gel implementation in an array of Army related technologies ranging from combat casualty care and tissue surrogates, to robotics and electronics devices. Several obstacles hinder widespread deployment of gel-based technologies including: (1) limited operational temperature windows and material lifetimes; (2) poor toughness and durability; (3) unstable performance in extreme mechanical, electrical, chemical, and radiation environments; and (4) limited multi-functional capability. We anticipate that a fundamental understanding of how to tailor the gel properties will have a broad impact on various technologies including robotics, smart clothing, armor, tissue simulants, sensors, energy storage, battlefield medicine, etc.

Keywords Gel • Non-aqueous • Non-entangled • Loop formation • Functional group spacing

7.1 Introduction

Glassy epoxy resins are utilized extensively in both military and commercial applications, due in part to the ability to tailor the properties by changing the backbone chemistry, cross-link density, and the incorporation of particulate fillers and small molecule additives. Some applications require a soft, flexible, and highly conformable cured epoxy. This can be accomplished by exploiting low functionality and flexible monomers, off-stoichiometric formulations, or the addition of a low volatility plasticizing solvent. The latter swells the crosslinked epoxy network producing a polymer gel wherein the solvent allows for a deformable material while the cross-linked network provides the ability to recover after deformation [1]. The incorporation of solvent also provides an additional parameter to alter the mechanical properties of the elastomeric epoxy gel. While substantial research has investigated gelation phenomena in epoxy resins, there has been minimal research on solvent swollen-epoxy gels and that work primarily focused on water-based hydrogels for the development of actuators, sensors, and biomedical devices.

The impact of water content on the mechanical properties of hydrogels has been studied extensively for use in a variety of applications including adhesives, biomedical technology, and actuators. However, hydrogels are only useful in a limited operational temperature range and operational temperature time dependent on packaging and ambient humidity. Several applications including active coatings, energy storage devices, electronic encapsulants, and sensors require operation outside the accessible temperature range of hydrogels. For example, high boiling point solvents up to 180 °C are often required in gel electrolytes to avoid degradation of gel properties and performance [2]. In addition, hydrogel electrolytes have been shown to produce oxygen and hydrogen gas near an electrode surface [3]. As a result, emphasis has been placed on developing non-aqueous gels with a broad operational temperature range.

In this investigation, epoxy-based gels are used to determine the impact of precursor size on the thermal and mechanical properties of solvent-swollen gels. The networks consisted of difunctional epoxy precursors separated with a poly(propylene

R.A. Mrozek (✉) • Y.R. Sliozberg • J.W. Andzelm • J.L. Lenhart
U.S. Army Research Laboratory, 4600 Deer Creek Loop, APG, Adelphi, MD 21005, USA
e-mail: randy.a.mrozek.civ@mail.mil

F. Barthelat et al. (eds.), *Mechanics of Biological Systems and Materials, Volume 7: Proceedings of the 2014 Annual Conference on Experimental and Applied Mechanics*, Conference Proceedings of the Society for Experimental Mechanics Series,
DOI 10.1007/978-3-319-06974-6_7,

glycol) (PPG) spacer cross-linked with a tetrafunctional amine precursor composed of two primary amines separated by a PPG spacer. The precursor size was controlled by varying the PPG spacer length, where even the largest precursor has a molecular weight lower than the molecular weight of entanglement for PPG, ~7,000 g mol^{-1}. As a result, the likelihood of entanglements is decreased and loop defects will likely have a significant impact on the network structure.

7.2 Experimental

The poly(propylene glycol) bis(2-aminopropyl ether)s were used as-received from Huntsman Corporation (Salt Lake City, UT). The poly(propylene glycol) diglycidyl ethers (PPGDE), nonyl phenol, and dibutyl phthalate were used as received from Aldrich Chemical (Milwaukee, WI). Epoxy networks were formed by cross-linking a difunctional epoxide monomer, polypropylene glycol diglycidyl ether(PPGDE), and a tetrafunctional amine monomer, poly(propylene glycol) bis(2-aminopropyl ether), with two primary amines separated by a polypropylene glycol spacer in the presence of 0–60 wt% dibutyl pthalate. Nonyl-phenol was utilized as a catalyst for the cross-linking reaction and was added at 5 mass% relative to the total mass in the formulation. The mixture was then cured for 6 days at 90 °C. The extent of cure was monitored by rheological measurements that determined after 6 days at 90 °C the value of the modulus in the plateau region remained unchanged indicating complete cure. Rheological measurements were performed on rectangular gel samples (12 × 4.5 × 28 mm) in a torsional geometry. The measurements were made on a Rheometric Scientific ARES instrument at a frequency of 1 Hz and a scan rate of 2 °C min^{-1}. An environmentally controlled oven was used to determine the modulus in a temperature range of −100 to 70 °C. Strain sweeps were conducted at various temperatures to ensure that the modulus was independent of strain at a frequency of 1 Hz. The relative uncertainty in the modulus values is less than ~10 %, as was demonstrated by measurements on multiple gel samples at a particular solvent loading. The extent of cure was monitored used Near Infrared Spectroscopy. Sample were produced by curing gel samples in between two microscope slides separated by a 1 mm spacer. Measurements were made in a transmission geometry in a range of 4,000–8,000 cm^{-1} using a ThermoNicolet Nexus 870 Fourier Transform Infrared Spectrometer. The samples were cured in the oven at 90 °C in between measurements.

7.3 Results and Discussion

Polymer gels were produced by cross-linking a difunctional epoxide monomer, polypropylene glycol diglycidyl ether (PPGDE), and a tetrafunctional amine monomer, poly (propylene glycol) bis(2-aminopropyl ether), with two primary amines separated by a polypropylene glycol spacer (Fig. 7.1). Monomer length was controlled by varying the polypropylene glycol molecular weight between functional groups. Amine monomer molecular weights of 230, 400, 2,000, and 4,000 g mol^{-1} were investigated and are referred to as D230, D400, D2000, and D4000, respectively. The amine functionalized precursor was cross-linked by an epoxy monomer with a molecular weight of either 640 g mol^{-1}

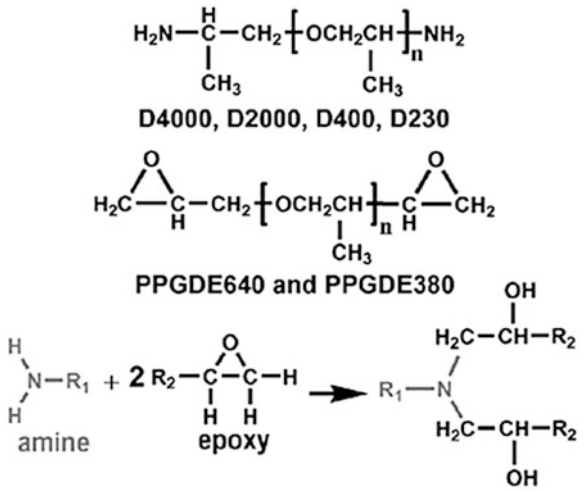

Fig. 7.1 Structures of the precursors utilized in the gels

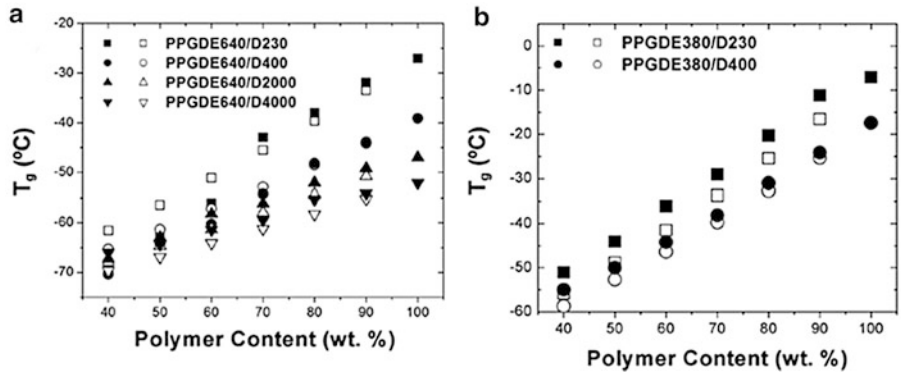

Fig. 7.2 Experimental (*filled symbols*) and theoretical calculated using the Fox equation (*open symbols*) for T_g as a function of polymer content for gels consisting of (**a**) PPGDE640 and (**b**) PPGDE380 cured with various molecular weight amine hardeners

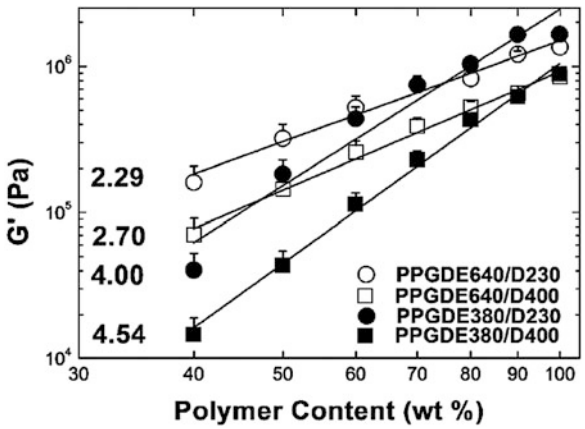

Fig. 7.3 Plot of shear storage modulus for PPGDE640 and PPGDE380 gels cured with D230 and D400, respectively, at various DBP loadings. *Lines* represent a best fit to the data for each amine hardener investigated. The modulus was measured at T_g + 70 °C for each gel

(PPGDE640) or 380 g mol^{-1} (PPGDE380). Epoxy gels were prepared in the presence of 0–60 mass% dibutyl phthalate (DBP) to determine the impact of solvent loading on the mechanical properties of the gel. For every cross-link density investigated, the modulus in the plateau region decreases with increasing solvent loading and the peak in the tan δ curve shifts to lower temperatures, indicating a decrease in the glass transition temperature (T_g—Fig. 7.2) with increased DBP loading consistent with expected behavior.

When the log of the modulus in the plateau region is plotted against the log of the polymer content, the scaling factors become much larger than the theoretical scaling factor of 2.3 in entanglement dominated systems. We attribute this to the differences in bulk and local concentrations of reactive functionality as the solvent loading is increased. As the solvent loading increases, the bulk concentration of reactive epoxy and amine hydrogen atoms from neighboring polymer chains is decreasing due to solvent dilution. However, the local concentration of the unreacted secondary amine and the remaining epoxy functionality of the diepoxide are unchanged. This coupled effect leads to an increase in the probability of loop formation, and a decrease in the probability of forming an elastically active bridge to another polymer chain, as the solvent loading increases. Similarly, as the diamine molecular weight increases, the probability of loop formation also increases due to the decrease in the bulk concentration of reactive amine species. These two factors, together, explain the increase in scaling factor with diamine molecular weight in Fig. 7.3, which we attribute to increased formation of loop defects.

It is also possible to explain the increase in scaling factors due to a decreased extent of reaction due to the presence of solvent. A reduced extent of reaction would produce dangling chain ends that would have a similar impact on the modulus as loop defects. However, several observations make a reduced extent of reaction an unlikely cause for the increased scaling factor. The modulus of the gels was measured as a function of time and it did not change after 6 days at 90 °C and remained constant over extended storage times suggesting complete epoxy-amine reaction. As a more direct measurement to quantify the extent of reaction, D230/PPGDE640 and D4000/PPGDE, both neat and with 60 % DBP, respectively, was monitored by FTIR using the disappearance of the epoxy stretching and bending peak at 4,530 cm^{-1} that has been previously utilized in similar epoxy resin cure studies [4, 5]. The peak at 4,530 cm^{-1} was reduced to baseline values within 6 days indicating complete cure within the resolution of FTIR spectroscopy (Fig. 7.4). Even using a conservative estimate of 90 % cure,

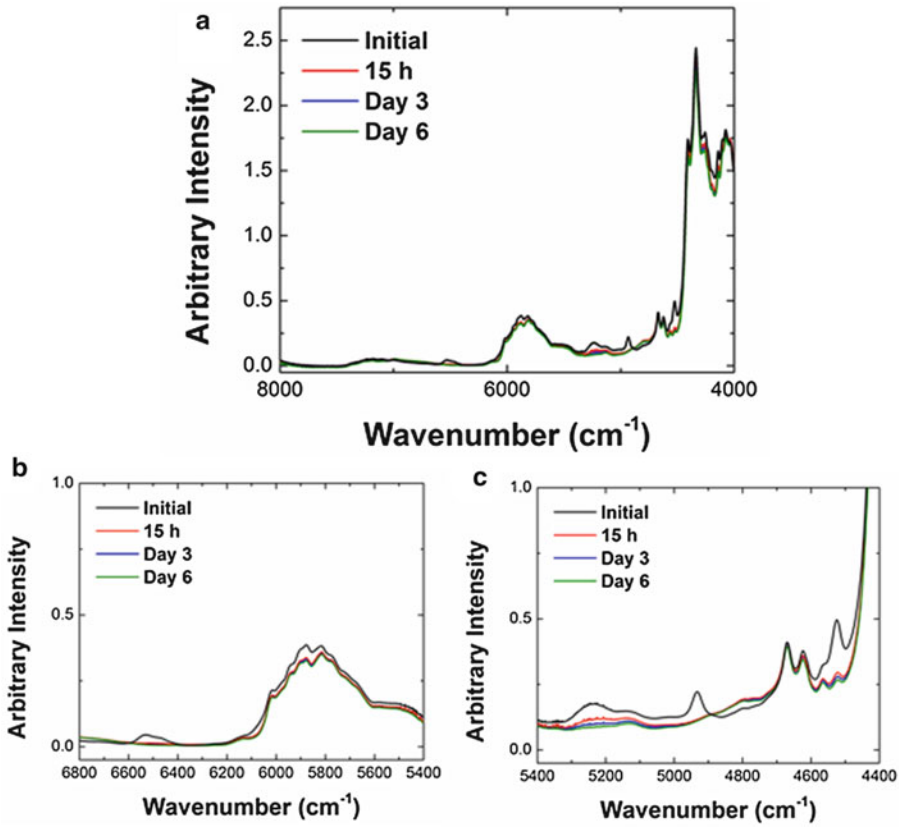

Fig. 7.4 Near IR spectra of a D230/PPGDE640 epoxy containing 60 % prior to curing and after 15 h, 3 days, and 6 days of cure at 90 °C in a range of (**a**) 4,000–8,000 cm^{-1} and expanded regions of (**b**) 5,400–6,800 cm^{-1} and (**c**) 4,400–5,400 cm^{-1}, respectively

to account for any small fraction of unreacted functional groups not detectable with FTIR, the modulus would be within 25 % of its fully cured value for model end-linked systems [6] which does not lead to a significant impact on the modulus. In addition, the trends with molecular weight would remain the same. Therefore, we conclude that the loop defects, and not dangling chain ends are responsible for the increased scaling factor.

7.4 Conclusions

We were able to obtain nearly three orders of magnitude change in shear storage modulus without altering the backbone chemistry by varying the solvent content and precursor chain length. This provides the ability to tailor the mechanical properties over a wide range while minimizing the impact on environmental stability, device compatibility, and processability. Utilizing network precursors below the entanglement molecular weight, scaling factor values much larger (up to 4.54) than the theoretical value of 2.3, for entanglement dominated network formation in a theta solvent, were obtained. The enhanced scaling factors were attributed to increased formation of loop defects. From this study three important trends were observed: (1) Loop formation increases with decreasing polymer content (i.e. increased dilution). This effect is attributed to the fact that the local functional group concentration, responsible for loop formation, remains constant while the bulk functional group concentration is being reduced. (2) Loop formation decreases with increasing molecular weight of the difunctional epoxide (PPGDE), consistent with previous work attributed to an increased capture radius. (3) Loop formation increases with increasing diamine precursor molecular weight (a tetrafunctional monomer due to the reactive capability of each amine hydrogen) attributed to the molecular structure which consists of two difunctional groups separated by a non-reactive spacer. When the molecular weight of the spacer is increased the local concentration of each difunctional group remains consistent while the bulk functional density is decreased, similar to dilution. As a result, it is critical to take into consideration the formation of loop defects and the impact of polymer content, diepoxy molecular weight, diamine molecular weight, and spacing of the reactive sites on the polymer chain on the loop defect concentration when tailoring these epoxy–amine polymer gels for specific applications.

Acknowledgements Certain commercial equipment and materials are identified in this paper in order to specify adequately the experimental procedure. In no case does such identification imply recommendations by the Army Research Laboratory nor does it imply that the material or equipment identified is necessarily the best available for this purpose.

References

1. Flory PJ (1953) Principles of polymer chemistry, vol 1. Cornell University, Ithaca, NY, p 576
2. Song JY, Wang YY, Wan CC (1999) J Power Sour 77:183–197
3. Gong JP, Kawakami I, Sergeyev VG, Osada Y (1991) Macromolecules 24:5246–5250
4. Mijovic J, Andjelic S (1995) Macromolecules 28:2787–2796
5. Raman VI, Palmese GR (2005) Macromolecules 38:6923–6930
6. Gottlieb M, Macosko CW, Benjamin GS, Meyers KO, Merrill EW (1981) Macromolecules 14:1039–1046

Chapter 8
Development of a Microloading Platform for In Vitro Mechanotransduction Studies

S.L. York, J.D. King, A.S. Pietros, B. Zhang Newby, P. Sethu, and M.M. Saunders

Abstract Mechanotransduction studies aim to understand the process of cells converting mechanical stimuli into a cellular response. As it can be difficult to study the impact of isolated factors using in vivo studies, in vitro studies are used as they offer more precisely controlled loads for experiments and allow cell culture on a variety of surfaces. Here, we developed a microloading platform for in vitro mechanotransduction studies, stretching the substrate by tenting it with a centrally contacting platen. This platform works through the use of a load cell and microactuator, which was characterized by comparing the reported and measured displacements. In addition, an alignment block was designed for the microloading platform to increase reproducibility between studies, and a cell culture handling system was designed to hold samples before experimentation and reduce preloads, allowing the study of only the controlled loading. A polydimethylsiloxane (PDMS) scaffold was also designed for cell loading, complete with a positional reference grid for observing the response of individual cells to strain. Initial work with this microloading platform includes studying osteocyte-like MLO-Y4 cells and changes in viability in response to mechanical load in vitro. These initial studies have demonstrated the ability to induce cell death in response to microdamage.

Keywords Mechanotransduction • Microloading platform • Polydimethylsiloxane • Cellular death • Osteocyte

8.1 Introduction

Mechanotransduction models are used in laboratories to investigate cellular responses to loads. A wide range of methods for stimulating cells in vitro exist and can simulate different types of loads. Examples include parallel plate flow chambers and the use of a platen to stretch a material with cells. Parallel plate flow chambers consist of cells seeded on a glass slide and inserted into a chamber. As fluid flows through the chamber, it flows past the cells and induces a fluid shear stress. Alternatively, platens can be used to stretch materials that have been seeded with cells. This induces a direct strain on the material and thus the cells, but requires a cell substrate that can be stretched [1]. The type of load applied in mechanotransduction experiments is significant in that physiologically relevant loads are desired whenever possible. Mechanotransduction studies are relevant in a range of fields, including cardiac and bone research. Bone mechanotransduction studies aim to understand the change in behavior of bone cells and subsequent bone to changes in mechanical load.

S.L. York (✉) • J.D. King • A.S. Pietros • M.M. Saunders
Department of Biomedical Engineering, The University of Akron, Auburn Science and Engineering Center 275, West Tower, Akron, OH 44325, USA
e-mail: sly15@zips.uakron.edu

B.Z. Newby
Department of Chemical and Biomolecular Engineering, The University of Akron, Whitby Hall 101A, Akron, OH 44325, USA

P. Sethu
Division of Cardiovascular Disease, The University of Alabama at Birmingham, McCallum Basic Health Sciences Building 290 A, 1918, Birmingham, AL 35294, USA

F. Barthelat et al. (eds.), *Mechanics of Biological Systems and Materials, Volume 7: Proceedings of the 2014 Annual Conference on Experimental and Applied Mechanics*, Conference Proceedings of the Society for Experimental Mechanics Series,
DOI 10.1007/978-3-319-06974-6_8,

Wolff's law is a theory that bone responds to changes in mechanical environment. Well known examples include the tennis player with stronger and denser bone in their dominant arm, and astronauts who lose bone density while in space [2, 3]. This is thought to be impacted by bone remodeling, a process in which old bone is resorbed and new bone is laid down, thus maintaining bone size and density. In this process, osteoclasts function as a bone resorbing cell, working to enzymatically break down old bone matrix. This free surface provides an area for osteoblasts to lay down collagen and new bone matrix. As part of laying down new bone, some osteoblasts become entrapped in the bone matrix, and become osteocytes. These cells reside in lenticular cavities found in bone, and narrow channels called canaliculi connect the lenticular cavities. Dendritic processes, or gap junctions, extend between osteocytes using the canaliculi. These gap junctions allow communicating between nearby cells by sending small molecules back and forth. As osteocytes reside in the bone matrix, they are exposed to interstitial fluid running through the lenticular cavities. They may also be strained as the bone matrix is placed under mechanical loads. This strain may be amplified by the lenticular cavities wherein osteocytes reside [4]. This suggests that osteocytes may play an important role in the mechanotransduction process in bone, providing a mechanism to detect changes in the mechanical environment.

It has been proposed that localized damage to bone matrix impacts the osteocytes, and that these cells initiate and control the bone remodeling process. Current theory is that osteocytes detect changes in the mechanical load, as interstitial fluid flows past or as the microstrain placed on bone are amplified [5, 6]. This change in the mechanical environment may be communicated to nearby osteocytes through the use of gap junction intercellular communication [7]. To investigate this theory, osteocytes must first be loaded in vitro. This study developed a microloading platform using a platen to load osteocyte-like MLO-Y4 cells, which allows for the quantification of changes in cellular activity as a function of loading.

A microloading platform for loading MLO-Y4 cells in vitro was developed and characterized. Following the building of the platform, the actuator for loading was characterized, insuring an accurate and repeatable displacement. For cell culture and loading, a polydimethylsiloxane (PDMS) well was designed and fabricated. PDMS was chosen due to its optical clarity, ease of fabrication, and the use of micron scale features. For this experiment, a positional reference grid was designed on the PDMS well, allowing comparisons of tracked cells before and after loading. Finite element analysis models were used to characterize the PDMS well, insuring the PDMS would not fail during experimentation. An alignment block and a cell culture holding system were also developed to insure consistent positioning of the PDMS well for loading and to reduce preloading of the PDMS wells, respectively. Following the development of the PDMS well and the microloading platform, changes in cellular behavior were observed. This was accomplished with a lactate dehydrogenase assay used to detect cell viability. This study serves as an important first step in investigating the role of osteocytes in bone mechanotransduction.

8.2 Methods and Results

8.2.1 Development and Characterization of Microloading Platform

The microloading platform, Fig. 8.1, consisted of an aluminum base plate (125 mm × 125 mm × 10 mm) connected to a Plexiglass top plate (125 mm × 125 mm × 10 mm) with four corner rods (250 mm × 5 mm radius). The Plexiglass top plate had a square hole in the center (12.5 mm × 12.5 mm) for platen clearance. A smaller aluminum base plate (75 mm × 75 mm × 10 mm) hung below the Plexiglass top plate with four corner rods (50 mm × 5 mm radius). This smaller aluminum base plate was a mounting plate for the microactuator (Zaber Technologies, T-NA08A25). The actuator connected to a 2.45 N load cell (Sensotec), and was used to detect initial contact during loading. For loading, a cylindrical platen was attached to the load cell and used to apply the load using a tenting effect from below.

Once assembled, microactuator performance was characterized through the use of gauge blocks. The microloading platform was assembled with the microactuator fully extended, Fig. 8.2. After aligning the cylindrical platen with a fixed surface, the displacement was decreased using a controller for the microactuator until a gauge block of known thickness could be inserted between the end of the cylindrical platen and the fixed surface. This characterization was completed using gauge blocks with thicknesses of 1,587.5, 2,540, 3,175, and 5,080 μm (0.0625, 0.1, 0.125, and 0.2 in.). Measurements were taken in triplicate and repeated three times. The measured displacement was compared to the theoretical displacement, based on the thickness of the gauge block, Fig. 8.3.

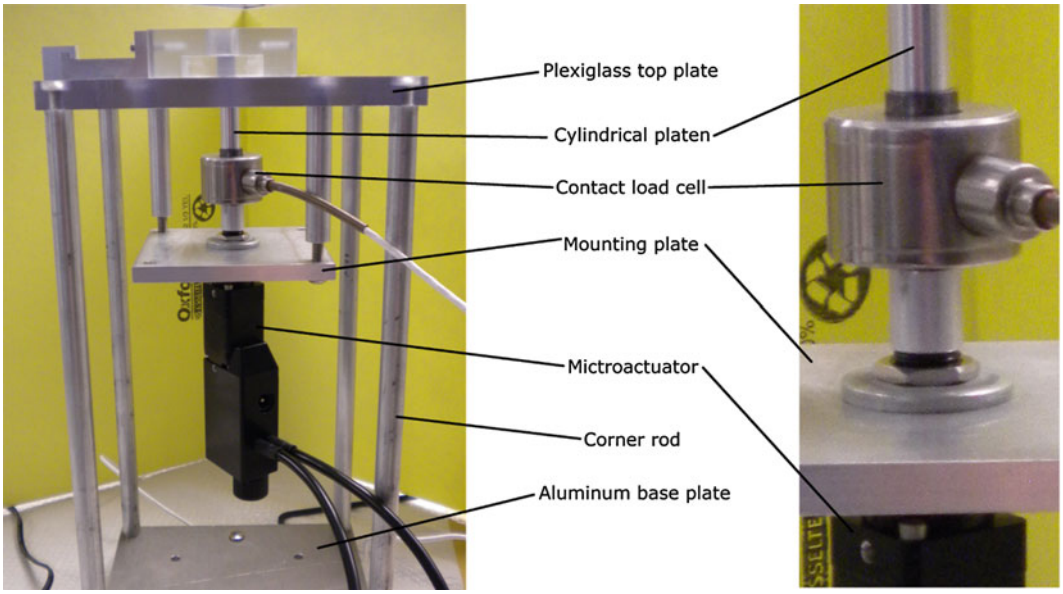

Fig. 8.1 Assembled microloading platform

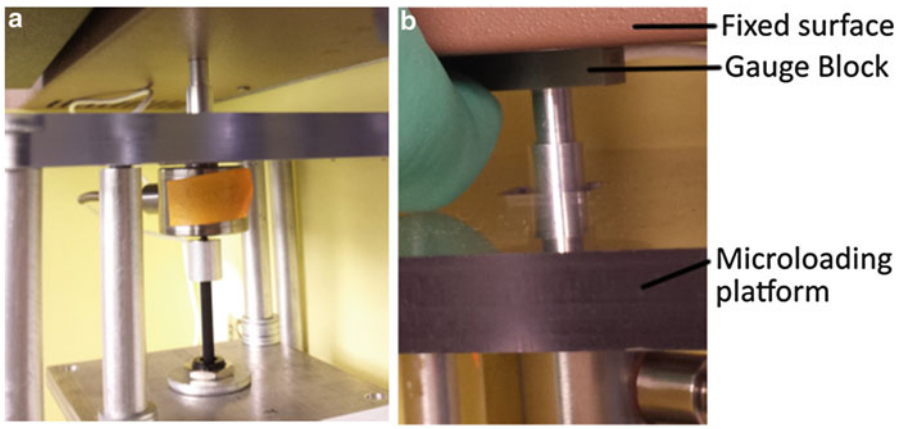

Fig. 8.2 Microloading platform setup for actuator characterization. Set on its side, the microloading platform was aligned with a fixed surface before reducing the displacement, allowing the gauge block to be fit between the platen and fixed surface

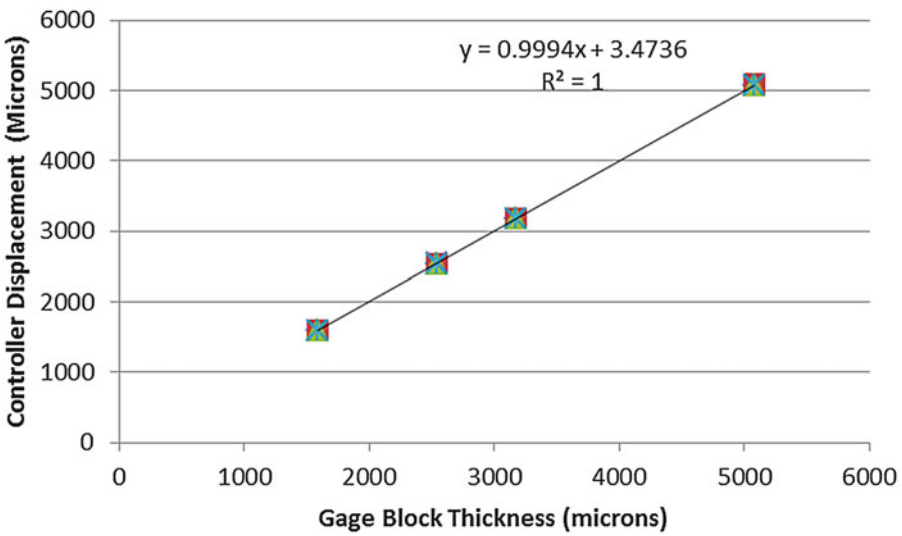

Fig. 8.3 Results from actuator characterization. A slope of 1 corresponds to an exact correlation

8.3 Microloading Platform Alignment

Following the development and characterization of the microloading platform, alignment was addressed. An alignment block was machined for the top of the microloading platform to locate the loading center during testing, Fig. 8.4. In addition, a polycarbonate cell culture holding system was developed to hold the PDMS well structure, and fit into the alignment block, Fig. 8.4. This cell culture holding system aimed to eliminate any preloading of the PDMS well prior to experimentation by preventing the PDMS well from sticking to the tissue culture plate. The polycarbonate was handled prior to experimentation instead of the PDMS well, eliminating preloading of the PDMS well and the seeded cells.

8.4 PDMS Fabrication

Two hundred micron thick PDMS layers were fabricated via a spin casting procedure. Briefly, PDMS (Sylgard 182, Dow Corning, Midland, MI) pre-polymer and cross-linking agent were mixed thoroughly in a 10:1 ratio and degassed in a vacuum desiccator to remove air bubbles. A silicon wafer was mounted on a spin coater (Laurel Technologies, North Wales, PA) and the mixed PDMS mixture was poured carefully onto the center of the wafer without incorporation of air bubbles and spun at speeds of 2,000 rpm for 30 s, generating a 200 μm thick layer. Following spinning, the cross-linking was accomplished by placing the silicon wafer in an 80 °C oven for 3 h. The cross-linked PDMS membranes were cut to the desired shape using a scalpel. The remainder of the PDMS wells was fabricated using a similar procedure, but were not spun to reach a smaller thickness. Core borers were used to remove material from the top and bottom layer of the PDMS structure, generating a well for cell culture and a space for loading. PDMS wells were fabricated by combining the three layers using a PDMS glue technique. For this technique, PDMS pre-polymer and cross-linking agent were mixed thoroughly in a 10:1 ratio before being spread on two clean pieces of PDMS. Following 2 h of baking in a 60 °C oven, the two pieces of PDMS were glued together. After gluing the third piece of PDMS, the well structure was ready for cleaning and experimentation, Fig. 8.5.

8.5 Finite Element Analysis of PDMS Well

A computer model of the PDMS well structure was designed using modeling software (SolidWorks 2012), Fig. 8.5. This computer model was used for finite element analysis (FEA) simulations to insure the PDMS well would not fail during loading. Table 8.1 shows the material properties used for PDMS, using accepted literature values, as well as the number of nodes and elements used for the finite element simulation [8, 9]. The finite element simulations were run using a remote displacement applied to the center of the bottom of the PDMS well structure, and actuator controller displacements of 1, 2, 4, 6, 8, and 12 mm. These FEA studies were run using a nonlinear model to allow a large displacement of the 200 μm thick PDMS grid. For the model, the PDMS well structure was constrained on top and along the sides with fixed geometry, simulating the PDMS well in the cell culture holding system. Results of the FEA study are shown in Table 8.2 and Fig. 8.6.

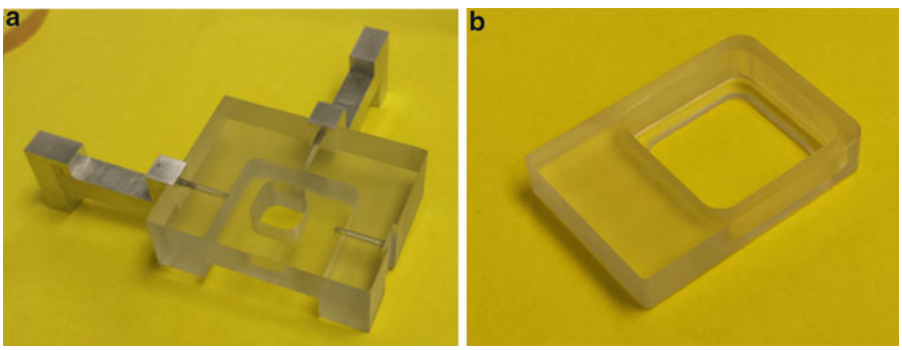

Fig. 8.4 (**a**) Alignment block designed for the Plexiglass top plate. Centering legs, made of aluminum, extend to the edge of the platform and center the sample for loading. (**b**) Cell culture holding system designed to hold PDMS well structure and reduce preloads

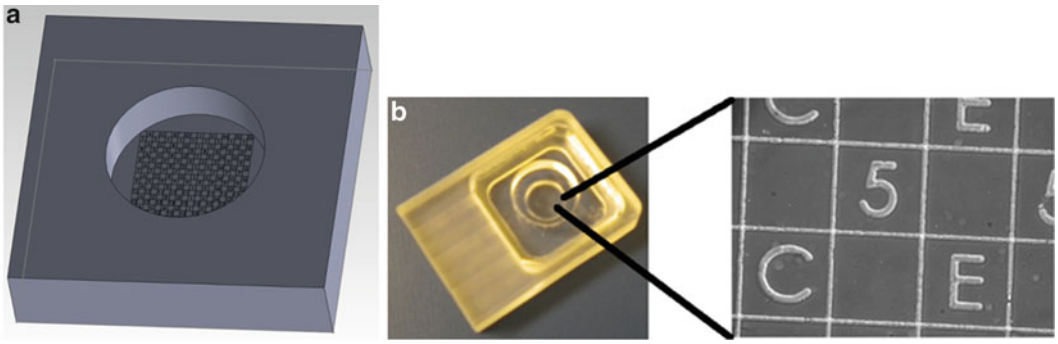

Fig. 8.5 (**a**) SolidWorks model of PDMS well. Here, the top well for cell culture and positional reference grid can be seen. (**b**) PDMS well structure fully assembled. The *top layer* has a 1.27 cm diameter hole for cell culture, the *middle layer* contains the positional reference grid shown on the *right*, and the *bottom layer* has a center hole with a diameter of 0.89 cm allowing for loading from below

Table 8.1 PDMS material properties input in the FEA model

Model type	Linear elastic isotropic	
PDMS material properties		
Elastic modulus	1.6	MPa
Poisson's ratio	0.49	–
Mass density	0.97	Kg/m^3
Tensile strength	10	MPa
FEA properties		
Nodes	60,127	–
Elements	36,999	–

Table 8.2 FEA study results

Actuator controller displacement (mm)	Max stress (vonMises) (MPa)	Max displacement (mm)	Max strain (mm/mm)	Max P1 (MPa)	Min P1 (MPa)	Max P3 (MPa)	Min P3 (MPa)
1	0.11	0.48	0.04	0.13	−0.11	0.03	−0.13
2	0.28	0.96	0.11	0.32	−0.31	0.11	−0.37
4	0.68	1.92	0.26	0.74	−0.82	0.37	−1.15
6	0.87	2.88	0.47	1.10	−1.37	0.61	−1.88
8	1.17	3.85	0.72	1.90	−2.34	0.94	−3.04
12	2.04	5.77	1.23	3.48	−4.23	1.45	−5.27

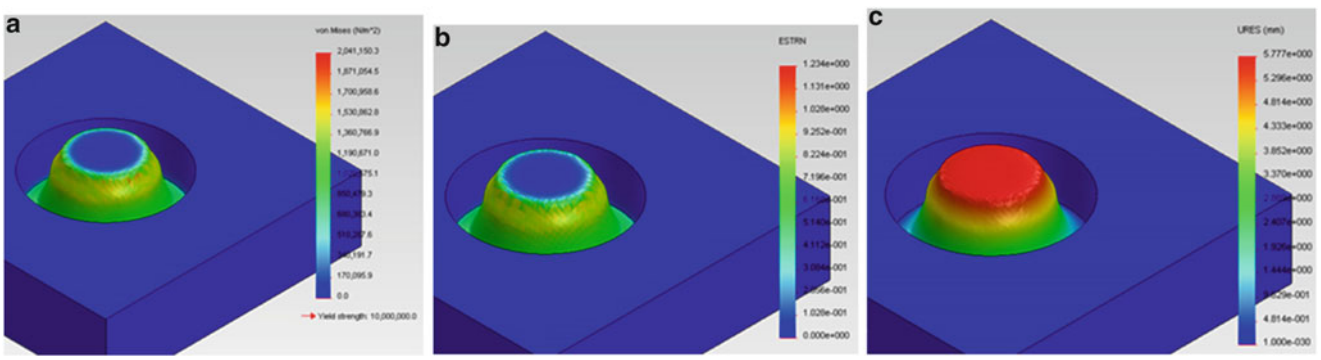

Fig. 8.6 FEA study results for a displacement of 12 mm. (**a**) Stress, (**b**) Strain, (**c**) Displacement. Results indicate that the PDMS well does not fail at this displacement

8.6 Cell Culture

Osteocyte-like MLO-Y4 cells (a generous gift from Dr. Lynda Bonewald) were cultured using a previously established protocol [10]. Cells were cultured using minimum essential alpha medium (α-MEM, Gibco) supplemented with 5 % fetal calf serum (Hyclone), 5 % fetal bovine serum (Hyclone), and 1 % penicillin/streptomycin (Pen/Strep, Invitrogen). Cells were maintained at 5 % CO_2 and 37 °C in 25 cm^2 flasks coated with rat tail collagen type I (BD Bioscience) in 0.02 M acetic acid (Sigma) at a concentration of 5 μg/cm^2 for 1 h prior to rinsing with Dulbecco's phosphate buffered saline solution with calcium and magnesium (D-PBS, Calcium and Magnesium, Hyclone). Cells were passaged between 70 and 80 % confluency using 0.05 % Trypsin-EDTA, and cells were fed every 3 days. For experimentation, cells were seeded onto PDMS well structures at a density of 2×10^4 cells/cm^2. PDMS well structures were collagen coated overnight before being placed in a cell culture holding system in a petri dish. Two Kimwipes were dipped in sterile water and wrapped around the border of the petri dish to generate a humidified chamber and promote cell growth. Cells were seeded 4 days prior to experimentation to allow cells to reach a high confluency and exhibit characteristic protein expression including sclerostin [11].

8.7 Loading Induced Differential Activity

For loading, the cell culturing system was removed from the incubator and placed in the alignment block on top of the microloading platform. The actuator displacement was increased until contact was detected based on force registration of the load cell. Following contact, displacement was increased to the desired level and maintained for 15 min, thus loading the PDMS well structure and cells. In this study, a displacement of 8 mm as reported by the microactuator controller was used for three samples and repeated three times. After loading, the PDMS well structure was stained and quantified for viability.

Viability staining was performed using a lactate dehydrogenase (LDH) stain. A base staining solution consisting of 5 % polypep (Sigma–Aldrich) and 2 mM of gly–gly (Sigma–Aldrich) was prepared in Hank's buffered salt solution (HBSS). Following, 1.75 mg/ml of nicotinamide adenine dinucleotide (Sigma–Aldrich) and 60 mM lactic acid (Sigma–Aldrich) were added to the base solution, and the solution was brought to a pH of 8.0. Three mg/ml of nitroblue tetrazolium were then added to the LDH solution before incubating the PDMS well structure with 0.5 ml of the staining solution for 2 h. Following the LDH stain, cells were washed with HBSS prior to fixation for 15 min in 4 % paraformaldehyde in PBS before being imaged.

Following imaging, quantification was completed using ImageJ (National Institute of Health). This process consisted of analyzing one positional reference grid at a time. For this study, the central positional reference grid was analyzed, as well as grids 3 and 6 above, right, below, and left of center. In each positional reference grid, 40 cells were randomly chosen and selected in ImageJ. The pixel intensity values were recorded throughout the cell, with the average for each cell determined. Ten background areas were also chosen in each positional reference grid, and the average background pixel intensity was subtracted from the average for each cell. This adjusted for the background in each positional reference grid, allowing comparisons between grids and experiments. Statistical comparisons were made using 1-way ANOVA with a Tukey post hoc test ran to determine statistically significant variances, as well as unpaired t tests. All comparisons between the same locations (middle, 3 away, 6 away, and overall well) were statistically significant for a P value of 0.05, Fig. 8.7. These regions were chosen as a different strain was experienced as a function of loading, Fig. 8.6.

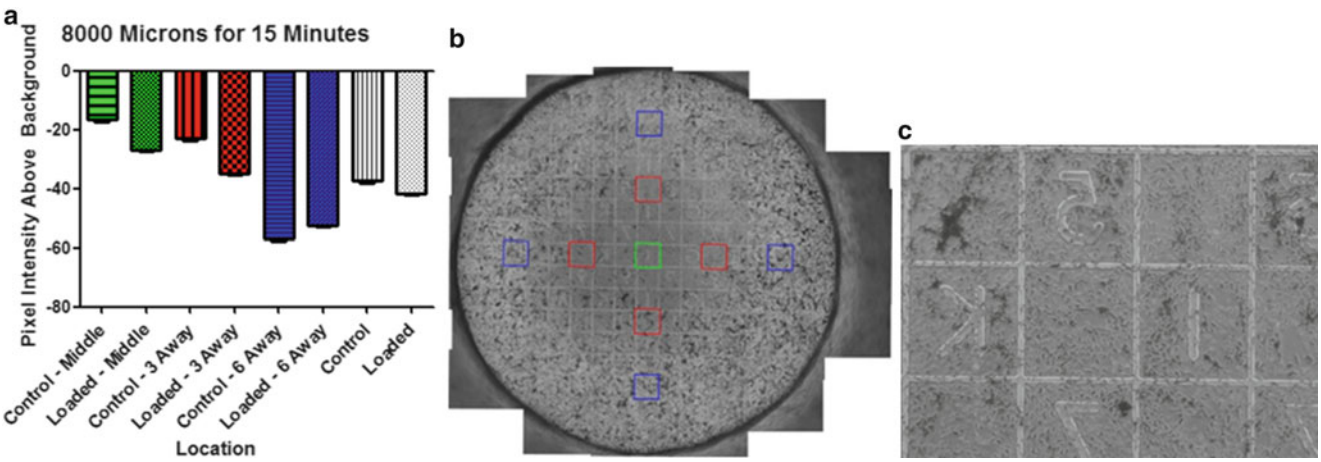

Fig. 8.7 (**a**) Loading results for loads of 8,000 μm for 15 min. All differences are significant, with a p value <0.05. (**b**) Example mosaic showing the entirety of the PDMS well following loading. (**c**) Example of original image taken following experimentation and used to form the mosaic

8.8 Discussion

In this study, a microloading platform was developed and characterized for the in vitro loading of MLO-Y4 cells on a PDMS well structure. Loading was done using a cylindrical platen to tent the PDMS well from below, stretching the material. For this study the microloading platform was designed and characterized, by insuring an accurate displacement was reported by the microactuator controller. An alignment block and cell culture holding system were also designed to increase the accuracy and reproducibility of loading, and to eliminate preloads, respectively. A PDMS well structure was designed with a positional reference grid, allowing consistent imaging of the entirety of the PDMS well and comparisons of cells before and after loading. A FEA model was ran to insure that the PDMS well structure would not fail during experimentation. Following the development and characterization of the microloading platform and PDMS well structure, initial loading experiments were performed. These studies demonstrated changes in lactate dehydrogenase staining in osteocyte-like MLO-Y4 cells, indicating changes in metabolic activity or viability. This study serves as an important first step in developing a model for investigating the role of osteocytes in the mechanotransduction process for bone. While further work must be performed, such as incorporating additional cell types and studying factors such as protein expression, this initial work demonstrates that this microloading platform can be used to mechanically load cells and induce differential cellular responses.

Acknowledgments Support for this work was provided by an NSF CAREER Award.

References

1. Brown T (2000) Techniques for mechanical stimulation of cells in vitro: a review. J Biomech 33(1):3–14
2. Jones HH, Priest JD, Hayes WC, Tichenor CC, Nagel DA (1977) Humeral hypertrophy in response to exercise. J Bone Joint Surg 59(2):204–208
3. Morey ER, Baylink DJ (1978) Inhibition of bone formation during space flight. Science 201(4361):1138–1141
4. Rath AL, Bonewald LF, Nicolella DP (2007) Tissue strain amplification at the osteocyte lacuna; a microstructural finite element analysis. J Biomech 40(10):2199–2206
5. Burger EH, Klein-Nulend J, Smit TH (2003) Strain-derived canalicular fluid flow regulates osteoclast activity in a remodeling osteon – a proposal. J Biomech 36(10):1453–1459
6. Wang Y, McNamara LM, Schaffler MB, Weinbaum S (2008) Strain amplification and integrin based signaling in osteocytes. J Musculoskelet Neuronal Interact 8(4):332–334
7. Taylor AF, Saunders MM, Shingle DL, Cimbala JM, Zhou Z, Donahue HJ (2005) Mechanically stimulated osteocytes regulate osteoblastic activity via gap junctions. Am J Physiol Cell Physiol 292(1):545–552
8. Schneider F, Draheim J, Kamberger R, Wallrabe U (2009) Process and material properties of polydimethylsiloxane (PDMS) for optical MEMS. Sensors Actuators A Phys 151(2):95–99
9. Mata A, Fleischman A, Roy S (2005) Characterization of polydimethylsiloxane (PDMS) properties for biomedical micro/nanosystems. Biomed Microdevices 7(4):281–293
10. Rosser J, Bonewald LF (2012) Studying osteocyte function using the cell lines MLO-Y4 and MLO-A5. Methods Mol Biol 816(1):67–81
11. York SL, Arida AR, Shah KS, Sethu P, Saunders MM (2012) Osteocyte characterization on polydimethylsiloxane substrates for microsystems applications. J Biomimet Biomater Tissue Eng 16(1):27–42

Chapter 9
Development of a Multi-Strain Profile for Cellular Mechanotransduction Testing

J.D. King, D. Hayes, K. Shah, S.L. York, P. Sethu, and M.M. Saunders

Abstract Mechanosensitive cells, such as osteocytes in bone, are capable of translating mechanical stimuli into cellular responses. This phenomenon can be widely found in cells throughout the body, and yet little is known about the mechanisms and pathways by which this occurs. Research in this field has focused on creating in vitro models that better reflect the in vivo environment in order to study these mechanisms and pathways. Where many variations on these systems exists, one major goal in improving these models is to use fewer cells in order to observe the response of specific cells and possibly more meaningful data. Using an uniaxial loading device, a substrate with cells seeded onto it can be mechanically strained and the response of these fewer cells can be quantified. In this study, two substrates of varying geometry are proposed that allow for a gradient of mechanical strains to be applied to cultured cells. These designs are characterized and compared using both physical and simulated testing. Utilizing designs, such as the ones used for these substrates, enables the effects of a wide range of mechanical strains on cells to be observed and studied under identical culture and loading environments.

Keywords Mechanotransduction • Strain gradient • Uniaxial loading • Polydimethylsiloxane (PDMS) • In vitro

9.1 Introduction

Mechanotransduction is a field of study that focuses on understanding the translation of mechanical stimuli to cellular responses [1]. This field is important to biomedical research due to the fact that tissues develop in environments with constant physical forces surrounding them such as gravity, movement, and pressure [1]. These forces can help to shape and control the function of these tissues during cellular activities such as differentiation, migration, and signal transmission [2]. Many cells are known to be mechanosensitive in this sense including cartilage [3], smooth muscle [4], endothelial [5], and bone [6]. Where some cellular mechanisms related to mechanotransduction have been discovered [6], many have yet to be elucidated due to the staggering complexity of the cellular interactions. Many of these complexities come from the in vivo environment in which these cells develop. For this reason in vitro experimentation on these cells and tissues can help to isolate specific cellular responses under quantifiable mechanical stimuli [7].

Creating in vitro mechanotransduction models enables simulation of cellular responses to mechanical stimuli in a controlled, physiologically relevant, and accurate manner. Many variations of these systems exist with each having their own advantages and disadvantages depending on the need of any specific experiment. These include systems for applying longitudinal stretch, out-of-plane circular substrate distention, in-plane substrate distention, and fluid shear [7]. In many of these systems cells are grown on a substrate that is loaded into the system where average cellular response to stimuli can then be measured. For this reason it is important to consider a substrate's mechanical nature in order to asses if it will be ideal for specific experimental parameters. For example, with a fluid shear model cells are generally seeded onto a rigid glass slide

J.D. King (✉) • D. Hayes • K. Shah • S.L. York • M.M. Saunders
Department of Biomedical Engineering, The University of Akron,
Auburn Science and Engineering Center 275 West Tower, Akron, OH 44325, USA
e-mail: jdk31@zips.uakron.edu

P. Sethu
Division of Cardiovascular Disease, The University of Alabama at Birmingham, Mccallum Basic Health Sciences Building 290 A,
1918 Birmingham, AL 35294, USA

F. Barthelat et al. (eds.), *Mechanics of Biological Systems and Materials, Volume 7: Proceedings of the 2014 Annual Conference on Experimental and Applied Mechanics*, Conference Proceedings of the Society for Experimental Mechanics Series,
DOI 10.1007/978-3-319-06974-6_9,

that forms the base of a parallel plate chamber [8, 9], while in-plane substrate distention utilizes a more flexible, generally silicone, substrate for seeding the cells. This difference in material is due to the distinct difference of how the mechanical stimuli is applied [10].

In addition, current in vitro mechanotransduction systems may not accurately represent net cell responses. For example, typical loading of bone and endothelial cells is performed using fluid shear models where fluid flow occurs over a monolayer of millions of cells [11, 12]. This type of cellular response characterization averages the response from many cells instead of the exact response of a cell to a known strain. In order to better understand this cellular response to strain, models which use fewer cells are needed in order to find a specific response instead of an average. For these reasons a system is needed to apply precise, known mechanical stimuli to small cell populations in order to quantify the cellular response in a more exact and meaningful manner. The first step is creating a model to mimic a more precise cellular response.

In bone research there is much interest in understanding the relation between mechanical stimuli and cellular response. This is due to the known reaction that bone has to mechanical load. This relationship is outlined by Wolff's Law and known as mechanical adaptation where an increase in mechanical loading on the bone leads to an increase of bone mass and strength while a decrease in loading on bone leads to a decrease in bone mass and strength [13]. In vivo studies have replicated this reaction in both human and animal models [14, 15]. Even though the general idea that bone cells react to mechanical stimuli is well established, many of the underlying cellular mechanisms that allow for this mechanism to occur remain unclear.

In order to understand the strain where these mechanosensitive cells react we need to first observe the cells' reaction to different ranges of strains. This will then allow for the ability to focus in on the more specific strains in which mechanotransduction is measureable. For this reason a unique profile was formed from elastomeric polydimethylsiloxane (PDMS). This material was chosen due to its optical transparency, ease of fabrication, microscale features, and elastic nature. This substrate has been shown to support cellular growth, specifically with osteocytes [16], and with a variety of cross-sectional thicknesses, allows for a range of strains to be applied to these cells under identical culture and loading conditions. With a well characterized substrate such as this the ability to view cellular response initiation becomes possible. This study analyzes two design profiles and characterizes the strains displayed on each profile with respect to the overall applied strain.

9.2 Experimental Procedure

This study focused on characterizing two profiles designed to create a range of strains under small overall displacements. Numerical [Finite Element Analysis (FEA)] and experimental testing were performed to characterize the response of varying profiles thickness as a function of overall strain.

9.2.1 Profile Design

The two profiles created for this testing were designed to be loaded utilizing an uniaxial load and created strain ranges over the substrate. Both of the designs were the same length and width with the side profile being the only difference between the designs, Fig. 9.1.

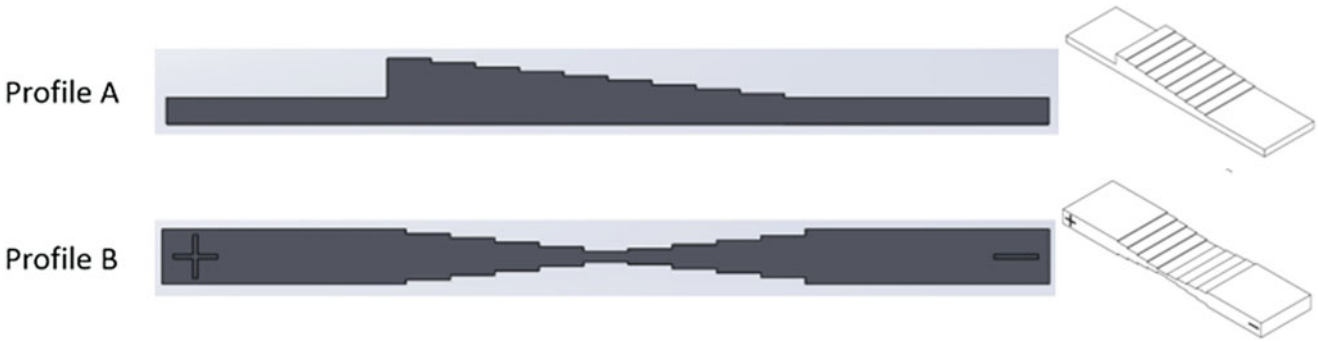

Fig. 9.1 Side profile view of the two designs

Fig. 9.2 Numbered profile steps by cross-sectional area thickness (1 represents the thickest while 9 represents the thinnest cross-sectional area)

Table 9.1 PDMS material strength properties used for FEA simulations

PDMS material properties	
Elastic modulus (MPa)	14.47
Poisson's ratio	0.49
Mass density (kg/m^3)	0.97
Ultimate tensile strength (MPa)	2.59

Profile A was designed with steps which vary from a larger cross-sectional area that decreased linearly down to the smallest cross-sectional area. Profile B was designed in order to keep the uniaxial load along the centerline of the profile. This profile was intended to produce a more uniform strain along the profile. This design incorporated staggered step sizes where the middle step had the smallest cross-sectional area followed by the step directly to the right of the middle step and then followed by the one to the left. The steps increased in size in this manner until they reached the clamp area. The plus and minus sign on the side of the profile was to show which side had the larger of the staggered steps. In order to relate the data to the step cross-sectional area the steps were numbered with 1 correlating to the step with the largest cross-sectional area and 9 correlating to the step with the smallest cross-sectional area, Fig. 9.2.

9.2.2 Fabrication

The molds to create the profile designs were made using Solidworks 2013 and saved as stl files. The stl files were sent to Fineline Prototyping (Willmington, NC) for stereolithography using Phototherm, a high temperature resistant material. Once the top and bottom molds were made they were assembled together and clamped in place. Then a silicone elastomer, PDMS (Dow Corning, Midland, MI), mixed 10:1 with a cross-linking agent was mixed, degassed and poured into the assembled mold and cured at 80 °C for 12 h in a convection oven. Following curing the molds were disassembled and the cured PDMS parts were taken out of the molds and washed with acetone and isopropyl alcohol and air dried.

9.2.3 FEA

Models for both profile designs were generated in Solidworks 2013. Using this same software and the material properties from mixtures gained from a previous study [17] FEA simulations were performed for both profiles. Table 9.1 displays the properties used to define the PDMS material for the simulations.

The models for both profiles were designed with a 22.86 mm gauge length so that all of the steps on the profiles were exposed and experienced the strain. Restrictions were placed on either end of the profile to simulate the friction clamps holding the sample in place. These restrictions consisted of one end having fixed nodes for both of the surfaces that were in contact with the clamp Fig. 9.3a, and the opposite end had rollers on both of the surfaces that the clamp was in contact with Fig. 9.3b. This allowed for both of the simulated clamps to remain on axis during loading simulating the physical tests in the loading system. A remote displacement was used to simulate the applied strain to the profile. This remote displacement was applied to the whole surface where the friction clamp contact was simulated with rollers Fig. 9.3c. This location was chosen to simulate a no slip condition in the boundaries of the friction clamp at any time during testing.

Remote displacements of 0.009 and 0.0225 mm, 1 and 2.5 % strain respectively, were applied to the models. The node and element properties for the models are displayed in Table 9.2.

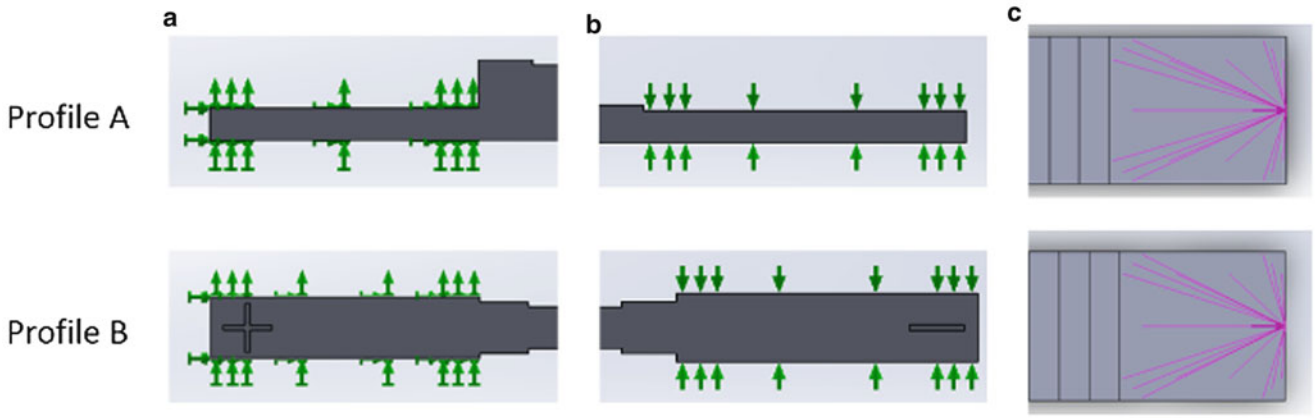

Fig. 9.3 FEA model restrictions (**a**) fixed points on model, (**b**) roller points on model, (**c**) applied remote displacement

Table 9.2 Node and element properties in FEA model

	Degrees of freedom	Elements	Nodes
Profile A	361,995	119,444	86,045
Profile B	248,247	57,740	85,767

9.2.4 Physical Test

Physical tests were performed with the stepped profiles in order to quantify the strains displayed on each step with relation to overall strain. A gauge length of 22.86 mm was used so that all of the steps on the profiles were uncovered by the friction clamps holding them into the system. Strain rates of 2.08 mm/s were used to apply the strains. Samples were loaded on a small-scale testing machine via poly-carbonate friction clamps built in-house [18]. These samples were loaded to 2.5 % strain with strain measurements taken for each step at overall strain increments of 0.5 %.

To measure the strains during loading a non-contact method was utilized. This method used a camera (8 megapixels at 30 fps) mounted perpendicular to the stepped profile during loading. Video of the experiments was recorded and frames from the video were extracted at desired overall strains using Microsoft Movie Maker 2012. Using ImageJ software (NIHImage, Bethesda, MD, USA), strains were calculated by measuring the change in length of each step 5 separate times and comparing those values to the original length of the step. This measurement resulted in the strain per step while the samples had an overall applied strain. This testing was performed on 4 samples per profile.

9.3 Results

9.3.1 FEA

Data collected from these tests included both the qualitative images of the strain fields and deformations during loading, as well as the average strains per step during loading for all loading conditions. Figure 9.4 displays the side profile of the samples under a 2.5 % overall strain with strain gradients normalized to each other between 0 and 11 % overall strain. The gauge length was set for the entire area not covered by the friction clamps during loading. In Fig. 9.5a, b top projected view of the profiles is displayed with strain gradients normalized to each other between 0 and 11.0 % overall strain. The average strain on each step was measured for each overall testing strain. This data is presented in Fig. 9.6a, b.

9.3.2 Physical Test

From the frames extracted from the video taken of the loaded profiles, strains from each step were measured using distance measurements made in ImageJ. These strains were recorded for all samples and averaged. In order to view the data in a more appropriate manner the data was clumped into bins that were defined by the thickness of the cross-sectional area. The bins consisting of the 3 thinnest steps, the 3 thickest steps, and the steps ranging in the middle thicknesses, Table 9.3.

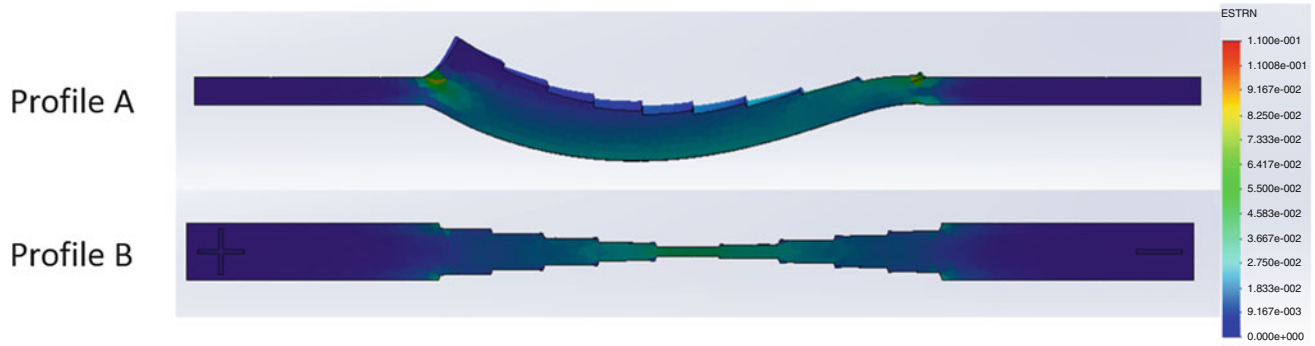

Fig. 9.4 Side view of profiles during FEA loading. Color spectrum of strains set the same for both designs

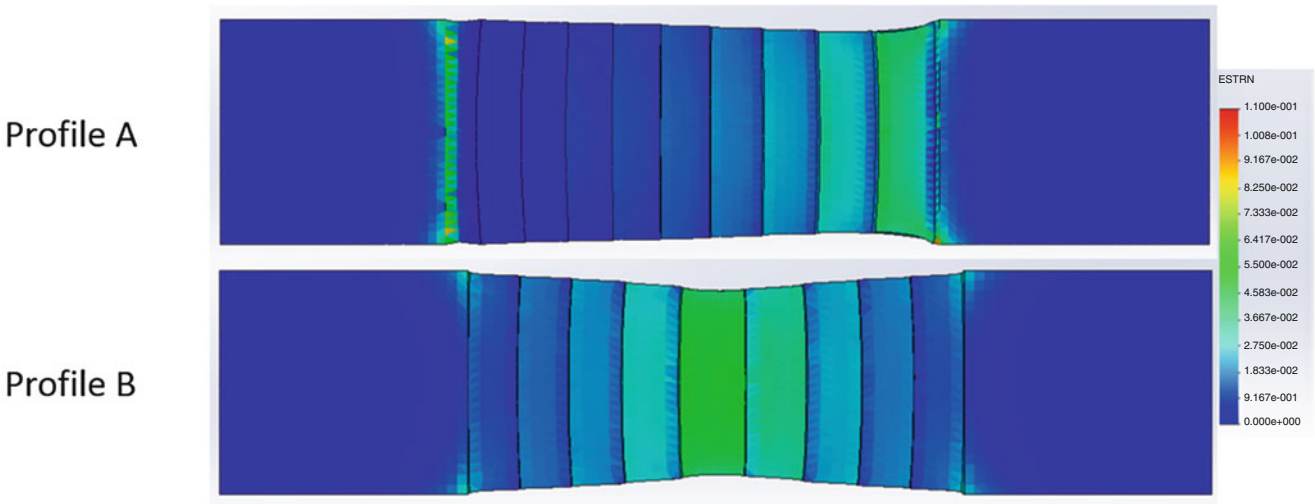

Fig. 9.5 Top view of profiles during FEA loading. Color spectrum of strains set the same for both designs

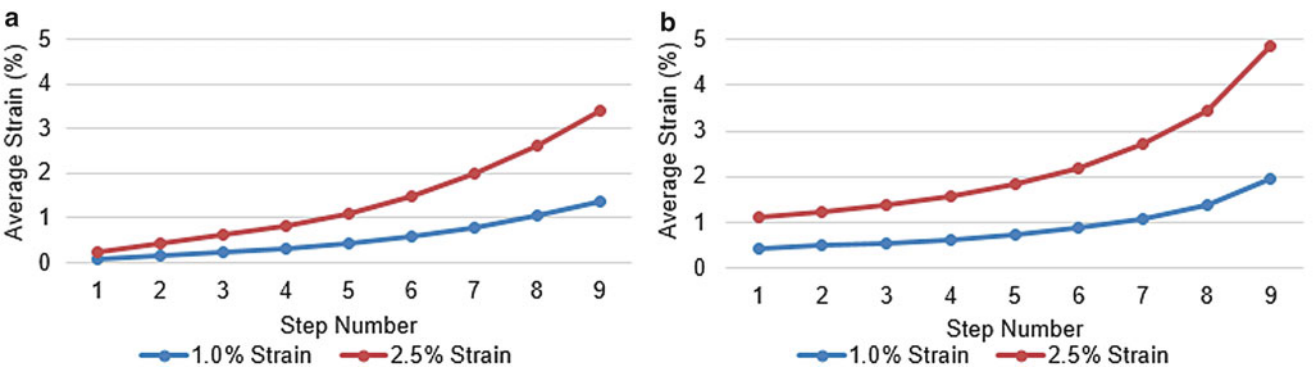

Fig. 9.6 Resulting average strain per step during overall strains of 1.0 and 2.5 % for (**a**) Profile A and (**b**) Profile B

Table 9.3 Bin contents

Thickest bin	Middle bin	Thinnest bin
Steps 1, 2, and 3	Steps 4, 5, and 6	Steps 7, 8, and 9

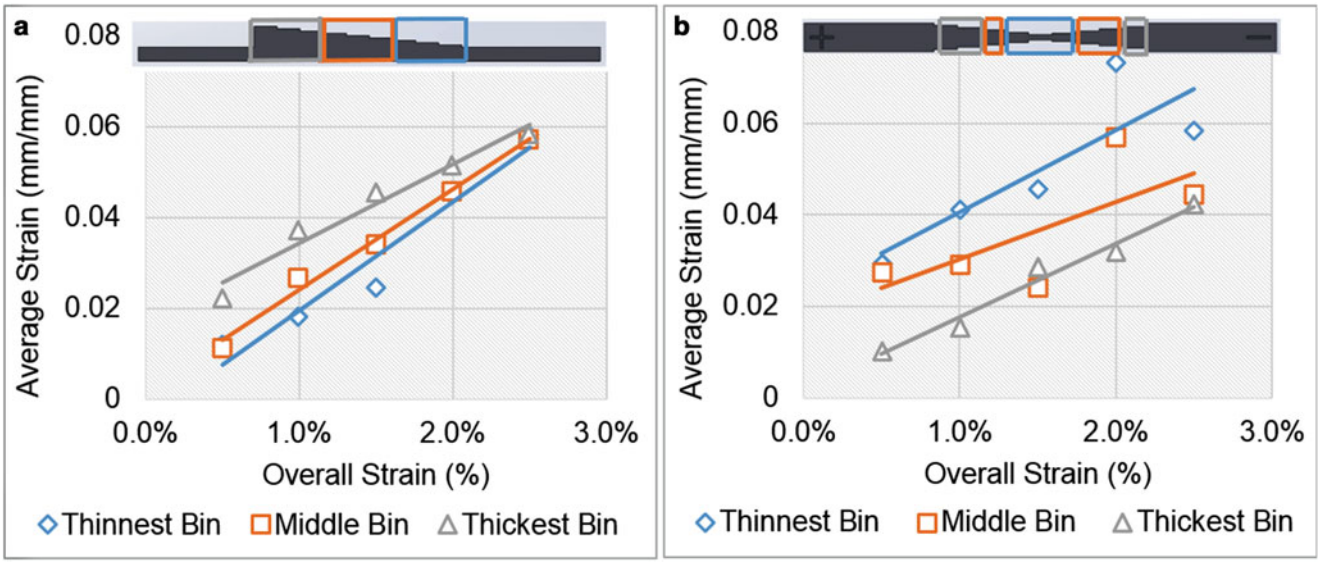

Fig. 9.7 Average measured physical strains for different thicknesses on (**a**) Profile A and (**b**) Profile B

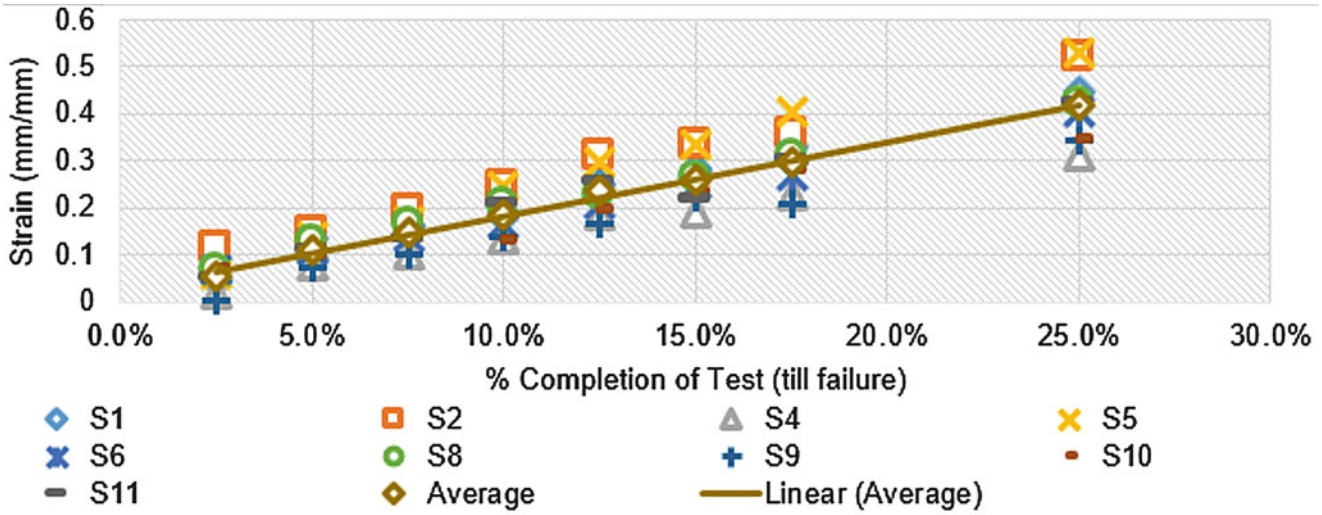

Fig. 9.8 Uniform thickness PDMS samples loaded to failure

The data was plotted and regression lines were fit for each bin data set, Fig. 9.7a, b. To understand how the PDMS responds to higher strains several samples of uniform thickness were loaded out to failure and strain was measured as a function of completion to sample failure, Fig. 9.8.

9.4 Discussion

One notable difference between the two profile designs existed in the side profile view under strain from the FEA model, Fig. 9.4. Here it was observed that while Profile B had no bending off axis from the load, Profile A had a very distinct bend as the strain was applied. This bend did not significantly affect the average strains on the steps which increased with decreasing cross-sectional step area. The bending is noted due to the possibility of introducing the cells on these steps to not only tensile forces from the strain, but to compressive forces from bending.

From the physical testing it can be noted that Profile A reacted under load counterintuitive to what was anticipated. The general assumption for strain was that as cross-sectional step area increased the strain would decrease under identical loading conditions. And conversely as cross-sectional step area decreased the strain would increase under identical loading conditions. On Profile A in Fig. 9.7a it was observed that during the physical testing of this profile the strain increased with an increase in cross-sectional step area. This was not observed in Profile B, showing that at these low strains the geometry of Profile A exhibited a less desirable strain range. At higher overall strains it is believed that this is not an issue due to PDMS having a more linear nature at higher strains, Fig. 9.8. This abnormal strain behavior may be corrected by altering the manner in which the profile is clamped into the system. One example of this could be to alter the clamp locations such that its contact is with first and last step. However for the purpose of stimulation cells, it is critical to characterize the mechanical performance at the low strain ranges (<5 %).

Due to the use of low strains to create a more physiological relevant strain range in our applications, Profile B performed in a more desirable manner. It is important to note that where the profiles did not display a simple linear curve that correlated step cross-sectional area to average step strain, such as the low strain ranges, mechanical characterization was possible. The goal of this work was to investigate various profile geometries to select a substrate that would allow for a range of strains to be applied to seeded cells in a physiologic range. With this goal, Profile B was superior to Profile A.

Acknowledgments The authors would like to acknowledge Ryan Manges for his help with preliminary testing on this project. Support for this work was provided by a NIH NIDCR AREA (R15) Award.

References

1. Ingber DE (1999) Tensegrity: the architectural basis of cellular mechanotransduction. Annu Rev Physiol 59(1):575–599
2. Katsumi A et al (2004) Integrins in mechanotransduction. J Biol Chem 279(13):12001–12004
3. Ramage L et al (2009) Signaling cascades in mechanotransduction: cell–matrix interactions and mechanical loading. Scand J Med Sci Sports 19(4):457–469
4. Hisada T et al (1993) Stretch-inactivated cationic channels in single smooth muscle cells. Pflügers Arch 422(4):393–396
5. Hoyer J et al (1996) Up-regulation of pressure-activated Ca (2+)-permeable cation channel in intact vascular endothelium of hypertensive rats. Proc Natl Acad Sci USA 93(20):11253–11258
6. Orr AW (2006) Mechanisms of mechanotransduction. Dev Cell 10(1):11–20
7. Brown TD (2000) Techniques for mechanical stimulation of cells in vitro: a review. J Biomech 33(1):3–14
8. Tzima E et al (2005) A mechanosensory complex that mediates the endothelial cell response to fluid shear stress. Nature 437(7057):426–431
9. Pahakis MY et al (2007) The role of endothelial glycocalyx components in mechanotransduction of fluid shear stress. Biochem Biophys Res Commun 355(1):228–233
10. Sotoudeh M et al (1998) A strain device imposing dynamic and uniform equi-biaxial strain to cultured cells. Ann Biomed Eng 26(2):181–189
11. Bacabac RG et al (2004) Nitric oxide production by bone cells is fluid shear stress rate dependent. Biochem Biophys Res Commun 315(4):823–829
12. Young SR et al (2001) Non-overlapping functions for Pyk2 and FAK in osteoblasts during fluid shear stress-induced mechanotransduction. PLoS ONE 6(1):e16026
13. Burger EH, Veldhuijzen JP (1993) Influence of mechanical factors on bone formation, resorption and growth in vitro. Bone 7:37–56
14. Sztefek P et al (2010) Using digital image correlation to determine bone surface strains during loading and after adaptation of the mouse tibia. J Biomech 43(4):599–605
15. Maïmoun L, Sultan C (2011) Effects of physical activity on bone remodeling. Metabolism 60(3):373–388
16. York SL et al (2012) Osteocyte characterization on polydimethylsiloxane substrates for microsystems applications. J Biomimet Biomater Tissue Eng 16:27–42
17. Karan SS, York SL, Sethu P, Saunders MM (2013) Developing a microloading platform for applications in mechanotransduction research, vol 5, Mechanics of biological systems and materials. Springer, New York, pp 197–205
18. Saunders M, Donahue H (2004) Development of a cost-effective loading machine for biomechanical evaluation of mouse transgenic models. Med Eng Phys 26:596–603

Chapter 10
Pull-Off Adhesion Measurements on *C. Elegans*

Michael W. Keller, Kevin A. Adams, and Roger Mailler

Abstract The surface adhesion between *C. elegans* and the agar plates on which they are commonly grown has yet to be accurately quantified. *C. elegans* are a scientifically important species of nematode whose simple structure allowed the first mapping of the complete nervous system in a multicellular organism. One of the current topics of research in the *C. elegans* community is the investigation of neuronal function in locomotion. Locomotion models derived from mathematical analysis of nematode motion and surface interaction are frequently employed to investigate the influence of neuronal function in locomotion. Surface interactions, such as adhesion energy, play a critical role in the development of these models, but measurements of these parameters have not yet been performed. This paper presents the measurement of surface adhesion energy of nematodes on agar surfaces using a direct pull-off experiment. Adhesion energy was found to be $W = 4.94 \pm 1.19$ mJ/m^2 for the wild type.

Keywords Surface adhesion • *C. elegans* • JKR adhesion • Adhesion modeling • Biological system

10.1 Introduction

Caenorhabditis elegans (C. Elegans) is a small (1 mm in length) nematode that can be found living in decaying organic matter in many parts of the world. It lives by feeding on bacteria and is capable of reproducing in about 3 days under the right conditions. Like other members of the nematode (Nematoda) family, the body of *C. elegans* is composed of two concentric tubes separated by a pseudocoelom. The inner tube is in the intestine and the outer tube consists of the hypodermis, muscles, nerves and the gonads. The pseudocoelom is filled with a hydrostatically pressurized fluid that helps maintain the shape of its body. *C. elegans* is a significant biological model and is the only multicellular animal to have an entire connectome for both neural and synaptic connections [1]. One of the current active topics in *C. elegans* research is the development of models for neuron activity during locomotion. These computational models are combined with experimentation using mutant worms with specific neurons deactivated.

Nematode locomotion is frequently studied on agar plates [2–5] and an accurate, physics-based model of the forces required to initiate and sustain motion is important to aid understanding of the interaction between the observed motion of the nematode and the influence of the environment. Several modeling attempts have been made [4, 5] frequently using lubrication-models to describe the motion of the relatively slender nematode through a thin liquid layer on the top surface of the agar plate. An example of a recently proposed model was published by Shen and coworkers [5]. In this and similar models, the surface tension or adhesion energy between the nematode is either neglected or has been described as unimportant based on the mathematical form of the model. Neglecting the importance of surface adhesion is typically supported by experiments where the surface energy of the agar is modified through the addition of a surfactant. Worm motion is then analyzed to see if there are differences from motion analyzed on an unmodified agar surface.

M.W. Keller (✉) • K.A. Adams
Department of Mechanical Engineering, The University of Tulsa, 800 S. Tucker Dr., Tulsa, OK 74104, USA
e-mail: mwkeller@utulsa.edu

R. Mailler
Department of Computer Science, The University of Tulsa, 800 S. Tucker Dr., Tulsa, OK 74104, USA

F. Barthelat et al. (eds.), *Mechanics of Biological Systems and Materials, Volume 7: Proceedings of the 2014 Annual Conference on Experimental and Applied Mechanics*, Conference Proceedings of the Society for Experimental Mechanics Series,
DOI 10.1007/978-3-319-06974-6_10,

However, recent research has indicated that *C. elegans* has a feedback system that modulates worm muscle response based on the environment [6], implying that simple surface tension modification experiments may not capture the entire effect of surface forces on nematode locomotion.

In this paper, we use a custom designed load frame to perform pull-off experiments on individual nematodes. A fracture-mechanics model of adhesion is then used to extract the surface energy between the nematode and an agar surface.

10.2 Experimental Methods

10.2.1 C. elegans Growth and Maintenance

Maintenance and culturing of nematodes was performed as outlined in [2]. Nematodes were grown on standard Nematode Growth Media (NGM) Lite plates with OP50 *E. coli* and incubated at room temperature [7]. The cultured worms were obtained from the *Caenorhabditis* Genetics Center and were wild type *N2*.

10.2.2 Experimental Setup

The pull-off system was adapted from a micro mechanical compression frame described in [8]. Displacement was applied at a rate of 1 μm/s using a stepper actuator (Physik Instrumente M-229.25S) controlled via a computer interface and accurate to 50 nm. The actuator included a displacement sensor that allowed feedback information of current crosshead displacement. Load data were acquired from a 10 g load cell (Transducer Techniques GSO-10) via a DAQ system (NI 9237) and associated software from National Instruments. The LabView software also served as the PID control loop that enabled operation in both load and displacement control modes. Images of the nematode during the compression cycle were captured through a microscope (Leica) by a monochrome CCD Camera (Allied Vision Technologies Pike F-505B). The entire system was mounted on vibration isolation. The system was constructed such that the load cell was fixed and the agar pad was attached to the actuator. This arrangement was selected to minimize noise generated by vibrations during stepper motor translation.

10.2.3 Agar Pad Production

One critical factor to running successful *C. elegans* pull-off experiments was ensuring that the agar test surface was as flat and parallel as possible. In order to achieve this, rectangular prism shaped molds were made from aluminum foil. Distilled water was then boiled and mixed with agar powder to produce a 2.5 wt% solution. Before the molten agar was poured into the aluminum molds, it was degassed using a vacuum pump to remove air bubbles. After cooling the molds to room temperature, the foil was then removed from the solidified agar bars, which were then refrigerated in a sealed container to prevent moisture loss. When an agar pad was needed for testing, it was cut from an agar bar using two parallel razor blades mounted approximately 4 mm apart. To minimize the drying effects of exposing the agar pads to air, each pad was cut just prior to the start of a test.

10.2.4 Pull-Off Experiment

For each pull-off experiment, an adult *C. elegans* specimen was picked from a growing plate of NGM agar, using a small platinum wire that had been flattened at one end and mounted to the end of a pipette for handling. The nematode was then placed on an empty agar plate, where it was anesthetized using one drop of a 1:100 sodium azide (NaN$_3$) aqueous solution. A small piece of glass slide mounted in a threaded collar was then prepared by coating its upper surface in a thin layer of adhesive (Elmer's multipurpose spray adhesive). Once the nematode had stopped moving, it was picked using the

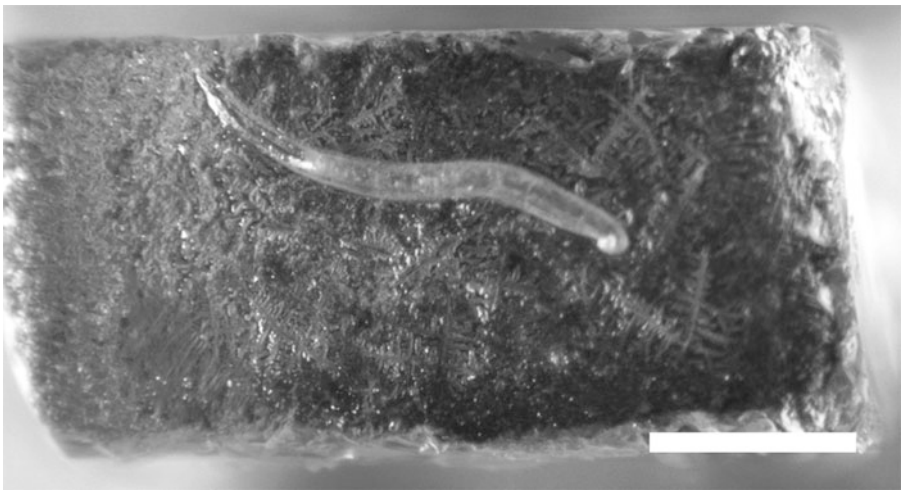

Fig. 10.1 Image of a nematode affixed to the loading block, scale bar is 500 μm

platinum wire and secured to the adhesive on the piece of glass slide as shown in Fig. 10.1. An image was taken of the nematode to allow for the measurement of the nematode diameter and length by image analysis software (ImageJ). The loading rod with the attached worm was then inserted into the test frame within 5 min of the nematode attachment to the glass compression rod. Tests were run in load control with a maximum compressive force of 0.20 mN, selected based on the sensitivity of the control system for the compression frame. After reaching the maximum compressive load, the actuator reversed direction until the nematode and the agar were no longer in contact.

10.3 Model

A simple JKR-adhesion model was used to estimate the adhesion energy of the nematode-agar interface. The model assumes that the nematode can be approximated using a cylinder. This approximation causes some error in the estimated value of the adhesion energy W as the nematode tapers to either end. We are currently investigating the use of a model based on an ellipsoid. From the work performed by Chaudhury and coworkers [9], we use the following relationship between pull-off load and adhesion energy

$$W = \left(\frac{P^3 L^3}{3.16 E' R}\right)^{1/2} \tag{10.1}$$

In this relationship, P is the pull-off load, L is the length of the nematode, R is the radius of the nematode, and E' is a combined modulus given by

$$E' = \frac{4}{3}\left(\frac{1-\nu_n^2}{E_n} + \frac{1-\nu_A^2}{E_A}\right)^{-1} \tag{10.2}$$

The values of the Poisson ratios for the nematode ν_n and the agar surface ν_A are assumed to be 0.5. The value for the agar modulus was taken from previous testing and was $E_A = 254$ kPa [10]. The value of the nematode "modulus" was estimated using direct compression of an entire nematode on a glass surface and calculated using a hertzian contact model. This returned an estimate for the modulus of the entire nematode as if it were homogenous. Compression of six individuals found this value to be $E_n = 14.9$ MPa.

10.4 Results and Discussion

Results from a repeated single-nematode pull-off test are shown in Fig. 10.2. Each of the traces in Fig. 10.2 occurred approximately 5 min apart. The data for these traces were smoothed using a moving average function with a window size of ten data point and a cubic spline was then fit to the smoothed data to extract the maximum load. Since this test was load-controlled, the maximum load experienced by the nematode remained constant for each compression-pull-off cycle. However, the maximum tensile load generated by the adhesive force between the nematode and the agar pad changed as time progressed. As shown by the sloped pull-off curve in Fig. 10.2, the nematode did not "snap-off" from the agar surface. The sloped unloading curve is likely the result of curvature over animal length. Fracture of the animal-agar contact begins at the head or tail of the animal and proceeds inward to the center.

This reduction is approximately exponential, which we interpret as an indicator of either the nematode or the agar pad is drying. This is, of course, not the only interpretation of the observed adhesion energy reduction. Further visual observations of the agar also indicate that the drying of the test pad is dominating the reduction in adhesion, though nematode drying cannot be ruled out. However, the displacement from initial contact with the agar to maximum compressive load, see Fig. 10.2, is approximately constant for all tests indicating that the elastic response of the nematode and the agar are remaining relatively constant during the compression experiment.

As in the case of the maximum pull-off forces, the drying trend can also be observed in the calculated adhesion energies in Fig. 10.3. Fitting an exponential through this data allows for an estimate of the fully hydrated $t = 0$ value of surface energy to be calculated. From the intercept value in Fig. 10.3 we find an adhesion energy of $W = 4.94 \pm 1.19$ mJ/m^2. This value is similar to what would be calculated using the surface tension of water implying that the water bridge between the nematode and agar surface is dominating the adhesion process. Further studies on cuticle mutants would be required to substantiate this observation.

In addition to the comparison described above, we also note that our measured value of the adhesion energy is approximately the same as estimates used in recent theoretical studies of nematode motion [5]. The value assumed by

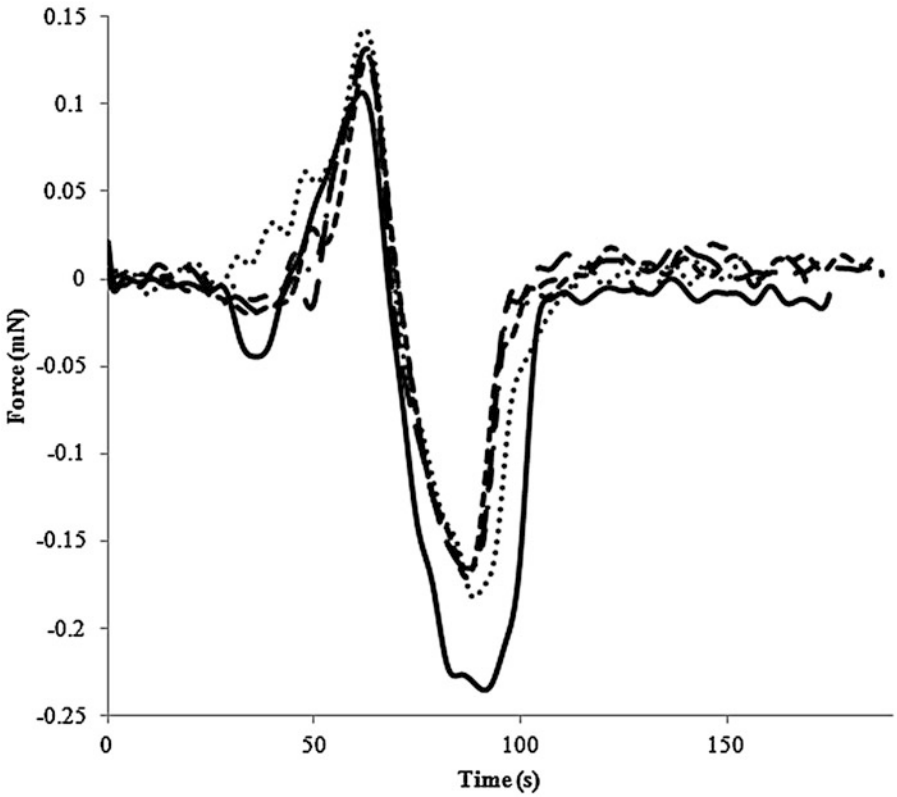

Fig. 10.2 Nematode pull off tests at different times

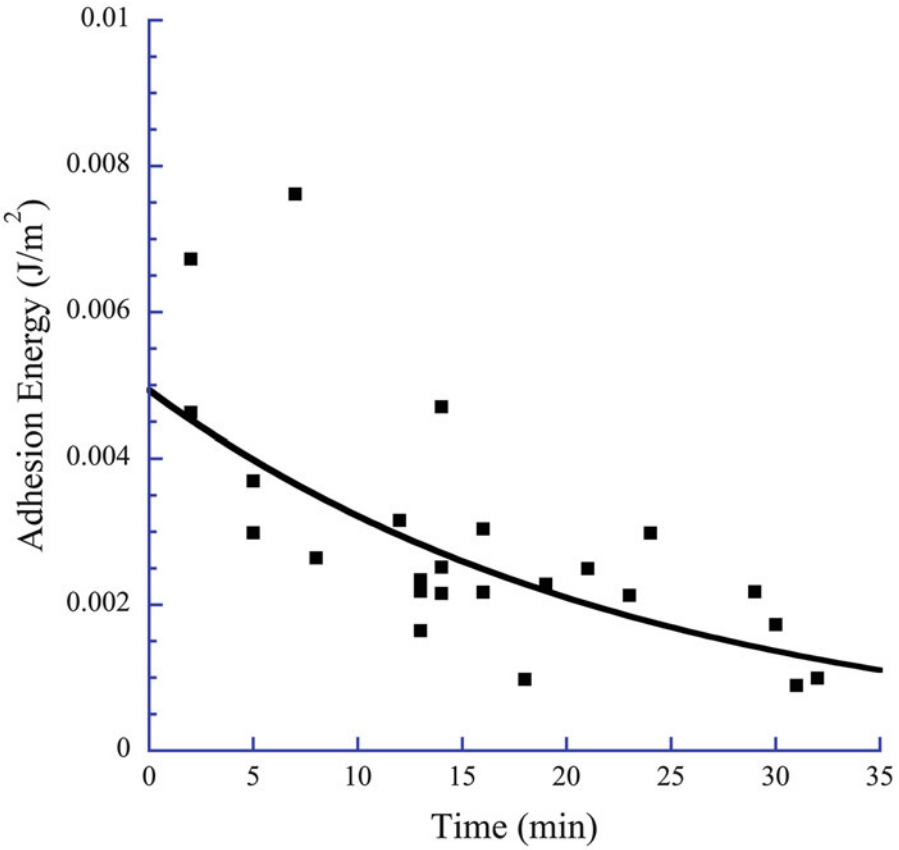

Fig. 10.3 Adhesion energy measured from maximum pull-off force as a function of time

previous researchers was between 5.0 and 3.5 mJ/m^2, which compares well with the measured value of 4.95 mJ/m^2. From the model described by Shen and coworkers, the estimated value of surface energy was used to indicate that this parameter is relatively unimportant in nematode motion on flat surfaces. However as described in the introduction, recent research has indicated that *C. elegans* has a feedback system that modulates worm muscle response based on the environment [6], implying that simple surface tension modification experiments may not capture the entire effect of surface forces on nematode locomotion.

10.5 Conclusions

In this work, an estimate of the adhesion energy of single *C. elegans* nematodes was derived from pull-off testing. Based on a JKR-type adhesion model, the adhesion energy was found to be $W = 4.94 \pm 1.19$ mJ/m^2 for a wildtype *N2* nematode. A roughly exponential decrease in adhesion energy over time was observed and is assumed to be the result of drying of the nematode or agar surface. Based on comparisons with the surface energy of water over similar lengths to the nematode, it is likely that the water bridge form the nematode to the agar surface is dominating the adhesion.

References

1. White JG, Southgate E, Thomson JN, Brenner S (1986) The structure of the nervous system of the nematode *Caenorhabditis elegans*. R Soc Lond Philos Trans 314:1–340
2. Brenner S (1974) The genetics of *Caenorhabditis elegans*. Genetics 77:71–94
3. Berri S, Boyle JH, Tassieri M, Hope IA, Cohen N (2009) Forward locomotion of the nematode *C. elegans* is achieved through the modulation of a single gait. HSFP J 3:186–193

4. Sauvage P, Argentina M, Drappier J, Senden T, Siméon J, Di Meglio JM (2011) An elasto-hydrodynamical model of friction for the locomotion of *Caenorhabditis elegans*. J Biomech 44:1117–1122
5. Shen XN, Sznitman J, Krajacic P, Lamitina T, Arratia PE (2012) Undulatory locomotion of *Caenorhabditis elegans* on wet surfaces. Biophys J 102:2772–2781
6. Wen Q, Po MD, Hulme E, Chen S, Liu X, Kwok SW, Gershow M, Leifer AM, Butler V, Fang-Yen C, Kawano T, Schafer WR, Whitesides G, Wyart M, Chklovskii DB, Zhen M, Samuel ADT (2012) Proprioceptive coupling within motor neurons drives *C. elegans* forward locomotion. Neuron 76:750–761
7. Stiernagle, T. Maintenance of *C. elegans* (2006) *WormBook*, ed. The *C. elegans* Research Community
8. Keller MW, Sottos NR (2006) Mechanical properties of microcapsules used in a self-healing polymer. Exp Mech 46:725–733
9. Chaudhury MK, Weaver T, Hui CY, Kramer EJ (1996) Adhesive contact of cylindrical lens and a flat sheet. J Appl Phys 80:30–37
10. Normand V, Lootens DL, Amici E, Plucknett KP, Aymard P (2000) New insight into agarose gel mechanical properties. Biomacromolecules 1:730–738

Chapter 11
A Fractional Order Model for Local Electric Fields in Tissues

Md. Mehedi Hasan and Corina Drapaca

Abstract In recent years, electro-chemotherapy and gene electro-transfer have emerged as promising cancer therapies that use locally applied electric fields to facilitate the transport of chemotherapeutic drugs into tumor cells or genes into target cells based on the cell membrane electroporation. It is well known that the local electric field in the tissue depends on the applied voltage on the electrodes, the geometry and position of the electrodes, and on the heterogeneity and geometry of the tissue. So far, the local electric field distribution in tissues was found by solving the classic Laplace equation. However, tissues and tumors have evolving microstructures which affect the distribution of the applied electric field. Inspired by the successful application of fractional order constitutive models of tissues, in our exploratory study we propose a fractional calculus based approach to model the electric field and potential distribution in tissues. The resulting fractional differential equation of Laplace type is solved analytically. Our preliminary results on the local electric field distribution might help to find electrode configurations for optimal treatment outcome.

Keywords Electroporation • Electric potential • Tissue inhomogeneity • Fractional differential equations • Green's functions

11.1 Introduction

In electroporation phenomena a cell or tissue is exposed to a sufficient high external electric field [1]. Pulsed electric field has been used in electroporation to facilitate the transport of drugs and genetic materials into cells. Over the last decade electroporation has been used clinically in gene delivery and treatment of localized cancers. The success of electroporation-based therapies depends on the electrode configuration and size, and pulsing protocol [2]. Among various electrode configurations, so far the most successful one is a six needle array electrode configuration that surrounds the target tissue (tumor) as shown in Fig. 11.1. The electroporation technique works as follows. An electric pulse is applied from the implanted electrodes until the entire tumor has been exposed. Different electrodes are active during different pulses. To proper design and optimize the pulsing sequence, the strength of the applied electric field must be known. However, the electric field strength does not depend only on the size, geometry and location of the electrodes, and the pulse sequence, but also on the tissue microstructure. The maximum electric field strength is obtained in homogeneous tissues. However, both healthy and pathological tissues are highly heterogeneous materials due to their complex, evolving microstructures and therefore a strong electric field inside the tumor is usually achieved by inserting more electrodes and/or by increasing the applied voltage. Both of these approaches produce damage to the healthy surrounding tissue. Therefore, new theoretical and experimental methods that maximize the electric field while minimizing the amount of damage to the healthy tissues are urgently needed. In this paper we will focus on a new theoretical framework that might contribute to the development of optimal electroporation-based treatments in the near future.

The existing mathematical models of electroporation involve solving the classic Laplace (or Poisson) equation for the electrostatic potential. Various numerical methods, such as finite element or finite difference methods have been used to calculate the potential and corresponding electric field for different electrode configurations [3–6]. Analytical solutions for

Md. M. Hasan (✉) • C. Drapaca
The Pennsylvania State University, University Park, PA, USA
e-mail: mzh204@psu.edu

F. Barthelat et al. (eds.), *Mechanics of Biological Systems and Materials, Volume 7: Proceedings of the 2014 Annual Conference on Experimental and Applied Mechanics*, Conference Proceedings of the Society for Experimental Mechanics Series,
DOI 10.1007/978-3-319-06974-6_11,

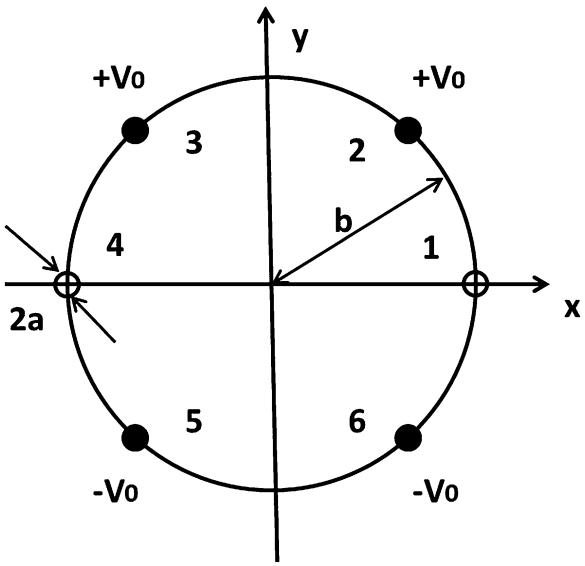

Fig. 11.1 Schematic of the electrode configuration used in [2]. Six identical *circular needles* of radius a are placed at the periphery of a circle of radius b surrounding the target tissue. The *black circles* represent cross-sections of active electrodes kept at potentials + V_0 or − V_0. *White circles* represent electrodes of zero potential

two [7] and six needles electrode configurations [2] have also been provided. Pupo et al. [8] presented analytical and numerical representations of the potential and electric field distributions inside a tumor in a 2D model with electrode arrays with various different conic sections. However, these mathematical models do not account for the role played by cell junction and tissue's microstructure in electroporation and thus their predictions may not agree with the experimental observations [9, 10]. An attempt at modeling tissue inhomogeneity was presented in [11] where two different values for tissue conductivity were used in the finite element solver developed for the case of constant conductivity: a higher conductivity for the tumor, and a lower one for the surrounding tissue. Granot and Rubinski [12] used experimental observations reported in the literature regarding the linear dependence of tissue conductivity on the electric field, to calibrate a mathematical model of electroporation in heterogeneous tissues with non-constant conductivity. To find the function that represents the spatial variations of the conductivity, Granot and Rubinski solve an (ill-posed) inverse problem for known electric potentials. However, the regularization approach used to deal with the ill-posedness of the problem makes it difficult to detect small inhomogeneities and sharp interfaces between two tissue types.

In this paper we propose to model tissue inhomogeneities using a fractional calculus approach. In recent years fractional calculus has been successfully used in modeling multiple temporal and/or length scaling and non-locality in a wide range of materials and phenomena. We will use the same approach of the electromagnetic theory in fractional dimensional space where fractional integration and differentiation provide the mathematical apparatus to describe wave propagation, radiation and scattering in a fractal media [13, 14]. By immersing fractals into the geometrical and physical framework provided by fractional calculus, such media can thus be described by continuous models which use fewer parameters to characterize media with complex microstructures. It has been showed [14] that in a fractional dimensional space there exists an electrostatic potential, solution to a *fractional* order differential equation of Laplace type, whose *fractional* gradient gives the corresponding electric field. We postulate that *the fractional order of the space is a measure of the amount of (fractal) microstructure present in the observed media (in our case tissues with tumors)*. As in [13], we use the method of Green's functions to find the electric potential to a variant of a fractional order equation of Laplace type and provide numerical simulations for electroporation using a six needle array electrode configuration. Our simulations show the convergence of the proposed analytic solutions to the solutions obtained in the classic case as the fractional order approaches 1.

11.2 Mathematical Model

Referring to Fig. 11.1, we assume that the needle penetration depth is larger than the distance between the electrodes. In addition, the needles are long, of uniform thickness of radius a, and fully inserted into the tissues. Therefore, the electric potential away from the tips of the needles can be considered two dimensional. The applied voltage at each needle is $+V_0$ for needles 3 and 4, $-V_0$ for needles 5 and 6, and zero for needles 1 and 2.

Table 11.1 Comparison between the fractional and classic electrostatic models

Fractional model	Classical model
Fractional equation of Laplace type $\nabla^{2\alpha}\phi(r) = 0,\ 0.5 < \alpha \leq 1$	Laplace equation $\nabla^{2}\phi(r) = 0$
Fractional field at needle n $\phi_{\mathrm{n}}(r) = \frac{\Gamma(1-\alpha)}{2^{2\alpha}\pi\,\Gamma(\alpha)} \frac{C_n}{\lvert r-r_n\rvert^{2-2\alpha}}$	Potential field at needle n $\phi_{\mathrm{n}}(r) = \frac{C_n}{2\pi}\ \ln\ \frac{a}{r-r_n}$
Fractional electric field at needle n $E_{\mathrm{n}}(r) = \frac{(2\alpha-2)\Gamma(1-\alpha)}{2^{2\alpha}\pi\,\Gamma(\alpha)} \frac{C_n}{\lvert r-r_n\rvert^{3-2\alpha}}$	Electric field at needle n $E_{\mathrm{n}}(r) = \frac{C_n}{2\pi}\frac{a}{r-r_n}$

The classic solutions are taken from [2, 11]

Let the electric potential ϕ (r) be the solution of the following fractional order equation of Laplace type:

$$\nabla^{2\alpha}\phi(r) = 0,\ 0.5 < \alpha \leq 1 \tag{11.1}$$

where $\nabla^{2\alpha}$ represents the generalization of the fractional quantum Riesz derivative introduced in [13–17]. The method of Green's functions provides the following particular expression for the fractional Green's function of Eq. (11.1) [13]:

$$G(r-a) = \frac{\Gamma(1-\alpha)}{2^{2\alpha}\pi\,\Gamma(\alpha)} \frac{1}{\lvert r-a\rvert^{2-2\alpha}} \tag{11.2}$$

Thus the potential of the six needle electrode configuration is given by [2, 11]:

$$\phi(r) = \sum_{n=1}^{6} \phi_n(r) \tag{11.3}$$

where

$$\phi_{\mathrm{n}}(r) = \frac{\Gamma(1-\alpha)}{2^{2\alpha}\pi\,\Gamma(\alpha)} \frac{C_n}{\lvert r-r_n\rvert^{2-2\alpha}} \tag{11.4}$$

is the electric potential for n-th electrode. r_n is the position of n-th electrode and C_n is a constant which can be determined from boundary conditions. In polar coordinates the differentiation of Eq. (11.4) gives the local electric field at each node n:

$$E_{\mathrm{n}}(r) = \frac{(2\alpha-2)\Gamma(1-\alpha)}{2^{2\alpha}\pi\,\Gamma(\alpha)} \frac{C_n}{\lvert r-r_n\rvert^{3-2\alpha}} \tag{11.5}$$

and the total electric field is thus the sum of all the local electric fields given by formula (11.5). In Table 11.1 we show a comparison between the potential and electric field distributions for the fractional and classic cases.

11.3 Results

As in [11], we take the radius of a needle to be a = 0.20 mm and the radius of the array configuration to be b = 5 mm. We consider the voltage on each active needle to be V_0 = 0.5 V such that the potential difference between the two needle pairs of opposite polarity is 1 V. A Dirichlet boundary condition has been employed on the surface of the needle, and 0 V was applied on needles 1 and 4.

We used Matlab to plot the fractional and classic potential and electric field distributions along three different paths bisecting the electrode array. In Figs. 11.2, 11.3, and 11.4 we show the potentials (Figs. 11.2a, 11.3a, and 11.4a) and corresponding electric fields (Figs. 11.2b, 11.3b, and 11.4b) for various values of the fractional order α and for paths through needles 6 and 2 (Fig. 11.2), through the center of the array (Fig. 11.3), and through needles 3 and 2 (Fig. 11.4). All the plots show that as the order α approaches 1, the fractional solutions converge to the corresponding classic solutions. Figures 11.2a, 11.3a, and 11.4a also present zoom-ins in some regions which consistently show that as the fractional order approaches 1 the potential profiles get steeper. Figures 11.2b and 11.4b show that in these two cases the electric fields are very high

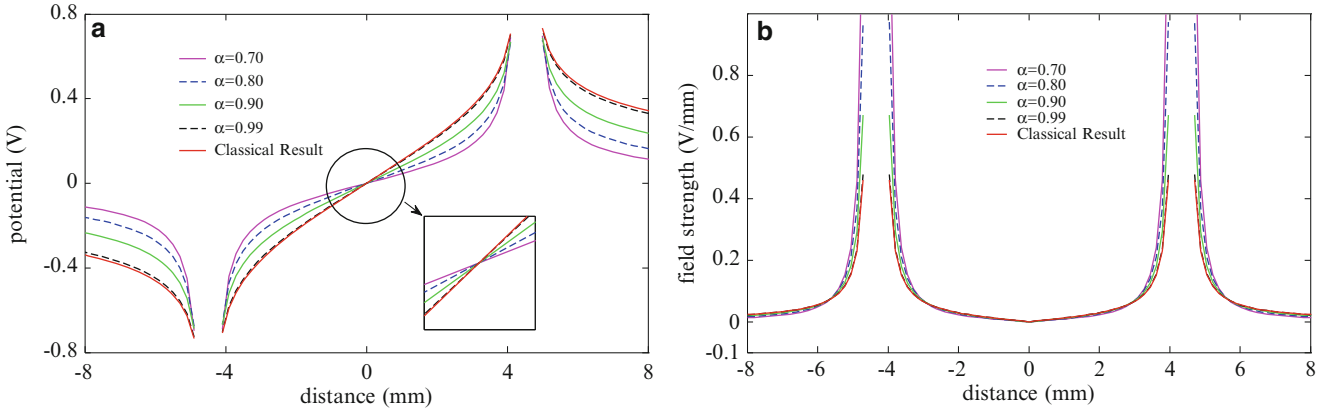

Fig. 11.2 Potential (**a**) and corresponding electric field (**b**) distributions as functions of position for a path through needles 6 and 2, and various values of the fractional order

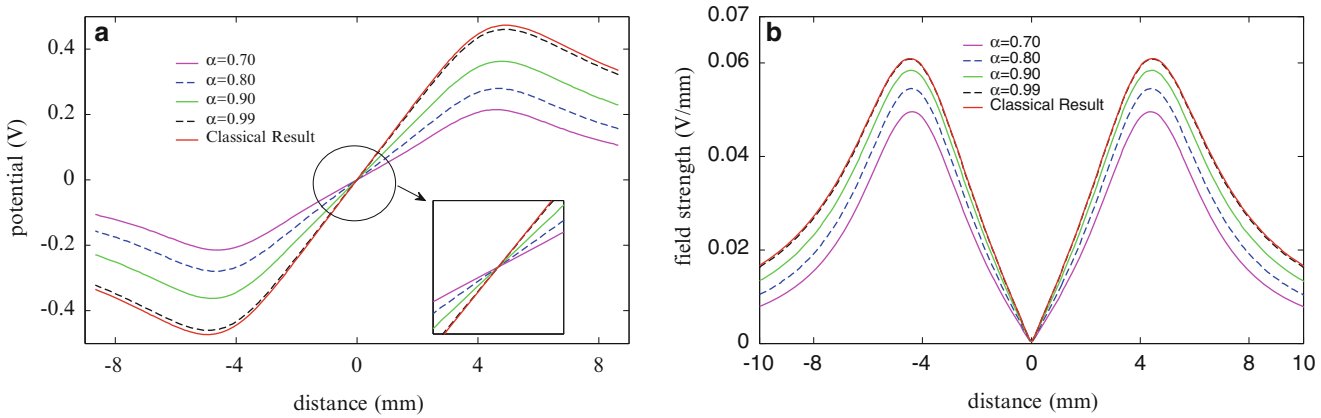

Fig. 11.3 Potential (**a**) and corresponding electric field (**b**) distributions as functions of position for a path through the center of the array and various values of the fractional order

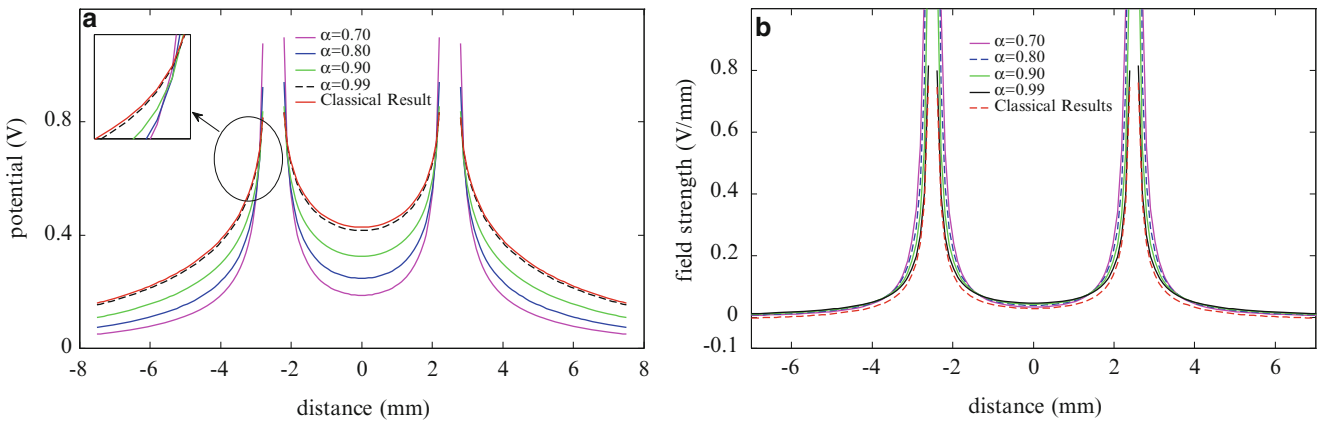

Fig. 11.4 Potential (**a**) and corresponding electric field (**b**) distributions as functions of position for path through needles 3 and 2 and for various values of the fractional order

on the boundary of the circular region of radius b, but in the disk bounded by this circle the fields are homogeneous. However the electric field strengths fall sharply to very small values inside the region bounded by the needle array.

On the other hand, the profile of the electric field along the path passing through the origin of the needle array shows a slower decrease from the boundaries of the circle of radius b, there is a larger area of the region of interest that is exposed to non-zero electric field.

Although these results did not improved the strength of electric field, the fact that the proposed model has one controller, the fractional order α, which provides a new metric for calculating the variations of potentials and electric fields, it will allow us to perform other numerical simulations to investigate how the number of electrodes, their shapes and configurations are affected by α. Since the fractional order is a measure of tissue inhomogeneity, we will also investigate different values of fractional orders for each needle electrode since we should not expect that the needles are located in locations with similar microstructures. Lastly, we intend to study the effect of various pulse sequences on the fractional electric field strengths. Another important factor that needs to be addressed is the biocompatibility between the needle electrodes and tissue. Since electroporation is intended for the use in people, the ultimate goal of these studies must be the design of optimal therapies which minimize the amount of tissue damage and maximize the electric field strength.

11.4 Conclusion

In this paper, we provided an application of fractional calculus to electroporation. We presented analytical solutions to a fractional order equation of Laplace type by using the method of Green's functions. We showed preliminary results for a six needle electrode configuration and compared them with the classic ones given by Dev et al. [9] and Čorovič et al. [11]. As the fractional order of the proposed equation approaches 1, the equation becomes the classic Laplace equation and our results show the expected convergence of our solutions to the classic ones. We postulate that this fractional order is a measure of tissue inhomogeneity and although our results did not show an improvement in the homogeneity and strength of the predicted electric field, we believe that the proposed model is simple enough so that it can be used as the foundation for more complex studies of electroporation.

References

1. Pavliha D, Kos B, Marčan M, Zupanič A, Serša G, Miklavčič D (2013) Planning of electroporation- based treatments using web-based treatment planning software. J Membr Biol 246:833–842
2. Dev SB, Dhar D, Krassowska W (2003) Electric field of a six-needle array electrode used in drug and DNA delivery in vivo: analytical versus numerical solution. IEEE Trans Biomed Eng 50(11):1296–1300
3. Hofmann GA, Dev SB, Dimmer S, Nanda GS (1999) Electroporation therapy: a new approach for the treatment of head and neck cancer. IEEE Trans Biomed Eng 46:752–759
4. Brandinsky K, Daskalov I (1999) Electrical field and current distributions in electrochemotherapy. Bioelectrochem Bioenerg 48:201–208
5. Hofmann GA, Dev SB, Nanda GS (1996) Electrochemotherapy: transition from laboratory to the clinic. IEEE Eng Med Biol Mag 15:124–132
6. Miklavčič D, Beravs K, Semrov D, Čemažar M, Demšar F, Serša G (1998) The importance of electric field distribution for effective in vivo electroporation of tissues. Biophys J 74:2152–2158
7. Ramo S, Whinnery JR, Van Duzer T (1965) Fields and waves in communication electronics. Wiley, New York
8. Pupo AEB, Reyes JB, Cabrales LEB, Cabrales JMB (2011) Analytic and numerical solutions of the potential and electric field generated by different electrode arrays in a tumor tissue under electrotherapy. Biomed Eng 10:85
9. Debruin KA, Krassowska W (1999) Modeling electroporation in a single cell. I. Effect of field strength and ret potential. Biophys J 77:1213–1224
10. Mezeme ME, Pucihar G, Pavlin M, Brosseau C, Miklavcic D (2012) A numerical analysis of multicellular environment for modeling tissue electroporation. Appl Phys Lett 100:143701
11. Čorovič S, Pavlin M, Miklavčič D (2007) Analytical and numerical quantification and comparison of the local electric field in the tissue for different electrode configurations. Biomed Eng Online 6:37–50
12. Granot Y, Rubinsky B (2011) Mathematical models of mass transfer in tissue for molecular medicine with reversible electroporation. In: Vafai K (ed) Porous media: applications in biological systems and biotechnology. Taylor & Francis, New York, pp 45–74
13. Mulish SI, Agrawal OP (2010) Riesz fractional derivatives and fractional dimensional space. Int Theory Phys 47(2):270–275
14. Zubair M, Mughal MJ, Naqvi QA (2012) Electromagnetic fields and waves in fractional dimensional space, Springer briefs in applied sciences and technology. Springer, New York
15. Samko SG, Kilbas AA, Marichev OI (2006) Fractional integrals and derivatives: theory and applications. Gordon and Beach, New York
16. Podlubny I (1999) Fractional differential equations. Academic, San Diego
17. Kilbas AA, Srivastava HM, Trujillo JJ (2006) Theory and applications of fractional differential equations. Elsevier, Amsterdam

Chapter 12
Simulation of Atherosclerotic Plaque Delamination Using the Cohesive Zone Model

Xiaochang Leng, Xin Chen, Xiaomin Deng, Michael A. Sutton, and Susan M. Lessner

Abstract Arterial tissue failure leads to a number of potentially life-threatening clinical conditions such as atherosclerotic plaque rupture and aortic dissection, which often occur suddenly and unpredictably in vivo. Atherosclerotic plaque rupture is responsible for roughly 75 % of all newly developed and recurring myocardial infarctions. Mouse models of atherosclerosis are often used in research studies because plaque characteristics can be manipulated experimentally in a reproducible fashion. To simulate atherosclerotic plaque delamination in mouse abdominal aorta, we adopt the Holzapfel model for the bulk material behavior and the cohesive zone model (CZM) for the delamination behavior along the plaque-media interface. In the Holzapfel model, each artery layer is treated as a fiber-reinforced material with the fibers symmetrically disposed with respect to the axial direction of the aorta. In the CZM, delamination is governed by a traction-separation law. A proper set of Holzapfel parameter values and CZM parameter values is determined based on values suggested in the literature and through matching the simulation predictions of the load vs. load-point displacement curve with experimental measurements for one plaque delamination cycle. With the same set of Holzapfel parameter values and CZM parameter values, two more simulation predictions of the load vs. load-point displacement curve were obtained, which match well with experimental measurements, thus validating the CZM approach. Our approach can be readily modified to understand tissue failure processes in human pathologies, e.g. aortic dissection.

Keywords Atherosclerotic plaque • Delamination • Cohesive zone model • Holzapfel model • Energy release rate

12.1 Introduction

Arterial tissue failure leads to a number of potentially life-threatening clinical conditions such as atherosclerotic plaque rupture and aortic dissection, which often occur suddenly and unpredictably in vivo. Atherosclerotic plaque rupture is responsible for roughly 75 % of all newly developed and recurring myocardial infarctions, which affect approximately 1.1 million people in the USA per year with a 40 % fatality rate [1].

Clinical autopsy studies have shown that plaque rupture often occurs at two sites: (1) the center of the plaque, where the fibrous cap may be very thin, and (2) the shoulder region, where the interface between the plaque and the underlying vascular wall is located [2]. Relevant to the second plaque rupture site, the interface strength of the bond between the plaque and vascular wall is important for the stability of the plaque. The local critical energy release rate, which is the energy required to delaminate a unit area of the plaque from the underlying vascular wall, provides a measure for quantifying the interface strength. As such, it is important to understand catastrophic arterial failures in order to develop effective approaches for treatment and intervention. To understand the atherosclerotic plaque rupture phenomena we have developed a finite element simulation procedure and applied the procedure to plaque delamination in mouse aorta.

An important part of finite element simulation studies is the modeling of material behavior. In the literature aorta has been modeled as a linearly elastic material in finite element analysis of the distribution of the circumferential stress in ruptured

X. Leng • X. Chen • X. Deng (✉) • M.A. Sutton
Department of Mechanical Engineering, University of South Carolina, Columbia, SC 29208, USA
e-mail: deng@cec.sc.edu

S.M. Lessner
Department of Cell Biology and Anatomy, University of South Carolina, Columbia, SC 29208, USA

F. Barthelat et al. (eds.), *Mechanics of Biological Systems and Materials, Volume 7: Proceedings of the 2014 Annual Conference on Experimental and Applied Mechanics*, Conference Proceedings of the Society for Experimental Mechanics Series,
DOI 10.1007/978-3-319-06974-6_12,

and stable atherosclerotic lesions [3]. In the evaluation of the impact of calcification on plaque structural stability, the finite element method has been applied to the study of human coronary atherosclerotic lesions using an isotropic, incompressible, Mooney-Rivlin finite-strain elasticity material model [4]. A composite material model has been proposed in the literature to capture the nonlinear properties of arterial wall, in which each arterial layer is treated as a fiber-reinforced material with the fibers corresponding to the collagenous component embedded in a non-collagenous matrix [5]. To account for the distribution of collagen fibers, an additional structure parameter has been added in the composite material model [6].

Atherosclerotic plaque is composed of a plaque core (which may contain a lipid core and calcifications in advanced lesions) and the underlying arterial wall, including a media layer and an adventitia layer. Plaque rupture is similar to the common delamination damage phenomenon in laminated fiber-reinforced composites between composite layers because of the relatively weak interlaminar strength. Methods based on the cohesive zone model (CZM) have been proven to be an effective way of modeling delamination failure in composite materials [7]. In an application of CZM to arterial tissue failure [8], the arterial wall is described as an anisotropic, heterogeneous, highly deformable, incompressible material, and arterial tissue failure is represented by a strong discontinuity kinematics. This approach was also applied to model the propagation of dissection of human aortic media [9]. In another study [10], the dissection of aortic media was simulated using an anisotropic cohesive law in order to distinguish between the cohesive responses along different directions of the cohesive surface.

The present study is focused on understanding the atherosclerotic plaque rupture phenomenon by modeling and simulating experiments performed on mouse aorta specimens in which a plaque is peeled off from an arterial wall.

12.2 Material Model

Under physiological conditions, arteries are regards as nearly incompressible material. Healthy arteries behave as highly deformable composite structures and exhibit a nonlinear stress–strain response with typical stiffening at the physiological strain level [10]. To simulate atherosclerotic plaque delamination in mouse aorta, we adopt the Holzapfel model [5] for the bulk material behavior and the cohesive zone model (CZM) [11] for the delamination behavior along the plaque-media interface. In the Holzapfel model, each artery layer is treated as a fiber-reinforced material with the fibers symmetrically disposed with respect to the axial direction of the aorta. In the CZM, delamination is governed by a traction-separation law.

12.2.1 Bulk Material for the Mouse Aorta

Holzapfel model assumes that the mean orientation of collagen fibers has no out-of-plane component [6], and state that the preferred orientation of the 3D collagen fiber network lies parallel to the aorta wall, although in mouse aorta there are some fiber orientations with an out-of-plane component to prevent out-of-plane shearing [12].

The anisotropic hyper-elastic potential $\psi(C, H_1, H_2)$ for an arterial layer can be represented by a superposition of the isotropic potential $\psi_g(C)$ for the non-collagenous ground-matrix (indicated by subscript 'g'), and the two transversely isotropic potentials ψ_{f1}, ψ_{f2}, for two families of embedded collagen fibers (with subscript 'f'). Thus, the free-energy function [7, 13], is

$$\psi(C,H_1,H_2) = \psi_g(C) + \left[\psi_{f1}(C,H_1(a_{01},\kappa)) + \psi_{f2}(C,H_2(a_{02},\kappa))\right] \tag{12.1}$$

where C is the right Cauchy–Green strain tensor. The structure tensors H_1, H_2 depend on the direction vectors a_{01}, a_{02}, and have the following forms in a cylindrical coordinate system, in matrix notation,

$$H_1(a_{01},\kappa) = \kappa I + (1-3\kappa)(a_{01}\otimes a_{01}) \tag{12.2}$$

$$H_2(a_{02},\kappa) = \kappa I + (1-3\kappa)(a_{02}\otimes a_{02}) \tag{12.3}$$

$$[a_{01}] = \begin{bmatrix} 0 \\ cos\beta \\ sin\beta \end{bmatrix}, \quad [a_{02}] = \begin{bmatrix} 0 \\ cos\beta \\ -sin\beta \end{bmatrix} \tag{12.4}$$

The non-collagenous ground-matrix is represented by means of an incompressible isotropic neo-Hookean model,

$$\psi_g(C) = \frac{\mu}{2}(I_1 - 3) \tag{12.5}$$

where $I_1 = tr(C)$ and μ denotes the first invariant of C and the neo-Hookean parameter, respectively. The transversely isotropic free-energy functions for the two families of collagen fibers are as follows

$$\psi_{f1}(C, H_1(a_{01}, \kappa)) = \frac{k_1}{2k_2}\left[e^{k_2[tr(H_1C)-1]^2} - 1\right] \tag{12.6}$$

$$\psi_{f2}(C, H_2(a_{02}, \kappa)) = \frac{k_1}{2k_2}\left[e^{k_2[tr(H_2C)-1]^2} - 1\right] \tag{12.7}$$

$$tr(H_1C) = tr(H_2C) = \kappa I_1 + (1 - 3\kappa)I_4 \tag{12.8}$$

where $I_4 = a_{01} \cdot Ca_{01} = a_{02} \cdot Ca_{02} = {\lambda_1}^2 cos^2\beta + {\lambda_2}^2 sin^2\beta$, and λ_1 and λ_2 are the stretch ratios along the axial direction and circumferential direction of the arterial wall. Then $\psi(C, H_1, H_2)$ is reduced to

$$\psi(C, H_1, H_2) = \frac{\mu}{2}(I_1 - 3) + \frac{k_1}{k_2}\left[e^{k_2[\kappa I_1 + (1-3\kappa)I_4 - 1]^2} - 1\right] \tag{12.9}$$

Note that the constitutive parameter μ is the shear modulus of the solid without fibers; k_1 is a stress-like parameter to be determined from mechanical tests of the tissue, which is related to the relative stiffness of the fibers in the small stretch ratio region; and k_2 is a dimensionless stiffness parameter that is related to the large strain stiffening behavior of the fibers; κ is the dispersion parameter which denotes the distribution of the collagen fibers within the two families of fibers. The lower limit of the dispersion parameter κ is 0, which describes the ideal alignment of collagen fibers, whereas the upper limit of the dispersion parameter κ is 1/3, which represents the isotropic distribution of the collagen fibers [6].

12.2.2 Cohesive Model

The use of a CZM in this study is realized through a user implementation of a UEL subroutine in ABAQUS [14]. The failure mechanism in a cohesive element as described by a traction-separation law involves three steps: (1) Damage initiation, (2) damage evolution and (3) element removal [14]. Damage initiation refers to the start of degradation of the cohesive element when an effective peak traction τ_c is reached; damage evolution refers to the period after damage initiation but before complete failure and is controlled; and element removal occurs after the cohesive traction reaches zero at a critical effective separation value.

In CZM, the failure criteria is defined as part of the cohesive element degradation properties [15]. Kenane and Benzeggagh [13] proposed a failure criterion which, in some cases, fits experimental results accurately:

$$G_c = G_T \tag{12.10}$$

where G_T is obtained from

$$G_T = G_I + G_{II} + G_{III} \tag{12.11}$$

and

$$G_c = G_{Ic} + (G_{IIc} - G_{Ic})\left(\frac{G_{shear}}{G_T}\right)^{\alpha} \tag{12.12}$$

$$G_{shear} = G_{II} + G_{III} \tag{12.13}$$

In the above G_I, G_{II} and G_{III} represent the mode I, mode II and mode III energy release rate, respectively; G_{Ic}, G_{IIc} and G_{IIIc} are the corresponding fracture toughness values of the material; and α is a parameter determined by fitting Eq. (12.12) to experimental data. Failure occurs when the energy release rate G_T is equal to G_c.

The cohesive law that governs material separation can be written as:

$$\tau_i = \tau(\Delta_i) \tag{12.14}$$

$$\Delta_3^0 = T_3^0/K \tag{12.15}$$

$$\Delta_{shear}^0 = T_{shear}^0/K \tag{12.16}$$

where τ_i is the cohesive traction; Δ_i is the displacement jump in the local coordinates which is required for modeling the behavior of the material discontinuity; K is the tangential stiffness of pure Mode I triangular cohesive law; Δ_3^0 and Δ_{shear}^0 are the displacement jumps of the initial cohesive element damage under pure Mode I and Mode II, respectively; and $T_3{}^0$ and T_{shear}^0 are the strengths of the cohesive interface along the normal direction and tangential direction, respectively. Derivation of the finite element discretization is provided by Turon [7], and a finite element-based cohesive zone model is implemented as a UEL subroutine in ABAQUS [14].

12.3 Numerical Simulations of Atherosclerotic Plaque Delamination

12.3.1 Experimental Process and Simulation Model

In the plaque delamination experiment [16] modeled in this study, 6-week old apolipoprotein E-knockout (apo E-KO) male mice were used. The mice were fed a high-fat (42 % of total calories) Western-style diet for 8 months to develop atherosclerosis throughout the aorta [17]. To initiate surface separation (delamination) between the plaque and the media layer of the aorta, a small initial flaw was carefully introduced at the proximal end of the plaque. The plaques were delaminated in situ, so that the tissues surrounding and underlying the aorta provide considerable structural support, restricting the outward motion of the aorta during mechanical loading. For the thoracic aorta, the intercostal branches prevented the outward motion of the aorta. For the abdominal aorta, bent insect pins were placed at both ends of an atherosclerotic plaque to prevent excessive outward motion of the aorta due to the lack of dorsally-oriented vascular branches like thoracic aorta [16].

A schematic of the atherosclerotic plaque delamination experimental setup is shown in Fig. 12.1. A mouse carcass with exposed aorta was fastened to a small plate connected to the load cell of a Bose ELF 3200 for load data recording. The small delamination on the proximal end of the plaque was gripped by a pair of micro-clamps connected to the Bose ELF 3200 actuator which applies sequential loading–unloading cycles. The delamination process of plaque was recorded by a computer vision system. For each experiment, a load–displacement curve with multiple loading–unloading cycles was obtained. Histological analyses of the specimens were performed, which show that the delamination interface in the mouse atherosclerotic lesions is located between the plaque (a relatively acellular tissue) and the underlying internal elastic lamina (IEL), instead of within the media.

Considering the complexity of the geometry of atherosclerotic plaque, the difficulty to measure accurately the dimensions of the small aorta, and the lack of data from the experiments that were performed before the modeling study was initiated, it is not possible to reconstruct an exact geometric model for the test specimen in the current study. As such, an approximate geometry model will be built in this study based on limited and incomplete data from multiple sources. In building the model, several conclusions have been made based on available information, for example: (1) the atherosclerotic plaque

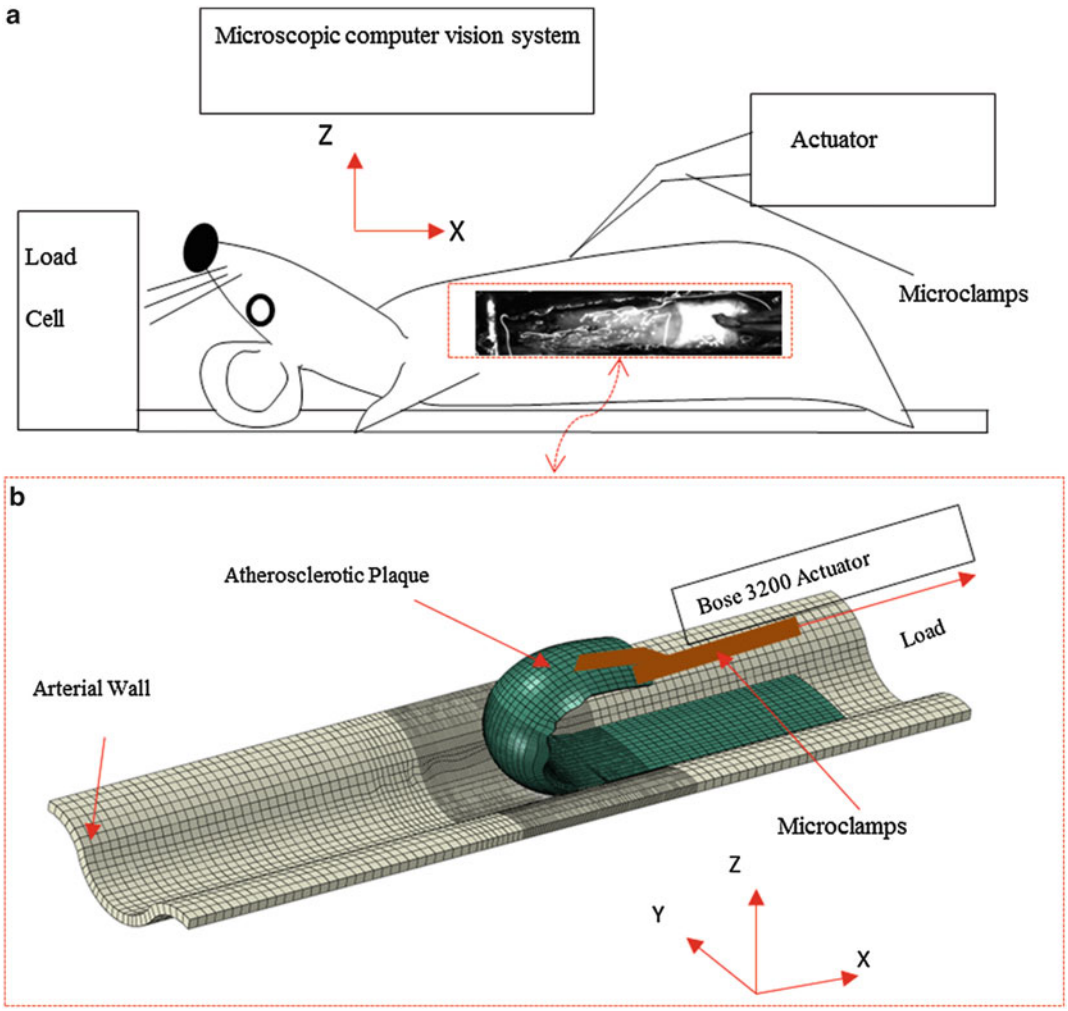

Fig. 12.1 The atherosclerotic plaque delamination experiment: (**a**) A mouse specimen on a loading table; (**b**) a schematic of the experimental process represented by a finite element model

specimen is not flat, and (2) the plaque shape is irregular, with a changing width and a rough and uneven surface. Accordingly, the resulting geometric model that best approximate the actual specimen contains an asymmetrical atherosclerotic plaque, as shown by the finite element model in Fig. 12.1b. The widths of plaque at different locations along the longitudinal direction of arterial wall are measured from experimental images, and the thickness of the plaque is taken to be constant because the total delamination length during one loading–unloading cycle is around 0.2 mm, which is a very small distance.

12.3.2 Parameter Identification

12.3.2.1 Material Properties of Holzapfel Model

Due to the lack of mechanical properties for the mouse aorta, the values of the material parameters in the Holzapfel model for the bulk artery material, which is employed in the current study, were determined based on values suggested in the literature and by matching simulation predictions with measurements using the first loading–unloading cycle of the load–displacement curve. The arterial wall and the plaque are treated as two layers of homogeneous materials, and their material parameters are shown in Table 12.1. This set of parameter values allows the predicted first loading–unloading cycle of the load–displacement curve to match reasonably well with the measured curve, as shown in Fig. 12.2.

Table 12.1 Material parameters of mice arterial wall and plaque

	μ (kPa)	k_1 (kPa)	k_2	κ	β (degree)
Arterial wall	4e-3	0.4	525	0.226	46.4
Plaque	4e-3	0.4	525	0.226	27.2

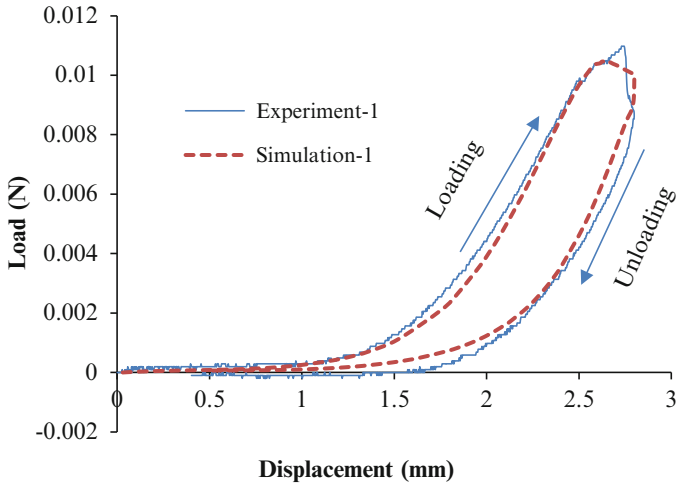

Fig. 12.2 The simulation predicted load–displacement curve of the first loading–unloading cycle during delamination is compared with the measured curve. The delamination cycle includes the loading process in which the plaque is pulled in order to cause delamination of the plaque, and the unloading process in which the plaque is returned to the initial position

Table 12.2 CZM parameter values

CZM parameters	T_3^0 (MPa)	T_{shear}^0 (MPa)	K (N/mm^3)	α
Values	0.14	0.14	1e4	1.2

The parameter β represents the angle between the mean fiber orientation and the circumferential direction of the aorta. The dispersion parameter κ describes the alignment of collagen fibers [6].

12.3.2.2 CZM Material Properties

The cohesive parameter values G_{Ic} and G_{IIc} are based on the experimental data of atherosclerotic plaque delamination from reference [16]. The plaque delamination experiment is basically a Mode I process, in which the tensile cohesive traction normal to plane of delamination is the dominant cohesive traction. As such, G_{IIc} is simply set to be equal to G_{Ic}, since the shear component is negligible. The value of G_{Ic} from experimental measurements is found to vary with the amount of delamination [16], possibly due to variations in the geometry of the plaque and material heterogeneities along the longitudinal direction. The measured G_{Ic} are used in the CZM model.

The rest of the CZM parameter values are selected based on values suggested in the literatures, such as the tensile strength of the interface between plaque and the underlying tissue (arterial wall) [9], and by matching simulation predictions with measurements using the first loading–unloading cycle of the load–displacement curve, as described earlier for determining parameter values of the Holzapfel model for bulk mouse arterial wall and plaque behavior. The resulting CZM parameter values are shown in Table 12.2.

In the finite element simulations using the CZM approach, special care has been made so that (1) the cohesive element size is sufficiently small compared to the cohesive zone length [18], and (2) the initial stiffness of the cohesive element is sufficiently high to avoid introducing a fictitious structural compliance.

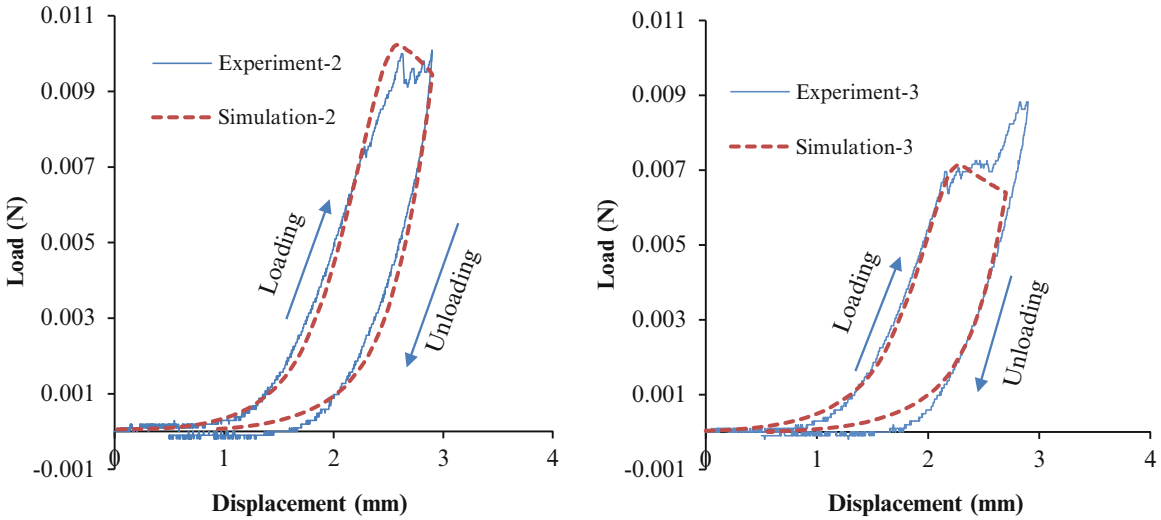

Fig. 12.3 Comparisons of the predicted and measured load–displacement curves for loading–unloading cycle 2 and cycle 3

12.4 Prediction and Validation

To avoid the effects of variations and uncertainties in specimen geometry and material properties from one experiment to another, the second and third loading–unloading cycles of the measured load–displacement curve from the same experiment as the one used to determine the material and CZM parameter values are utilized to validate the simulation predictions.

In the validation predictions for the second and third loading–unloading cycles, the same Holzapfel model parameter values for the arterial wall and the plaque, the same CZM parameter values (except for the critical energy release rate, which is taken from experimental measurements directly), and the same boundary conditions used for the first cycle were employed. Comparisons of the predicted and measured load–displacement curves for cycle 2 and cycle 3 are shown in Fig. 12.3. Although there are some differences between the predictions and measurements, overall a reasonably good agreement is achieved, which provides a validation for the CZM based simulation approach for the plaque delamination process.

12.5 Conclusions

Plaque dissection of arterial tissue often happens at the shoulder region of the fibrous cap, which is frequently observed in clinical operations. Mouse atherosclerotic plaque delamination experiments provide a way to investigate the underlying mechanism of tissue damage in order to understand the process of vascular tissue failure. Although the finite element method have been used to analyze the stress–stain behavior and tissue separation inside the arterial material during the process of plaque delamination, few studies have focused on the biomechanics of atherosclerotic plaque rupture.

In the present work, the finite element method and cohesive zone model approach has been employed to model and simulate atherosclerotic plaque delamination process. This study focused on plaque delamination experiments performed on mouse aorta specimens. Approximations of the specimen geometry were made based on limited and incomplete data from multiple sources. The bulk mouse arterial wall and plaque behavior were modeled based on a Holzapfel model in which each artery layer is treated as a fiber-reinforced material with the fibers symmetrically disposed with respect to the axial direction of the aorta. The plaque-media interface was modeled using cohesive elements. Holzapfel model and CZM parameter values were determined based on values suggested in the literature and by matching simulation prediction of the first loading–unloading cycle of the load–displacement curve with the measured curve. As validation of the CZM approach, these parameter values were then used in simulations of the second and third loading–unloading cycles of the plaque delamination experiment, and the simulation predictions of the second and third cycles match reasonably well with the measured load–displacement curve.

Acknowledgment The authors gratefully acknowledge the sponsorship of NSF (award # CMMI-1200358).

References

1. Virmani R, Narula J, Leon MB, Willerson JT (eds) (2007) The vulnerable atherosclerotic plaque: strategies for diagnosis and management. Blackwell, Malden, MA, pp 37–59
2. Loree HM, Kamm RD, Stringfellow RG, Lee RT (1992) Effects of fibrous cap thickness on peak circumferential stress in model atherosclerotic vessels. Circ Res 71(4):850–858
3. Cheng GC, Loree HM, Kamm RD, Fishbein MC, Lee RT (1993) Distribution of circumferential stress in ruptured and stable atherosclerotic lesions: a structural analysis with histopathological correlation. Circulation 87(4):1179–1187
4. Huang H, Virmani R, Younis H, Burke AP, Kamm RD, Lee RT (2001) The impact of calcification on the biomechanical stability of atherosclerotic plaques. Circulation 103:1051–1056
5. Holzapfel GA, Gasser TC, Ogden RW (2000) A new constitutive framework for arterial wall mechanics and a comparative study of material models. J Elast 61(1):1–48
6. Gasser TC, Holzapfel GA, Ogden RW (2006) Hyperelastic modelling of arterial layers with distributed collagen fibre orientations. J R Soc Interface 3(6):15–35
7. Turon A, Camanho PP, Costa J, Dávila CG (2006) A damage model for the simulation of delamination in advanced composites under variable-mode loading. Mech Mater 38(11):1072–1089
8. Gasser CT, Holzapfel GA (2007) Modeling plaque fissuring and dissection during balloon angioplasty intervention. Ann Biomed Eng 35 (5):711–723
9. Gasser TC, Holzapfel GA (2006) Modeling the propagation of arterial dissection. Eur J Mech A Solids 25(4):617–633
10. Ferrara A, Pandolfi A (2010) A numerical study of arterial media dissection processes. Int J Fract 166(1–2):21–33
11. Camanho PP, Dávila CG, de Moura MF (2003) Numerical simulation of mixed-mode progressive delamination in composite materials. J Compos Mater 37(16):1415–1438
12. Holzapfel GA (2001) Biomechanics of soft tissue. In: Lemaitre J (ed) Handbook of materials behavior models: Composite media, biomaterials, 1st edn. Academic, Boston, pp 1057–1071
13. Benzeggagh ML, Kenane M (1996) Measurement of mixed-mode delamination fracture toughness of unidirectional glass/epoxy composites with mixed-mode bending apparatus. Compos Sci Technol 56(4):439–449
14. ABAQUS (2012) Analysis user's manual version 6.12, Dassault Systemes Corp
15. Shanmugam V, Penmetsa R, Tuegel E, Clay S (2013) Stochastic modeling of delamination growth in unidirectional composite DCB specimens using cohesive zone models. Compos Struct 102:38–60
16. Wang Y, Ning J, Johnson JA, Sutton MA, Lessner SM (2011) Development of a quantitative mechanical test of atherosclerotic plaque stability. J Biomech 44(13):2439–2445
17. Nakashima Y, Plump AS, Raines EW, Breslow JL, Ross R (1994) ApoE-deficient mice develop lesions of all phases of atherosclerosis throughout the arterial tree. Arterioscler Thromb 14(1):133–140
18. Turon A, Dávila CG, Camanho PP, Costa J (2007) An engineering solution for mesh size effects in the simulation of delamination using cohesive zone models. Eng Fract Mech 74(10):1665–1682